

Università degli Studi di Napoli

“Federico II”



**Dottorato di Ricerca in
Ingegneria Aerospaziale, Navale e della Qualità
XXVII Ciclo**

Aerodynamic study of a small hypersonic plane

Coordinatore:

Ch.mo Prof. L. De Luca

Candidata:

Tutors:

Ing. Vera D'Oriano

Ch.mo Prof. R. Savino

Ing. M. Visone (BLUE Engineering)

Acknowledgements

First I wish to thank my academic tutor Prof. Raffaele Savino, for offering me this precious opportunity and for his enthusiastic guidance.

Next, I am immensely grateful to my company tutor, Michele Visone (Mike, for friends) for his technical support, despite his busy schedule, and for his constant encouragements.

I also would like to thank the HyPlane team members: Rino Russo, Prof. Battipede and Prof. Gili, Francesco and Gennaro, for the fruitful collaborations.

A special thank goes to all Blue Engineering guys (especially to Myriam) for making our site a pleasant and funny place to work.

Many thanks to queen Giuly and Peppe "il pazzo", my adoptive family during my stay in Turin, and also to my real family, for the unconditional love and care.

My greatest gratitude goes to my unique friends - my potatoes (Alle & Esa), my mentor Valerius and Franca - and to my soul mate Naso, to whom I dedicate this work.

Abstract

Access to Space is still in its early stages of commercialization. Most of the attention is currently focused on sub-orbital flights, which allow Space tourists to experiment microgravity conditions for a few minutes and to see a large area of the Earth, along with its curvature, from the stratosphere. Secondary markets directly linked to the commercial sub-orbital flights may include microgravity research, remote sensing, high altitude Aerospace technological testing and astronauts training, while a longer term perspective can also foresee point-to-point hypersonic transportation.

In recent years some private enterprises have started to develop reusable airplane-like vehicles to perform sub-orbital missions. The design of such vehicles is based on the integration of the systems developed for aeronautical purposes and the technological solutions required for the flight into the stratosphere at super-hypersonic speed.

In this scenario University of Naples “Federico II”, with the support of other universities and small and medium enterprises, is investigating a new concept for a small passenger hypersonic airplane of six seats, for long-duration sub-orbital Space tourism missions and point-to-point medium range hypersonic transportation. Such aircraft will operate on short-medium length runways of existing even small airports, since it is intended to take-off and land horizontally with relatively small speed and landing loads. The vehicle conceptual design is defined by the complex interplay of aerodynamics, atmospheric heating, materials, structures, propulsion, fuel selection and flight mechanics/dynamics.

The flight envelope covers subsonic, transonic, supersonic and hypersonic flight regimes, being hypersonic the most challenging one, constrained on the lower boundary by heating and material limits, and on the upper boundary by aerodynamic lift and propulsion performance.

Main objective of the present thesis is to provide some contributions to the studies of this vehicle, through a synergistic integration between disciplines such as aerothermodynamics, propulsion and flight mechanics.

In particular this work has been focused on the aerodynamic analysis, which is essential for the evaluation of the effects of the aerodynamic heating and for flight mechanics studies.

In this context a validation methodology of an engineering tool has been carried out, aimed at the achievement of the aerodynamic database covering all flight regimes and the prevision of the surface thermal loads which occur in the hypersonic phase, the most severe condition in terms of aerodynamic heating.

The evaluation of the effects of the aerodynamic heating has allowed a preliminary identification of proper materials able to sustain the hypersonic phase.

These analyzes are related to a preliminary reference configuration. Flight mechanic studies have allowed to refine the vehicle, although more detailed studies on the upgraded configuration are foreseen as future development.

The aerodynamic database of the upgraded configuration has been implemented in a flight simulator, along with propulsion and inertia data and trim performances have been evaluated.

Table of contents

List of Figures	i
List of Tables	vi
1 Introduction	1
1.1 A historical perspective on super-hypersonic vehicles	1
1.2 Commercial sub-orbital flight	5
1.2.1 Space Tourism	6
1.2.2 Super-hypersonic point-to-point transportation	8
References.....	12
2 HyPlane vehicle	13
2.1 System concept.....	14
2.2 Propulsion system.....	17
2.2.1 Turbine-Based Combined Cycle engines.....	17
2.2.2 Rocket engine	18
2.3 Preliminary mass budget	19
2.4 Potential mission scenarios.....	20
2.3.1 Space tourism mission	21
2.3.2 Hypersonic cruise mission.....	23
References.....	24
3 Aerodynamic models.....	25
3.1 Missile DATCOM model	26
3.1.1 Techniques and accuracy	26
3.1.2 HyPlane model	29
3.2 CFD models	32
3.2.1 Fluid dynamic governing equations	32
3.2.2 SST $k - \omega$ turbulence model	33
3.2.3 $\gamma - Re_\theta$ laminar-turbulent transition model	35
3.2.4 Radiation model	37
3.2.5 Computational grid	40
3.2.6 Solver	42
References.....	44

4 Assessment of aerodynamic prediction capabilities.....	45
4.1 Study logic.....	45
4.2 Preliminary assessment of Missile DATCOM prediction capabilities in hypersonic regime.....	47
4.3 Preliminary assessment of CFD model in hypersonic regime.....	49
4.4 Utilization of Missile DATCOM and CFD model for different flight conditions.....	51
4.4.1 Body-wing-tail configuration	51
4.4.2 Body-wing-tail-elevons configuration	60
4.5 Effects of engines on aerodynamic predictions in hypersonic regime	63
4.5.1 Mixed compression variable geometry inlet	63
4.5.2 CFD analysis and inlet performances	64
4.5.3 Body-wing-tail-engine configuration	66
References.....	67
5 Aerodynamic database.....	68
5.1 Longitudinal aerodynamic coefficients	68
5.2 Lateral-directional derivatives	72
5.3 Dynamic derivatives	73
5.4 Effect of control surfaces	75
5.4.1 Elevons effect	75
5.4.2 Ailerons effect	76
5.4.3 Rudder effect	77
References.....	78
6 Aerodynamic heating and preliminary materials identification.....	79
6.1 Boundary layer laminar-turbulent transition assessment	80
6.1.1 A case study: flat plate in hypersonic regime	80
6.1.2 Application to HyPlane fuselage and wing	82
6.2 Aerothermal analysis	88
6.1.1 Nose	88
6.1.2 Wing	89
6.3 Preliminary materials assessment	91
References.....	92

7 Preliminary trim performances.....	93
7.1 Configuration upgrade	93
7.2 Six-dof nonlinear dynamic model	96
7.3 Trim algorithm	99
7.4 Trim performances	101
References.....	103
 8 Conclusions	 104

List of Figures

- Figure 1.1** Lockheed F-104 Starfighter (a); Tupolev Tu-144 (b) and Aérospatiale-BAC Concorde (c)
- Figure 1.2** Lockheed SR-71 (a); surface temperature distribution at cruise condition (b)
- Figure 1.3** North American X-15, first hypersonic vehicle
- Figure 1.4** X-20 Dyna-Soar
- Figure 1.5** NASA X-24 B
- Figure 1.6** NASP X-30 (a), X-43 (b), X-51 (c)
- Figure 1.7** Commercial sub-orbital Space flight and prospective markets
- Figure 1.8** Virgin Galactic SpaceShipTwo on WhiteKnightTwo
- Figure 1.9** BSP Ascender (a), EADS Spaceplane (b), XCOR Lynx (c)
- Figure 1.10** EU funded projects: LAPCAT A2 (a), FAST20XX SpaceLiner (b)
- Figure 1.11** Concepts for supersonic business jets: Gulfstream X-54 (a), SAI QSST (b), Aerion SSBJ (c) and Spike S-152 (d)
- Figure 1.12** Concepts for super-hypersonic vehicles: Dassault Aviation HiSAC (a); SoniStar (b); ZEHST (c)
-
- Figure 2.1** Vehicle concepts for Space tourism and super-hypersonic point-to-point transportation
- Figure 2.2** Artistic rendering of HyPlane hypersonic vehicle
- Figure 2.3** Perspective (a), side (b), top (c), front (d) views of HyPlane
- Figure 2.4** HyPlane internal layout
- Figure 2.5** HyPlane wing and vertical tail airfoil
- Figure 2.6** Performances of Turbine-Based Combined Cycle : Maximum Thrust per engine (a) and Specific Impulse (b) as a function of Mach number at different altitudes
- Figure 2.7** Total (a) and structural (b) mass breakdowns
- Figure 2.8** Vehicle center of gravity longitudinal excursion as the propellant is consumed (from the apex of the nose)
- Figure 2.9** Space tourism mission scenario
- Figure 2.10** HyPlane performances along a possible sub-orbital parabola trajectory. Altitude and Total Sensed Acceleration (TSA) profiles (a); thrust provided by the rocket engine and mass variation profiles (b)
- Figure 2.11** Hypersonic point-to-point mission scenario
- Figure 2.12** HyPlane performances along a possible hypersonic point-to-point trajectory. Altitude and Mach number profiles (a); sonic boom profile (b)
-
- Figure 3.1** Component build-up technique
- Figure 3.2** Missile DATCOM body axis system
- Figure 3.3** HyPlane clean configuration. Original geometry (a) and Missile DATCOM model (b)
- Figure 3.4** HyPlane complete configuration. Original geometry (a) and Missile DATCOM model (b)
- Figure 3.5** Radiation exchange between two finite surfaces
- Figure 3.6** Schematic representation of radiation fluxes on patch i
- Figure 3.7** Polyhedral grid
- Figure 3.8** Computational grid refinement near the elevons
- Figure 3.9** Surface grid on the vehicle with engines

- Figure 4.1** Study logic scheme
- Figure 4.2** X-15 preliminary configuration
- Figure 4.3** Lift (a), drag (b) and pitching moment (c) coefficients as a function of angle of attack at $M_\infty = 6$, $Re_\infty = 2.71 \cdot 10^7$. Comparison between experimental data and Missile DATCOM results
- Figure 4.4** Side force (a), rolling moment (b) and yawing moment (c) coefficients as a function of angle of attack at $M_\infty = 6$, $Re_\infty = 2.71 \cdot 10^7$. Comparison between experimental data and Missile DATCOM results
- Figure 4.5** Lift and drag coefficients as a function of angle of attack, with $\delta_e = 10^\circ$, at $M_\infty = 6$, $Re_\infty = 2.71 \cdot 10^7$. Comparison between experimental data and Missile DATCOM results
- Figure 4.6** Coarse (a), medium (b) and fine (c) grids
- Figure 4.7** Flight conditions investigated with Missile DATCOM and CFD
- Figure 4.8** Predicted lift (a), drag (b) and pitching moment (c) coefficients as a function of angle of attack, for $M_\infty = 0.2$, $H = 0 \text{ km}$. Comparison between Missile DATCOM and CFD results
- Figure 4.9** Predicted lift (a), drag (b) and pitching moment (c) coefficients as a function of angle of attack, for $M_\infty = 0.7$, $H = 10 \text{ km}$. Comparison between Missile DATCOM and CFD results
- Figure 4.10** Pressure contour on the vehicle and the symmetry plane computed with CFD simulations. $M_\infty = 0.2$, $H = 0 \text{ km}$. $\alpha = 0^\circ$ (a), $\alpha = 4^\circ$ (b), $\alpha = 8^\circ$ (c), $\alpha = 12^\circ$ (d), $\alpha = 16^\circ$ (e), $\alpha = 20^\circ$ (f)
- Figure 4.11** Pressure contour on the vehicle and streamlines computed with CFD simulations. $M_\infty = 0.7$, $H = 10 \text{ km}$. $\alpha = 0^\circ$ (a), $\alpha = 4^\circ$ (b), $\alpha = 8^\circ$ (c)
- Figure 4.12** Vorticity contours and surface streamlines computed with CFD simulations. $M_\infty = 0.7$, $H = 10 \text{ km}$, $\alpha = 8^\circ$
- Figure 4.12** Predicted lift (a), drag (b) and pitching moment (c) coefficients as a function of angle of attack, for $M_\infty = 0.9$, $H = 10 \text{ km}$. Comparison between Missile DATCOM and CFD results
- Figure 4.13** Predicted lift (a), drag (b) and pitching moment (c) coefficients as a function of angle of attack, for $M_\infty = 1.0$, $H = 10 \text{ km}$. Comparison between Missile DATCOM and CFD results
- Figure 4.14** Predicted lift (a), drag (b) and pitching moment (c) coefficients as a function of angle of attack, for $M_\infty = 1.1$, $H = 10 \text{ km}$. Comparison between Missile DATCOM and CFD results
- Figure 4.15** Predicted lift (a), drag (b) and pitching moment (c) coefficients as a function of angle of attack, for $M_\infty = 1.2$, $H = 10 \text{ km}$. Comparison between Missile DATCOM and CFD results
- Figure 4.16** Predicted lift (a), drag (b) and pitching moment (c) coefficients as a function of angle of attack, for $M_\infty = 1.5$, $H = 15 \text{ km}$. Comparison between Missile DATCOM and CFD results
- Figure 4.17** Predicted lift (a), drag (b) and pitching moment (c) coefficients as a function of angle of attack, for $M_\infty = 2.0$, $H = 20 \text{ km}$. Comparison between Missile DATCOM and CFD results
- Figure 4.18** Predicted lift (a), drag (b) and pitching moment (c) coefficients as a function of angle of attack, for $M_\infty = 3.0$, $H = 30 \text{ km}$. Comparison between Missile DATCOM and CFD results
- Figure 4.19** Mach number and pressure contours on the vehicle and the symmetry plane computed with CFD simulations. $M_\infty = 2.0$, $H = 20 \text{ km}$. $\alpha = 0^\circ$ (a), $\alpha = 4^\circ$ (b), $\alpha = 8^\circ$ (c)
- Figure 4.20** Predicted lift (a), drag (b) and pitching moment (c) coefficients as a function of angle of attack, for $M_\infty = 4.0$, $H = 30 \text{ km}$. Comparison between Missile DATCOM and CFD results

- Figure 4.21** Predicted lift (a), drag (b) and pitching moment (c) coefficient as a function of angle of attack, for $M_\infty = 6.0$, $H = 30 \text{ km}$. Comparison between Missile DATCOM and CFD results
- Figure 4.22** Pressure contour on the vehicle and the symmetry plane computed with CFD simulations. $M_\infty = 2.0$, $H = 20 \text{ km}$. $\alpha = 0^\circ$ (a), $\alpha = 4^\circ$ (b), $\alpha = 8^\circ$ (c), $\alpha = 12^\circ$ (c)
- Figure 4.23** Lift (a), drag (b), pitching moment (c) coefficient as a function of Mach number for different angles of attack, computed by Missile DATCOM (solid lines) and CFD simulations (dots)
- Figure 4.24** Predicted contributes to lift (a), drag (b) and pitching moment (c) coefficients as a function of elevons deflection, for $M_\infty = 0.7$, $H = 10 \text{ km}$, $\alpha = 0^\circ$. Comparison between Missile DATCOM and CFD results
- Figure 4.25** Predicted contributes to lift (a), drag (b) and pitching moment (c) coefficients as a function of elevons deflection, for $M_\infty = 2.0$, $H = 20 \text{ km}$, $\alpha = 0^\circ$. Comparison between Missile DATCOM and CFD results
- Figure 4.26** Predicted contributes to lift (a), drag (b) and pitching moment (c) coefficients as a function of elevons deflection, for $M_\infty = 4.0$, $H = 30 \text{ km}$, $\alpha = 0^\circ$. Comparison between Missile DATCOM and CFD results
- Figure 4.27** Pressure contour on the vehicle computed with CFD simulations ($M_\infty = 0.7$, $H = 10 \text{ km}$, $\alpha = 0^\circ$). $\delta_e = 10^\circ$ (a), $\delta_e = 20^\circ$ (b)
- Figure 4.28** Pressure contour on the vehicle computed with CFD simulations ($M_\infty = 2.0$, $H = 20 \text{ km}$, $\alpha = 0^\circ$). $\delta_e = 10^\circ$ (a), $\delta_e = 20^\circ$ (b)
- Figure 4.29** Pressure contour on the vehicle computed with CFD simulations ($M_\infty = 4.0$, $H = 30 \text{ km}$, $\alpha = 0^\circ$). $\delta_e = -10^\circ$ (a), $\delta_e = -20^\circ$ (b)
- Figure 4.30** Schematic of flow field for The HyPlane turbo-ramjet inlet at the nominal condition
- Figure 4.31** Turbo-ramjet variable geometry inlet. Dimensions expressed in meters
- Figure 4.32** Mach number, pressure (a), streamlines and temperature (b) distributions at $M_\infty = 4$, $H = 30 \text{ km}$ and $\alpha = 0^\circ$, computed by CFD simulations
- Figure 4.33** Pressure, temperature (a), streamlines and total pressure (b) distributions at $M_\infty = 2$, $H = 15 \text{ km}$ and $\alpha = 0^\circ$, computed by CFD simulations
- Figure 4.34** Computational domain (a) and surface grid on the air intake (b)
- Figure 4.35** Mach number (a) and pressure (b) distributions at $M_\infty = 4$, $H = 30 \text{ km}$ and $AoA = 6^\circ$, computed by CFD simulations
- Figure 4.36** Pressure distribution for $M_\infty = 4$, $H = 30 \text{ km}$ and $\alpha = 0^\circ$ on the configuration without (a) and with engines (b), computed by CFD simulations
-
- Figure 5.1** Lift coefficient as a function of angle of attack at different Mach numbers. Subsonic (a) and supersonic (b) regimes
- Figure 5.2** Drag coefficient as a function of angle of attack at different Mach numbers. Subsonic (a) and supersonic (b) regimes
- Figure 5.3** Pitching moment coefficient as a function of angle of attack at different Mach numbers. Subsonic (a) and supersonic (b) regimes
- Figure 5.4** Lift (a) and drag (b) coefficients as a function of Mach number, at different angles of attack
- Figure 5.5** Pitching moment coefficient as a function of Mach number, at different angles of attack
- Figure 5.6** Drag coefficient as a function of angle of attack at different altitudes ($M_\infty = 4$)
- Figure 5.7** Super-hypersonic vehicle configurations
- Figure 5.8** Cruise lift-to-drag ratio for super-hypersonic vehicles and the "L/D barrier"
- Figure 5.9** Side force coefficient derivative with sideslip angle as a function of angle of attack, at different Mach numbers
- Figure 5.10** Rolling (a) and yawing (b) moment coefficients derivatives with sideslip angle as

a function of angle of attack, at different Mach numbers

- Figure 5.11** Lift derivative with rate of change of angle of attack (a) and pitch rate (b) as a function of Mach number
- Figure 5.12** Pitching moment derivative with rate of change of angle of attack (a) and pitch rate (b) as a function of Mach number
- Figure 5.13** Side force coefficient derivative with roll rate (a) and yaw rate (b) as a function of Mach number
- Figure 5.14** Rolling moment coefficient derivative with roll rate (a) and yaw rate (b) as a function of Mach number
- Figure 5.15** Yawing moment coefficient derivative with roll rate (a) and yaw rate (b) as a function of Mach number
- Figure 5.16** Contributes to lift (a) and drag (b) coefficients as a function of elevons deflection angle, at different Mach numbers
- Figure 5.17** Contribute to pitching moment coefficient as a function on elevons deflection angle, at different Mach numbers
- Figure 5.18** Contributes to lift (a) and drag (b) coefficients as a function of aileron deflection angle, at different Mach numbers
- Figure 5.19** Contributes to pitching (a) and rolling (b) moment coefficients as function of aileron deflection angle, at different Mach numbers
- Figure 5.20** Contributes to yawing moment coefficients as function of aileron deflection angle, at different Mach numbers
- Figure 5.21** Contributes to drag (a) and side force (b) coefficients as a function of ailerons deflection angle, at different Mach numbers
- Figure 5.22** Contributes to yawing (a) and rolling (b) moment coefficients as a function of ailerons deflection angle, at different Mach numbers

- Figure 6.1** 2D structured hypersonic flat plate grid
- Figure 6.2** Stanton number variation as a function of the local Reynolds number. Comparison between numerical and experimental results
- Figure 6.3** Computational domain (a) and surface grid (b) on the vehicle fuselage forefront
- Figure 6.4** Radiative equilibrium temperature distribution on the vehicle forefront fuselage ($M_\infty = 4$, $H = 30 \text{ km}$, $\alpha = 0^\circ$). Laminar (a), transitional (b) and fully turbulent (c) boundary layer
- Figure 6.5** Radiative equilibrium temperature variation along the vehicle forefront fuselage for laminar, transitional and fully turbulent boundary layer ($M_\infty = 4$, $H = 30 \text{ km}$, $\alpha = 0^\circ$). Linear scale (a) and logarithmic scale (b) for the X axis
- Figure 6.6** Turbulence intensity (a) and intermittency (b) distributions on the symmetry plane ($M_\infty = 4$, $H = 30 \text{ km}$, $\alpha = 0^\circ$)
- Figure 6.7** Computational domain (a) and surface grid (b) on vehicle wing
- Figure 6.8** Radiative equilibrium temperature distribution on the vehicle wing ($M_\infty = 4$, $H = 30 \text{ km}$, $\alpha = 0^\circ$). Laminar (a), transitional (b), fully turbulent (c) boundary layer
- Figure 6.9** Temperature variation along the vehicle wing mean aerodynamic chord for laminar, transitional and turbulent boundary layer ($M_\infty = 4$, $H = 30 \text{ km}$, $\alpha = 0^\circ$)
- Figure 6.10** Turbulence intensity and intermittency distributions along on the symmetry plane ($M_\infty = 4$, $H = 30 \text{ km}$, $\alpha = 0^\circ$). Transitional (a) and fully turbulent (b) boundary layer
- Figure 6.11** Radiative equilibrium temperature distribution on the vehicle nose at $M_\infty=4$, $H=30 \text{ km}$ and $\alpha=0^\circ$. Top view (a) and side view (b)
- Figure 6.12** Convective heat flux and corresponding radiative equilibrium temperature along the vehicle nose at $M_\infty=4$, $H=30 \text{ km}$ and $\alpha=0^\circ$
- Figure 6.13** Radiative equilibrium temperature distribution on the wing at $M_\infty=4$, $H=30 \text{ km}$ and $\alpha=0^\circ$. Sections at 1 m, 2 m and 3 m distance from the wing root

Figure 6.14 Convective heat flux and corresponding radiative equilibrium temperature along the considered wing sections at $M_\infty=4$, $H=30$ km and $\alpha=0^\circ$

Figure 6.15 Radiation equilibrium temperature distribution for $M_\infty = 4$, $H = 30$ km, $\alpha = 0^\circ$.
Leeside (a) and windside (b)

Figure 6.16 Preliminary structure and materials assessment

Figure 7.1 Longitudinal position of vehicle center of gravity at maximum takeoff weight and empty weight

Figure 7.2 HyPlane original configuration (a) and upgraded configuration (b)

Figure 7.3 Vehicle CoG longitudinal position (from the nose apex) as the propellant is consumed

Figure 7.4 Vehicle inertia properties with respect to body axes centered in the CoG, as a function of fuel mass

Figure 7.5 MASLab model block diagram

Figure 7.6 Trim algorithm

Figure 7.7 HyPlane trim envelop at MTOW and EW (a). Angle of attack (b), elevons deflection angle (c) and turboramjet throttle (c) in trimmed conditions

Figure 7.8 HyPlane trim envelope at MTOW varying the climb angle

Figure 7.9 HyPlane aerodynamic efficiency in trimmed conditions at maximum take-off weight (a) and at empty weight (b)

List of Tables

Table 1.1 Main features of vehicle concepts for Space Tourism

Table 1.2 Main features of vehicle concepts for super-hypersonic transportation

Table 2.1 HyPlane main geometric features

Table 2.2 Main geometric features of wing and vertical tail airfoil

Table 2.3 Rocket engine main performances

Table 3.1 Longitudinal aerodynamic parameters computed by Missile DATCOM

Table 3.2 Lateral-directional aerodynamic parameters computed by Missile DATCOM

Table 3.3 Main methodologies implemented in Missile DATCOM for body aerodynamic parameters computation

Table 3.4 Main methodologies implemented in Missile DATCOM for fin aerodynamic parameters computation

Table 3.5 Main methodologies implemented in Missile DATCOM for inlet aerodynamic parameters computation

Table 3.6 Main methodologies implemented in Missile DATCOM for fin-body interference estimate

Table 3.7 Missile DATCOM applicability to different geometric configurations and flight conditions

Table 3.8 Component build-up approach applicability to different geometric configurations

Table 3.9 Computational grid main parameters

Table 4.1 Coarse, medium and fine grids main parameters

Table 4.2 Flow conditions for the grid sensitivity analysis

Table 4.3 Longitudinal aerodynamic coefficients computed by CFD simulations adopting different grids

Table 4.4 Flight conditions investigated with Missile DATCOM and CFD simulations

Table 4.5 Deviation of Missile DATCOM computations, with respect to CFD results, for longitudinal aerodynamic coefficients, varying the flight regime

Table 4.6 Flight conditions investigated with Missile DATCOM and CFD simulations

Table 4.7 Analysed turbo-ramjet inlet operating conditions

Table 4.8 Turbo-ramjet supersonic inlet main performances

Table 4.9 Lift and drag coefficients during hypersonic cruise, for the configuration with and without engines, computed by CFD simulations and Missile DATCOM

Table 6.1 Flow conditions for flat plate test

Table 6.2 Flow conditions for the assessment of the boundary layer transition process on HyPlane fuselage and wing

Table 6.3 Studied cases for aerodynamic heating evaluation on HyPlane fuselage and wing

Table 6.4 Main properties of the identified materials

Table 7.1 HyPlane configurations main geometric features

1 Introduction

In this chapter a brief introduction on super-hypersonic vehicles is presented, underlining the challenges won in the past and the state-of-the-art technologies.

Commercial sub-orbital flight is then introduced and the most relevant vehicle concepts proposed worldwide are discussed. In particular the attention is focused on most promising concepts for Space tourism and point-to-point super-hypersonic transportation purposes.

1.1 A historical perspective on super-hypersonic vehicles

Human dream of flying has lead to several challenges. The engineering challenges involved in pushing aircraft to fly faster and faster are perhaps the greatest of all.

As an approach to the hypersonic vehicles, one may begin by introducing high-performing aircrafts that have flown at successively higher speeds [1,2].

At Mach number of 2, typical examples include the supersonic interceptor F-104 Starfighter and the civil SuperSonic Transport (SST) aircrafts Tupolev Tu-144 and Concorde. Those aircrafts were built of aluminum and used afterburning turbojets for propulsion.

Concorde, jointly developed and produced under and Anglo-French treaty, entered service in 1976 and continued commercial flights for 27 years. The aircraft was retired after the type's only crash in 2000 and a decision by Airbus to discontinue maintenance support.



(a)



(b)



(c)

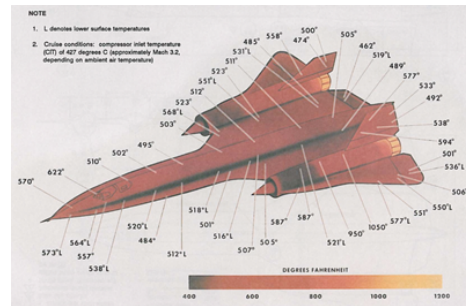
Figure 1.1: Lockheed F-104 Starfighter (a); Tupolev Tu-144 (b) and Aérospatiale-BAC Concorde (c)

At Mach 3 and higher, there was the SR-71, a strategic reconnaissance aircraft developed by Lockheed in the 1960s. The aircraft, powered by two Pratt & Whitney J-58 engines, cruised at 85000 feet (~26 km) of altitude and Mach 3.2. The ability to achieve high-altitude high-Mach flight derives from its propulsion system and structures. In particular the Turbine-Based Combined Cycle (TBCC) engines merged the low-speed attributes of turbojets with the high-speed capabilities of ramjets, to achieve maximum performance. Structures were 93% titanium with the balance

consisting of high temperature composite materials, able to sustain the aerodynamic heating that brought temperatures above 500°F (260°C).



(a)



(b)

Figure 1.2: Lockheed SR-71 (a); surface temperature distribution at cruise conditions (b)

At Mach 4 and above the physics of flow is dominated by aerodynamic heating. No version of the turbojet served at such speeds. It was necessary to use a ramjet or a rocket.

The Lockheed X-7, an unmanned ramjet test bed, was built of steel and when it flew past Mach 4.3 in 1958, the aerodynamic heating became so severe that it produced structural failure and a consequent breakup of the vehicle in flight.

The V-2 rocket, developed during the Second World War in Germany, flew above Mach 5. Steel proved suitable for its construction and aerodynamic heating played only a limited role in the overall design of the missile.

The term "hypersonics" was coined in 1946 by Hsue-shen Tzien, a Chinese aerodynamicist at the California Institute of Technology. Since then, it has involved in different significant areas of application.

The first was the atmospheric re-entry, which came to the forefront during the mid-1950s. The successful development by United States Air Force (USAF) of a heat shield to protect the first InterContinental Ballistic Missile (ICBM) against the intense aerodynamic heating opened the door to a host of other initiatives. The US Mercury, Gemini and Apollo and the Soviet Vostok, Voskhod and Soyuz were capsules with ablative heat shields, that re-entered the atmosphere ballistically, using parachutes to slow the final descent. The return of capsules from orbit became routine, allowing astronauts and cosmonauts to come back to Earth safely. The Soyuz-type vehicle is still in use today, transporting astronauts to and from the International Space Station (ISS).

The first manned airplane to fly hypersonic was the North American X-15. This rocket-powered research airplane designed during the 1950's and operated by USAF and NASA set speed and altitude marks that were not surpassed until the advent of the shuttle. The aircraft, built of the nickel alloy Inconel-X 750, was characterized by a

relatively high hypersonic lift-to-drag ratio, which offered enough cross-range for many missions. It reached altitudes high enough for some of its pilots to qualify as astronauts and routinely withstood temperatures of 1200°F (~650°C). On its fastest flight, the vehicle achieved Mach 6.7 and returned with some pieces of the sharp leading edges of the wing melted off. This flight showed that the aerodynamic heating effects would be extremely difficult to solve with the available materials and technologies.



Figure 1.3: North American X-15, first hypersonic vehicle

To overcome the limit of the thermal protection materials NASA and USAF researchers began to look at combining the thermally efficient blunt body with the ability to generate lift. Since the 1960s, a series of reusable lifting vehicles designed to re-enter the atmosphere from orbit and to land safely without parachutes to a chosen landing site, like an airplane, were tested. The manned Northrop M2-F2 and HL-10 flown to study and validate the concept of safely maneuvering and landing a low lift-over-drag vehicle. In the same period the USAF developed the X-20 Dyna-Soar, a manned winged re-entry vehicle designed for a variety of American military and Space missions. Unfortunately the vehicle was never built: the program was cancelled in 1963 just after the construction had begun. It was a far more advanced concept than other human spaceflight mission of the period and was of concern for future Spaceplane design concepts.



Figure 1.4: X-20 Dyna-Soar

In 1963 the ASSET (Aerothermodynamic Elastic Structural Systems Environmental Tests) project involved the testing of an unmanned sub-scale re-entry vehicle (originally designed to verify the superalloy heat shield of the Dyna-Soar prior to full-scale manned flights) and provided a lot of data useful for the development of future space vehicles. In 1964 the USAF START (Spacecraft Technology and Advanced Re-entry

Test) project to test the SV-5 configuration began. In the first phase, called PRIME (Precision Recovery Including Maneuvering Entry), sub-scale SV-5D vehicles were launched on Atlas boosters and flew hypersonic re-entries. In the second phase a full-scale, manned vehicle called SV-5P (which became the X-24 A) was built, to explore speed from low supersonic down to landing.

Subsequently the USAF developed a series of aircraft characterized by higher hypersonic efficiency than lifting bodies. They were intended both for re-entry vehicles and hypersonic-cruise airplanes. The X-24B, delivered in 1972, presented high performances and was favorably compared to contemporary fighters by pilots. In the last two flights of the X-24B, in 1975, pilots Manke and Love made the first two landings of a lifting body on a conventional runway.

Soviets also experimented with lifting bodies, under Project Spiral. The Mikoyan-Gurevich MiG-105, originally conceived in response to the American X-20 Dyna-Soar, was a manned test vehicle to explore low-speed handling and landing.



Figure 1.5: NASA X-24 B

Early shuttle concept designs favoured a lifting body, based on the HL-10 shape but finally a swept delta wing configuration, like the Dyna-soar, was chosen in order to achieve the maximum cross-range on re-entry. The development of the fragile but effective and reusable Thermal Protection System (TPS) allowed the vehicle to sustain the strong aerodynamic heating during the re-entry phase, which brought temperatures of about 3000°F (~1650°C).

The National Aerospace Plane (NASP) program, started in mid-1980s, was the first American attempt to create a Single Stage To Orbit (SSTO) spacecraft able to takeoff and land horizontally, the X-30. Propulsion systems based on innovative airbreathing engines (scramjets) and rockets were considered. The project was cancelled in the early 1990s, before a prototype was completed, due to cost and technical challenges, but it was later developed into X-43, which was essentially an unmanned scaled-down X-30. In 2004 the X-43A set a speed record of approximately 6.6 mph (10.6 km/h).

The X-51 was an unmanned scramjet demonstration aircraft designed for high range hypersonic flight at Mach number of 6. The program is a collaborative effort of USAF,

NASA, DARPA with industry partners Boeing and Pratt & Whitney Rocketdyne. In May 2013 the vehicle reached speeds of over Mach 5 for 143 seconds, setting the record for the longest duration airbreathing hypersonic flight. The test proved the technologies in hypersonic field has matured enough to open the door to practical applications, such as advanced defense systems and more cost-effective access to space.

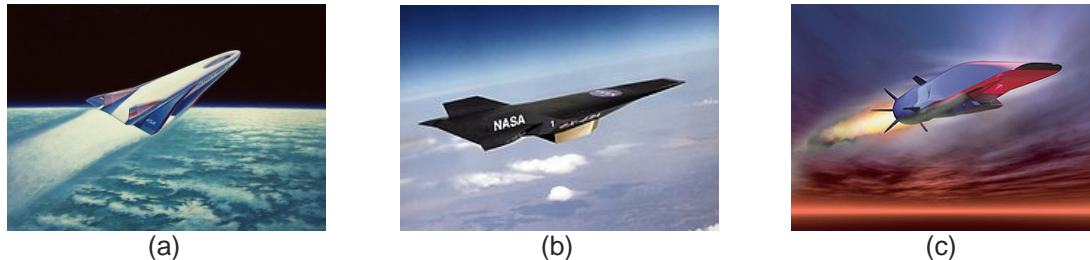


Figure 1.6: NASP X-30 (a), X-43 (b), X-51 (c)

1.2 Commercial sub-orbital flight

Access to Space is still in its early stages of commercialization. Most of the attention is currently focused on sub-orbital flights, while orbital ones still appear limited and expensive.

Sub-orbital flights allow Space tourists to experiment microgravity conditions for a few minutes and to see a large area of the Earth, along with its curvature, from the stratosphere [3]. As shown in Figure 1.7, secondary markets directly linked to commercial sub-orbital flights may include microgravity research, remote sensing, high altitude Aerospace technological testing and development, astronauts training and so forth, while a longer term perspective can also foresee point-to-point hypersonic transportation.

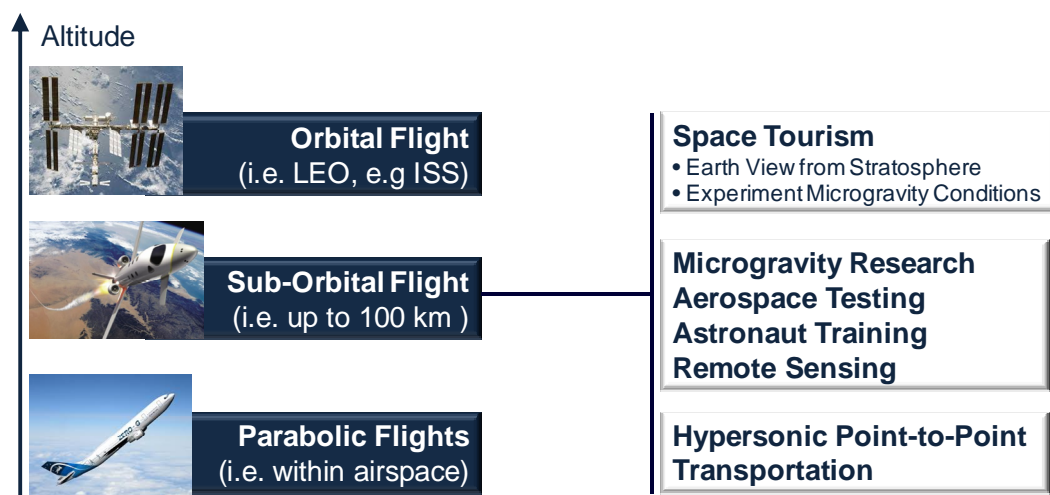


Figure 1.7: Commercial sub-orbital Space flight and prospective markets

In recent years several private enterprises have started to develop reusable airplane-like vehicles to perform sub-orbital missions, for Space tourism and super-hypersonic point-to-point transportation purposes.

The design of such vehicles is based on the integration of the systems developed for aeronautical purposes and the technological solutions required for the flight into the stratosphere at super-hypersonic speed.

The most promising concepts for Space tourism and point-to-point super-hypersonic transportation are presented in the following sections.

1.2.1 Space tourism

Some private enterprises have recently been approaching Space flight with a relatively low-cost philosophy, hoping to create a Space tourism business.

Scaled Composites constructed for the ambitious British company Virgin Galactic the Space Ship One (SS1), a sub-orbital air-launched Spaceplane for manned private Spaceflight. In its first flight in 2004, the vehicle reached 100 km altitude on a sub-orbital trajectory 36 years after the X-15, developed by NASA at the turn of 50s and 60s. The company is presently test qualifying an enlarged version of the SS1, named SS2, intended to carry passengers for a short-duration Space flight at a fare of about 200 k\$ per seat. The aircraft is carried to its launch altitude by a Scaled Composites White Knight Two, before being released to fly into the upper atmosphere powered by its rocket engine; then the ship glides back to the Earth and performs a conventional runway landing. In October 2014, the first SS2 craft called VSS Enterprise broke up in-flight and crashed in the Mojave Desert. Despite the accident, a second SS2 called VSS Voyager is under construction.



Figure 1.8: Virgin Galactic SpaceShipTwo on WhiteKnightTwo

Other projects included in this frame are Bristol Spaceplanes (BSP) Ascender, the EADS Spaceplane and the XCOR Lynx [5].

The Ascender is a small Spaceplane for Space tourism and microgravity research purposes. The vehicle is designed to takeoff from a typical runway powered by two turbojet engines, achieve altitudes of up to 100 km taking advantage from the hydrogen peroxide rocket engine, gliding back to the Earth and, finally, land on the same runway

using the turbojet engines. Also the EADS (European Aeronautic Defence and Space Company) Spaceplane uses turbojet engines for the atmospheric phase and by a rocket engine (powered by liquid methane and liquid oxygen) for the Space tourism phase. The XCOR Lynx, a rocket powered Spaceplane under development by the American company XCOR Aerospace, is designed to realize horizontal takeoff and horizontal landing (HTHL) and to carry one pilot and one ticketed passenger and/or a payload above 100 km. As of March 2014, the passenger ticket was projected to cost 95 k\$.

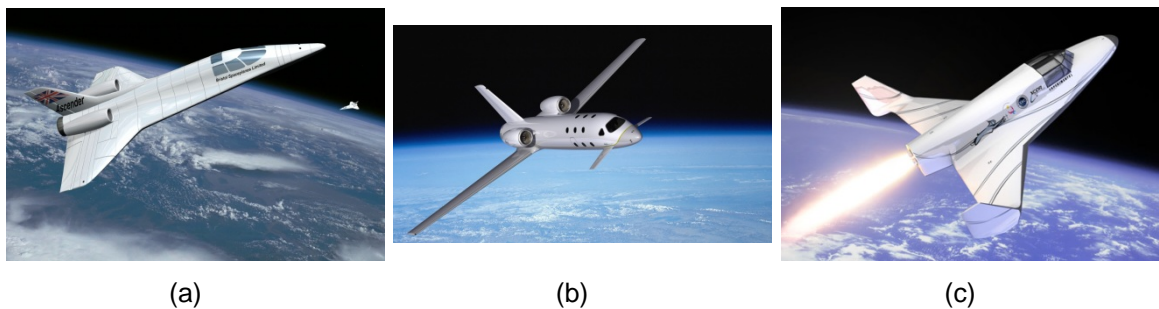


Figure 1.9: BSP Ascender (a), EADS Spaceplane (b), XCOR Lynx (c)

Table 1.1 provides an overview over selected concepts.





	X-COR Lynx 	EADS SpacePlane 	Virgin Galactic SS2 	BSP Ascender 
Crew + Passengers	1+1	1+4	2+6	1+2
Max. Altitude	100 km	100 km	110 km	100 km
Max. Mach Number	3	3	3.5	3
Max. Acceleration	4.5g	4.5g	6g	6g
Propulsion System	Rocket	Turbojets, Rocket	Rocket	Turbojets, Rocket
Takeoff/Landing	HTHL	HTHL	Air Launch, Glide Landing	HTHL
Cost/seat	95k\$	200k€	200k€	100k\$

Table 1.1: Main features of vehicle concepts for Space Tourism

Recent survey studies assessed the potential market for sub-orbital vehicles [6,7]. The one performed by EADS and IPSOS shows that there is a sizable market for sub-orbital tourism and that people willing to pay around 200 k€ for that could be in the order of 50000, just 16 years after the market start. This market is of course much larger than the one related to orbital Space tourism missions on the International Space Station (ISS). In this case, in fact, only 7 people had the opportunity, up to now, to perform this experience paying from 20 M\$ to 40 M\$. It is obvious that these fares can be paid only by the so called Ultra High Net Worth Individuals (UHNWI).

Sub-orbital Space tourism may also be seen as an intermediate step towards a novel concept of orbital Space tourism, based on reusable winged vehicles. Indeed, the employment of reusable components could strongly reduce the cost per seat up to 2 orders of magnitude, depending on the number of flights scheduled. In addition, the development of a winged re-entry vehicle could represent a safer and more comfortable way to cross the atmosphere [8].

1.2.2 Super-hypersonic point-to-point transportation

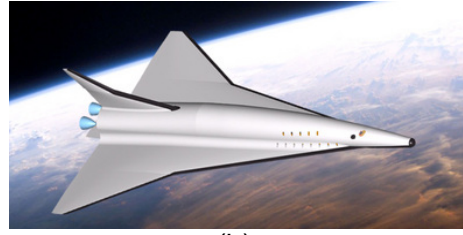
In the faster and faster business world of today, no SuperSonic Business Jet (SSBJ) is currently available, although several research and development programs for commercial aviation have been proposed in recent years. The civil large scale SuperSonic Transport (SST) aircrafts Tupolev Tu-144 and Concorde had relatively high costs, high noise, high fuel consumption and some environmental concerns.

Thanks to some recent research programs such as the QSP (Quiet Supersonic Platform) project sponsored by the American DARPA (Defense Advanced Research Projects Agency) and the EU funded LAPCAT and FAST 20XX, technologies to solve the main issues of supers-hypersonic flights have been developed.

The LAPCAT (Long-Term Advanced Propulsion Concepts and Technologies) A2 vehicle is designed to carry 300 passengers from Brussels to Sydney in 2-4 hours. The vehicle is powered by the Scimitar hypersonic air-breathing engine, conceived by Reaction Engines Limited, using liquid hydrogen fuel and able to sustain Mach 5 flight. In the FAST (Future high-Altitude high-Speed Transport) 20XX research project two vehicle concepts have been investigated by DLR (German Aerospace Center). The second concept, SpaceLiner, is a fully-reusable two-stage rocket-powered vehicle, which accommodate about 50 passengers. The aircraft offers ultra-fast point-to-point transportation along long distances (maximum Mach number of 25 and range up to 18000 km) and is able to takeoff and land horizontally.



(a)



(b)

Figure 1.10: EU funded projects: LAPCAT A2 (a), FAST20XX SpaceLiner (b)

In recent years American and European private enterprises and institutions have started to invest in projects regarding new-generation high performance super-hypersonic vehicles. The most relevant are shown below.

The Gulfstream X-54 project is intended to produce an experimental supersonic aircraft able to produce a low sonic boom, taking advantage of the technologies developed by NASA in the last decades. The vehicle, designed to perform cruise at a Mach number over 1.4 and at an altitude above 50000 feet (~15.2 km), is intended to provide enough data to reform national and international regulations on supersonic over-land flight.

The Quiet SuperSonic Transport (QSST) is a project by Supersonic Aerospace International (SAI) to develop a commercial supersonic business jet able perform cruise at a Mach number of 1.6-1.8 and an altitude of 60000 feet (~18.3 km), with a range of 4,600 miles (~7400 km). The two-engine gull-wing aircraft would create a sonic boom only 1% as strong as that generated by the Concorde. The Lockheed Martin began developing the vehicle in 2001 under a \$25-million contract from SAI, which has planned to achieve first flight in 2017 and begin customers' deliveries by 2018. The price per aircraft was expected to be about \$80 million.

The Aerion SSBj and the Spike S-512 are two concepts for a supersonic business jet, designed by the American enterprises Aerion Corporation and Spike Aerospace, respectively.

Both the vehicles, if produced, would allow travels from Europe to North American in few hours. Aerion Corporation plans flight testing to begin in 2019 and the first aircraft to reach the market in 2021. The price per vehicle is expected to be \$80 million, with development costs ranging from \$2.5 to \$3.0 billion.

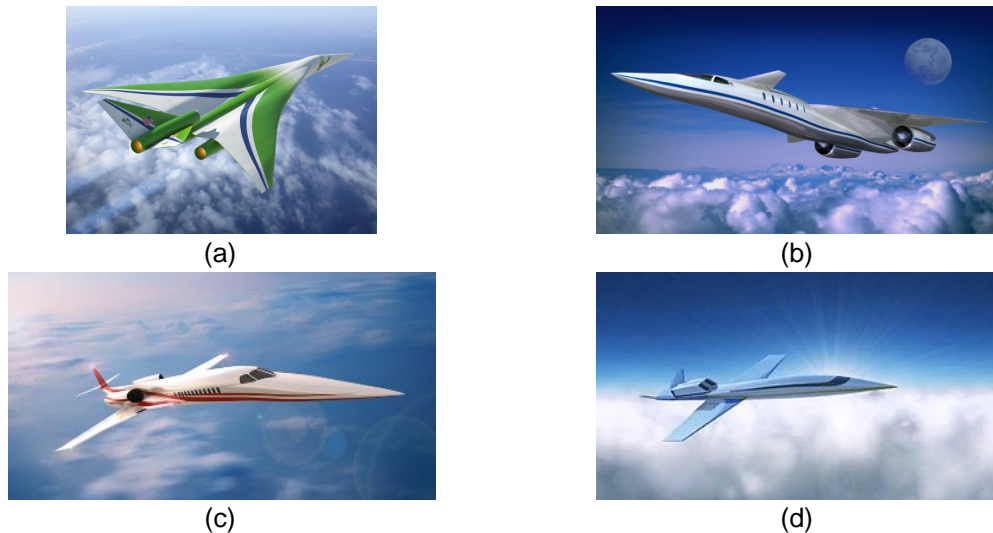


Figure 1.11: Concepts for supersonic business jets:
Gulfstream X-54 (a), SAI QSST (b), Aerion SSBJ (c) and Spike S-152 (d)

The HiSAC (High Speed AirCRAFT) project brings together 37 partners coordinated by Dassault Aviation. The project is aimed to evaluate the feasibility of a small supersonic business jet that would meet future environmental standards concerning sonic boom and atmospheric emissions.

SoniStar is a supersonic passenger business jet proposed by the company HyperMach Europe Aeronautics. The vehicle would carry 32 passengers in luxury accommodation, reaching speeds of up to Mach 4.4 and altitudes of 60000 feet (~18.3 km). Sonic boom is intended to be avoided through electromagnetic drag reduction technology, currently not existing.

In the ZEHST (Zero Emission Hyper Sonic Transport) project, EADS and Japan are developing an environmentally friendly hypersonic passenger aircraft. Powered by two turbofans (for takeoff and up to Mach 0.8), rocket boosters (up to Mach 2.5) and two ramjets, the vehicle would reach an altitude of 32 km and Mach number of 4-5. The aircraft would carry 50-100 passengers and be able to takeoff and land on current airport runways. ZEHST is envisaged to fly by 2050, from London to Japan in less than 3 hours.

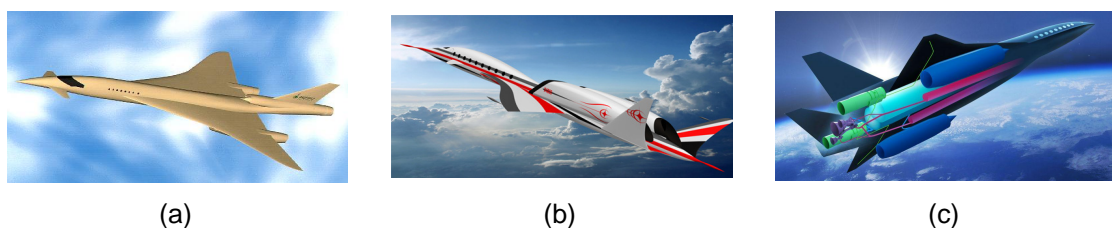


Figure 1.12: Concepts for super-hypersonic vehicles:
Dassault Aviation HiSAC (a); SoniStar (b); ZEHST (c)

Table 1.2 provides an overview over various vehicle concepts for super-hypersonic point-to-point transportation. All these projects show that several worldwide companies operating in the aerospace industry are confident in the strong, long-term potential of intercontinental aircrafts for different applications. Bombardier Aerospace forecast a total of 24000 business jet deliveries from 2013 to 2032 in the business jet segment, which represents approximately \$650 billion in industry revenues. North America is expected to receive the greatest number of new business jet deliveries, followed by Europe and China. It is also expected that key growth markets including Brazil, India, Russia/the Commonwealth of Independent States (CIS), Mexico, and Turkey will receive a significant share of business jet deliveries during the next 20 years. If only 1% of the mentioned market would simply pass to high supersonic/hypersonic transportation sector, i.e. 240 deliveries with \$6 billion revenues, it would comply with almost all the market studies performed during the last decade on the supersonic business jet market segment.









		Passengers	Cruise Altitude	Cruise Mach Number	Down-Range	Propulsion System
Gulfstream X-54		12	15.2 km	1.4	-	Turbofans
Aerion SSBJ		18	15.5 km	1.6	7400 km	Turbofans
Spike S-152		18	18.3 km	1.6	7400 km	Turbofans
HiSAC		16	20 km	1.8	9000 km	Turbofans
QSST		12	18.3 km	1.8	7400 km	-
HyperMach SoniStar		32	18 km	4.4	-	S-MAGJET
ZEHST		50-100	32 km	5	9000 km	Turbofans Rocket Ramjets
LAPCAT A2		300	25 km	5	20000 km	Scimitar Engines

Table 1.2: Main features of vehicle concepts for super-hypersonic transportation

References

- [1] T.A. Heppenheimer, Facing the Heat Barrier: a History of Hypersonics, The NASA History Series (2007)
- [2] R. P. Hallion, The Hypersonic Revolution: Case Studies in the History of Hypersonic Technology, U.S. Air Force (1987-1988)
- [3] D. Ashford, An aviation approach to Space transportation, The Aeronautical Journal 113: 499-515 (2009)
- [4] G. Russo, Next Generations Space Transportation Systems, Aerotecnica Missili e Spazio, 81: 65-72 (2002)
- [5] T. Le Goff, A. Moreau, Astrium suborbital spaceplane project: Demand analysis of suborbital space tourism. Acta Astronautica 92: 144-149 (2013)
- [6] The Tauri Group, Suborbital Reusable Vehicles: A 10-Year Forecast of Market Demand (2012)
- [7] C. Lauer, D. Faulkner, M. Onuki, J. Crisafulli, Suborbital Spaceplane Vehicle Development Programs for Future Point-to-Point Transportation Services, International Astronautical Federation (2009)
- [8] R. Monti, D. Paterna, A low risk reentry: looking backward to step forward, Aerospace Science and Technology, 10: 156-167 (2006)

2 HyPlane vehicle

The increasing number of projects regarding airplane-like vehicles for Space tourism and super-hypersonic point-to-point transportation perspectives induce to reasonably expect the aviation to include in the near future very high speed systems. In this scenario University of Naples “Federico II”, in the wider frame of the Space Renaissance (SR) Italia Space Tourism Program [1] and with the support of other universities and small and medium enterprises (including Polytechnic of Turin and BLUE Engineering) is investigating a new concept for a small passenger hypersonic airplane (named HyPlane) of six seats, for long-duration sub-orbital Space tourism missions and point-to-point medium range hypersonic transportation [2,3,4,5,6].

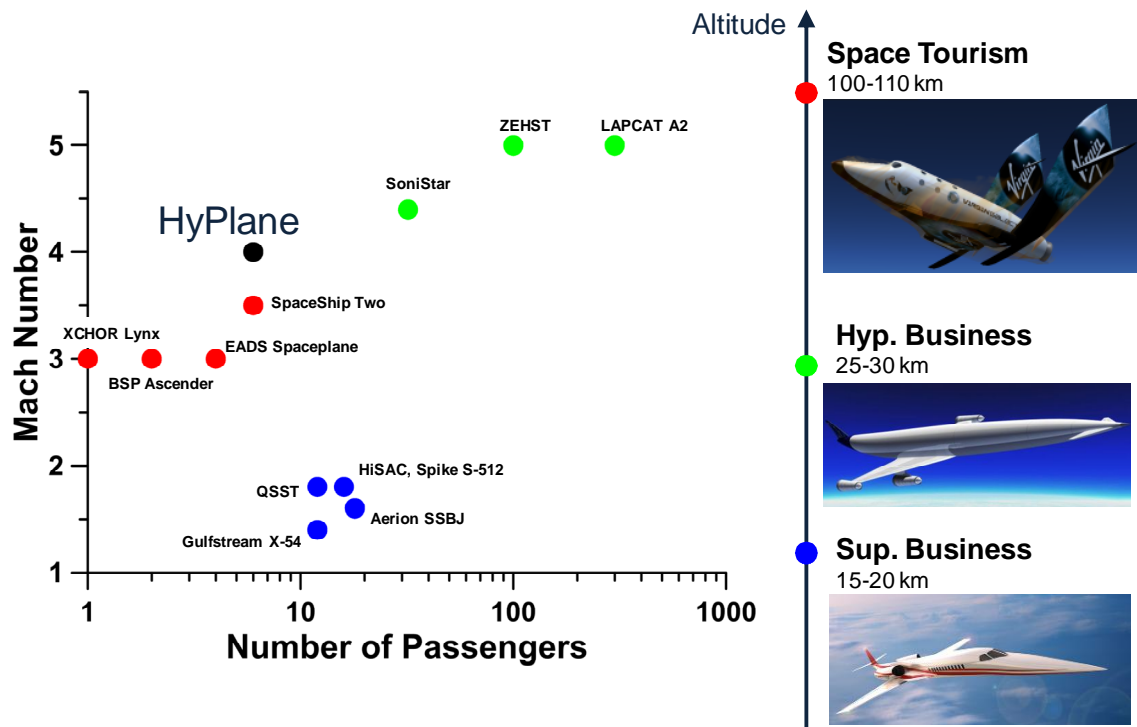


Figure 2.1: Vehicle concepts for Space tourism and super-hypersonic point-to-point transportation

In this chapter the vehicle system concept is presented. Main aerodynamic features, propulsion system and the potential mission scenarios are discussed, pointing out the main applications and opportunities offered to travellers.

2.1 System concept

HyPlane is designed for long-duration sub-orbital Space tourism missions which offer short and repeated periods of low-gravity, in the high stratosphere where a large view of the Earth is ensured. The vehicle is also consistent with a point-to-point medium range hypersonic transportation and will operate on short-medium length runways of existing even small airports, since it is intended to takeoff and land horizontally with relatively small speed and landing loads. Most of the previous and actual studies concerning super-hypersonic civil transport aircraft designs have tended toward large aircrafts, characterized by hundreds of tons of mass and hundreds of passengers. This has resulted in great difficulty in determining a valid and sustainable operational concept, because of the system high complexity, requiring very long time to reach the sufficient technology readiness level. The development of a small hypersonic plane (of the size of an executive jet) may open new markets and applications, such as “urgent business travel”, taxi aircraft for persons, specific goods, human organs and so forth. Figure 2.2 illustrates a vehicle preliminary configuration.



Figure 2.2: Artistic rendering of HyPlane hypersonic vehicle

The design of such a hypersonic airplane is based on the concept of integrating available technologies developed for aeronautical and space atmospheric re-entry systems. The vehicle conceptual design is defined by the complex interplay of aerodynamics, atmospheric heating, materials and structures, propulsion, fuel selection, cabin, tank and subsystems sizing. The flight envelope covers subsonic, transonic, supersonic and hypersonic flight regimes, being hypersonic the most challenging one, constrained on the lower boundary by heating and material limits, and on the upper boundary by aerodynamic lift and propulsion performance.

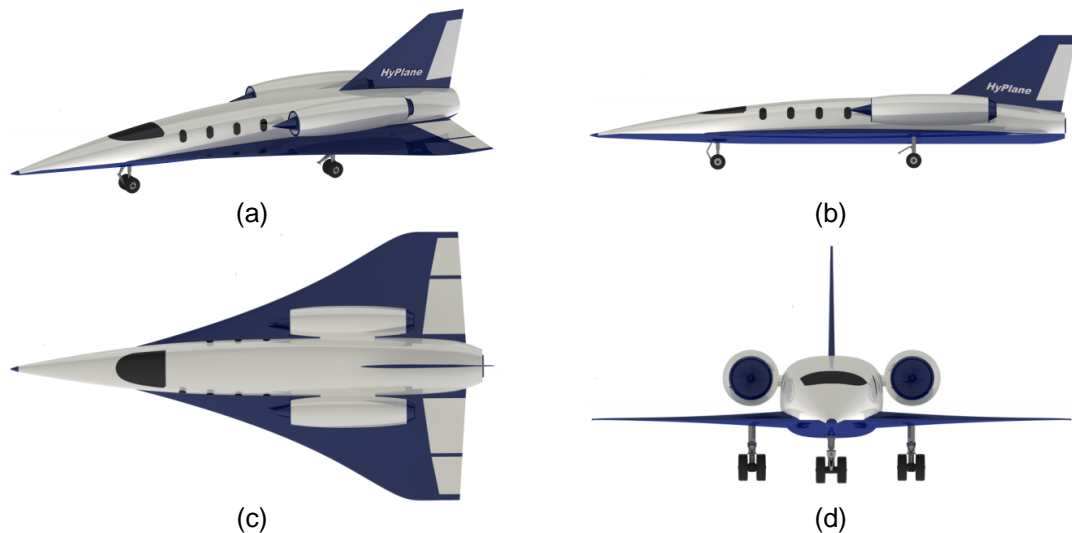


Figure 2.3: Perspective (a), side (b), top (c), front (d) views of HyPlane

The airframe consists of a fuselage, a high performance variable-delta wing with four elevons, both internal and external. If deflected symmetrically, the four elevons provide pitch control, while asymmetric deflections of the external elevons (ailerons) provide roll control. It also features a vertical tail, with a moveable rudder, for directional control. The fuselage is separated in different compartments. A pressurized compartment holds the cockpit from which a pilot and a co-pilot and a cabin for the accommodation of six passengers. Unpressurized compartments hold the tricycle landing gear, the subsystems and the propellant tanks.

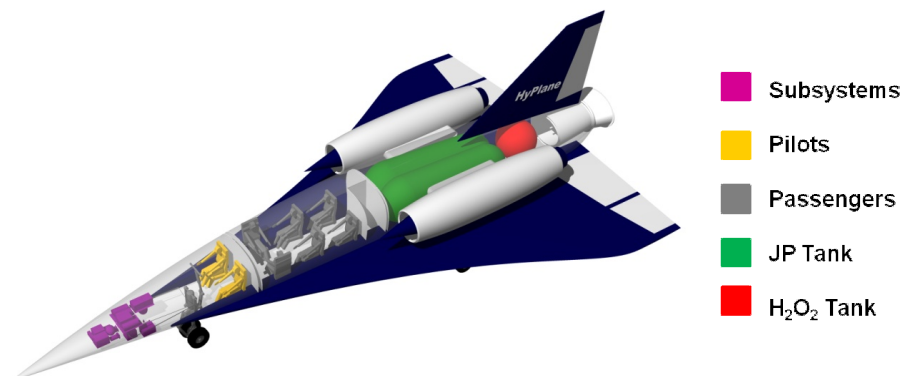


Figure 2.4: HyPlane internal layout

The vehicle, powered by Turbine Based Combined Cycle (TBCC) engines plus a throttleable Rocket, is characterized by a relatively high aerodynamic efficiency and low wing loading.

As it is in most hypersonic planes designs, the aircraft needs to have a relatively high lift-to-drag ratio, for different reasons. First, the requirement to fly in the atmosphere using also rocket engines forces the designers to minimize the required thrust, so that the propellant mass at takeoff can be small. Second, the high aerodynamic efficiency

guarantees the maximization of the range with the minimum fuel consumption, crucial in the hypersonic cruise scenario. Third, the manoeuvring performances are improved if the aircraft has a high enough lift-to-drag ratio.

The low wing loading makes possible a high altitude flight, which offers a better Earth view and may open to new applications (e.g. remote sensing, high altitude technological demonstrations, etc.).

The wing area is large enough to aerodynamically sustain the aircraft gross takeoff weight with relatively low velocities and to reduce, at relatively high altitudes, aerodynamic heating and sonic boom during cruise and supersonic descent approach (efficient overland routes) and the consequent environmental impact.

The vehicle main geometric characteristics are reported in Table 2.1.

Geometric parameters	
Fuselage length [m]	23.6
Nose Radius of Curvature [m]	0.03
Wing Area [m ²]	140
Wing Span [m]	13.5
Aspect Ratio	1.3
Wing Chord at Root [m]	16.7
Wing Chord at Tip [m]	2.5
Wing Mean Aerodynamic Chord [m]	12
Vertical Tail Span [m]	3.6
Vertical Tail Area [m ²]	14
Vertical Tail Chord at Root [m]	6.4
Vertical Tail Chord at Tip [m]	1.8
Vertical Tail Sweep [deg]	57
Internal Elevons Area [m ²]	10.3
External Elevons Area [m ²]	4.9
Rudder Area [m ²]	3.0

Table 2.1: HyPlane main geometric features

Wing and vertical tail airfoil is presented in Figure 2.5. A symmetrical thin airfoil with blunt leading edge, suitable for both hypersonic cruise and high aerodynamic load manoeuvres, has been chosen. Table 2.2 summarizes airfoil main geometric features, assuming a chord of 1 m.

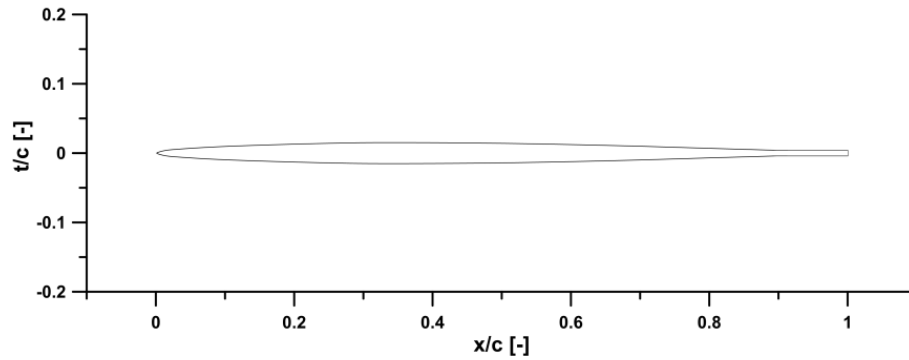


Figure 2.5: HyPlane wing and vertical tail airfoil

Airfoil geometric parameters (Chord=1m)	
Leading edge radius of curvature [m]	0.0007
Maximum thickness [m]	0.03
Maximum thickness location [m]	0.3

Table 2.2: Main geometric features of wing and vertical tail airfoil

2.2 Propulsion System

2.2.1 Turbine-Based Combined Cycle engines

HyPlane takes advantage from state-of-the-art airbreathing hypersonic propulsion. Current design is based on combined-cycle engines, capable of operating in multi-modes and then extremely versatile and efficient in different flight conditions.

In particular the vehicle is powered by two Turbine-Based Combined Cycle (TBCC) engines. A TBCC engine is essentially a combination of a low-speed turbine engine and higher speed ramjet, to achieve maximum performance [7]. The TBCC engines operate by using a gas turbine propulsion cycle that passes to a ramjet cycle at high Mach number. In this condition, in fact, the air-flow bypasses the turbomachinery, because pressure, temperature, and flow velocity would make such turbine impractical, redundant, or both.

An example of operative TBCC engine is the J58 utilized in the Lockheed SR-71 Blackbird, working in multiple cycles depending on the flight regime. More recent advanced hypersonic systems, such as the DARPA Blackswift, have been proposed using TBCC-class propulsion system [8].

In the present work a conceptual Mach 4 TBCC developed by AFRL (Air Force Research Laboratory) has been considered. The engine deck provided uninstalled thrust and specific impulse information, for the JP-4 hydrocarbon fuelled engine, as a

function of flight altitude and Mach number [9]. Figure 2.5 shows the deduced maximum thrust and the specific impulse as a function of Mach number for different altitudes.

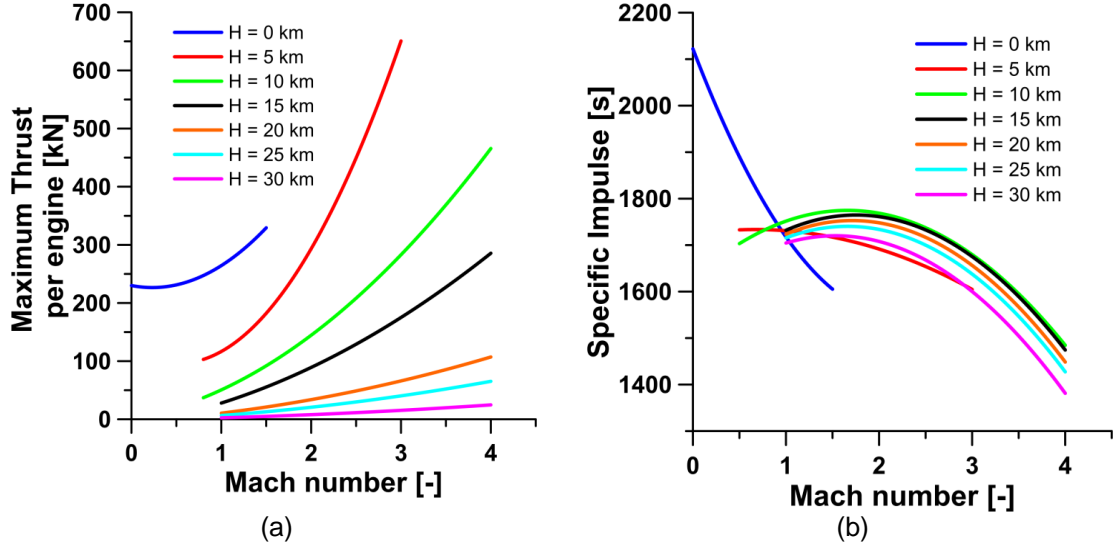


Figure 2.6: Performances of Turbine-Based Combined Cycle : maximum thrust per engine (a) and specific impulse (b) as a function of Mach number at different altitudes

2.2.2 Rocket engine

HyPlane is powered also by a throttleable rocket, which guarantees adequate propulsive characteristic to fly sub-orbital trajectories and is based on the utilization of hydrogen peroxide (H_2O_2) as oxidizer, which has several advantages.

In particular this engine offers the versatility of operating in monopropellant mode (offering a small thrust for attitude control) and bipropellant mode, using Kerosene as fuel. The high available thrust offered by the latter mode is crucial in a Space tourism mission scenario, where high accelerations are necessary to perform sub-orbital jumps. Since the H_2O_2 decomposes into a mixture of superheated steam and oxygen to a temperature of about 1000 K, a propulsion unit without a requirement for a separate ignition system offers a higher system reliability.

Moreover the H_2O_2 is considered a green propellant due to the reduced emissions and the low toxicity, ensuring a very limited environmental impact. The average performances of the rocket identified for this work are shown in Table 2.3.

Average Thrust [kN]	Average Specific Impulse [s]
200	310

Table 2.3: Rocket engine main performances

2.3 Preliminary mass budget

A preliminary mass budget has been elaborated in order to assess the feasibility of the vehicle configuration, according to the main mission requirements. The study is based on both statistical correlation and engineering design of specific subsystems.

These models, taking also into account heavier vehicles designed in past years, provide preliminary results, which can be useful in the first stages of the iterative design process.

The following assumptions have been made in order to obtain the vehicle mass budget and the mass breakdown among its main subsystems:

1. The fuel weight depends on the aircraft configuration and on the mission requirements. In particular an overall fuel weight of 16 tons has been considered necessary for the hypersonic medium range point-to-point mission.
2. The vehicle empty weight can be estimated from statistics on the basis of the HASA model proposed in literature [10].
3. The crew and passengers weights have been determined considering the worst case scenario of all adult and male passengers travelling in winter (i.e. 100 kg per person, according to the Federal Aviation Administration).

According to the considered model, the overall vehicle weight has been computed by iteratively solving a number of equations for different parameters, including the total volume and the total gross weight of the vehicle.

The different steps include:

1. The assignment of proof values for some parameters, in particular total volume and total gross weight of vehicle.
2. The comparison between the assigned and the computed value of each parameter.
3. The iteration until a sufficient accuracy is reached.

After having added a proper mass design margin, the method has an overall accuracy around 20% for the total gross mass estimation, while the errors regarding the mass breakdowns are estimated to be larger.

The predicted takeoff weight of the aircraft is about 26.3 tons. In Figure 2.7 the total vehicle mass breakdown and the structural mass distribution are reported.

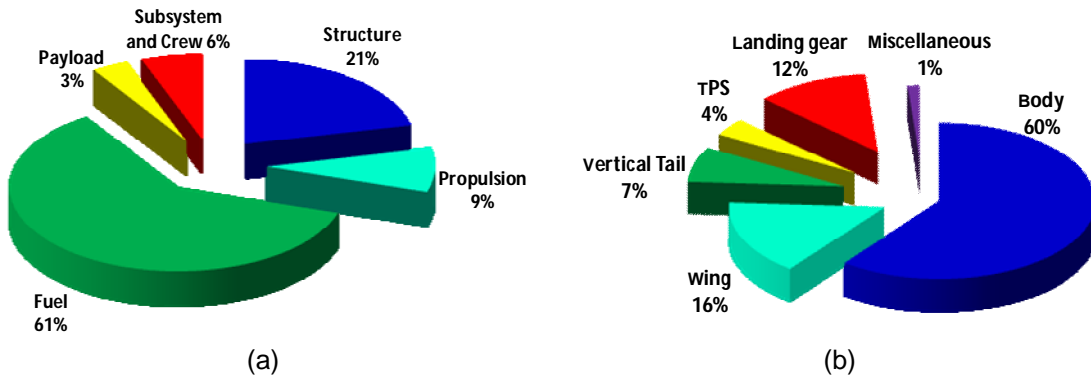


Figure 2.7: Total (a) and structural (b) mass breakdowns

As the propellant is consumed during the flight, the vehicle center of gravity, estimated taking advantage of a CATIA tool [11], has a significant longitudinal excursion while it is possible to neglect its vertical position variation. In particular it moves forward of about 2 m: the CoG is approximately located at 16 m and at 14 m from the apex of the nose, at takeoff and at zero-fuel condition, respectively (Figure 2.8).

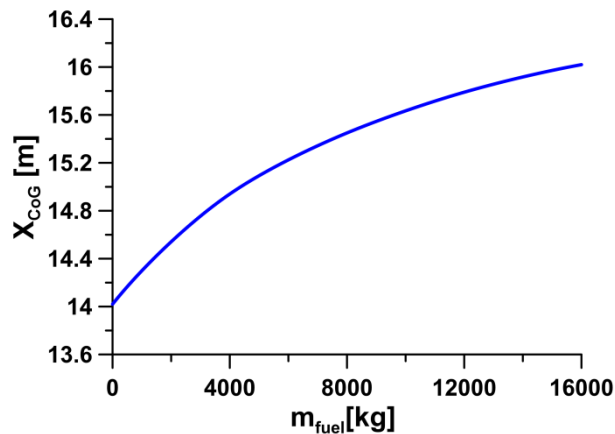


Figure 2.8: Vehicle CoG longitudinal excursion as the propellant is consumed (from the apex of the nose)

2.4 Potential mission scenarios

HyPlane is designed to be able to realize long duration missions, both for Space tourism purposes and for hypersonic cruises over transcontinental distances (with a total range in the order of 6000 km). This can be achieved, as mentioned previously, optimizing the propulsion performances of the TBCC and the rocket in the different phases of the flight envelopes.

The HyPlane mission profile begins with a Horizontal Takeoff (HT) from a short-medium length runway, taking advantage from the two TBCC engines operating in turbojet mode and from the lift forces resulting from the relatively large wing surface.

Then, an ascent phase is performed to reach suitable conditions for the sub-orbital parabolic manoeuvres or for the hypersonic cruise. In particular this phase consists in

an initial subsonic ascent to altitude between 5 and 10 km and in a subsequent acceleration through trans-supersonic speed range and climbing along a constant dynamic pressure trajectory, using the TBCC engines. During the acceleration, when the aircraft reaches a sufficient altitude and speed, the engine operating mode undergoes a transition to ramjet.

Then the HyPlane performs its nominal mission, namely a sequence of 3 sub-orbital parabolas using the rocket engine, or the hypersonic cruise using the TBCC operating in ramjet mode, with a total range of 6000 km.

After that, the aircraft performs a gliding descent, a powered approach to the terminal area and, finally, a Horizontal Landing (HL) on a conventional runway.

The total duration of the mission in both cases is less than 2 hours.

In summary, the mission specifications include:

1. HT with TBCC operating in turbojet mode
2. Subsonic ascent to altitudes between 5 and 10 km
3. Acceleration through the trans-supersonic speed range and climbing along a constant dynamic pressure trajectory (the TBCC operating mode undergoes a transition to ramjet)
4. Sequence of 3 sub-orbital parabolas (using rocket engine) or hypersonic cruise
5. Gliding descent, powered approach and HL

In an early conceptual phase, mission trajectories have been computed considering the dynamic equations of motion for a point mass characterized by three degrees of freedom, before considering a six degrees of freedom model (Chapter 7). The set of first order nonlinear ordinary differential equations [12] has been numerically integrated at discrete time-steps and taking advantage of the Euler's method.

2.3.1 Space tourism mission

In a Space tourism mission scenario, similarly to subsonic airplanes performing parabolic flight, the HyPlane will be able to execute 3 sub-orbital jumps, each providing up of a couple of minutes of low gravity. During this period passengers will experience weightlessness conditions, enjoying a beautiful view of the Earth from the Space.

Before each sub-orbital jump, the vehicle begins flying at hypersonic speed in a steady horizontal attitude, at a Mach number of 4 and at an altitude of 30 km. During this steady flight the gravity level is 1g.

Then the airplane gradually pulls up the nose and starts accelerating along a climbing trajectory with flight path angle up to 20°. During this phase the passengers experience

conditions of increased acceleration (~ 3 to 4 g), immediately prior to the two minutes of low-gravity. The peak of the sub-orbital trajectory is achieved below 70 km altitude. The extended duration low-gravity period is followed by another manoeuvre characterized again by hyper-gravity conditions, before the aircraft again flies a steady horizontal path.

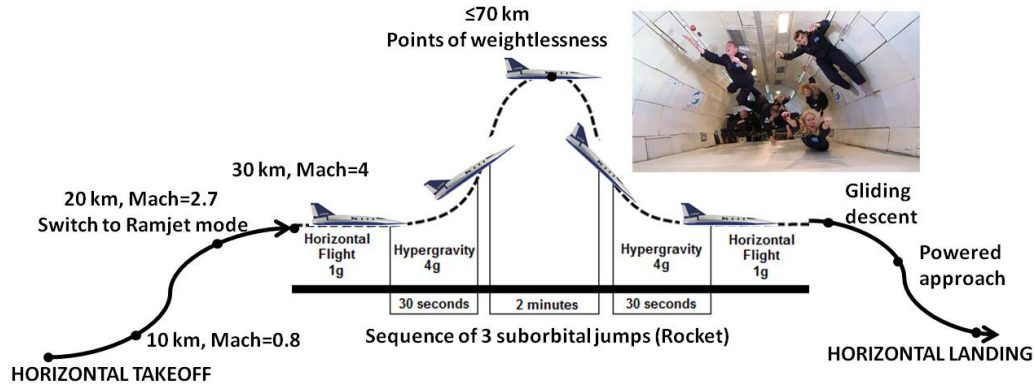


Figure 2.9: Space tourism mission scenario

The downrange for each sub-orbital jump is about 300 km. In Figure 2.10 a possible parabolic trajectory is shown along with the corresponding Total Sensed Acceleration (TSA), the thrust provided by the Rocket engine and the consumed mass profiles.

The described scenario offers the opportunity to execute microgravity research under relatively extended duration and repeated low-gravity conditions, offering the chance for human, biological and physical research in preparation for long-duration missions onboard orbital Space laboratories.

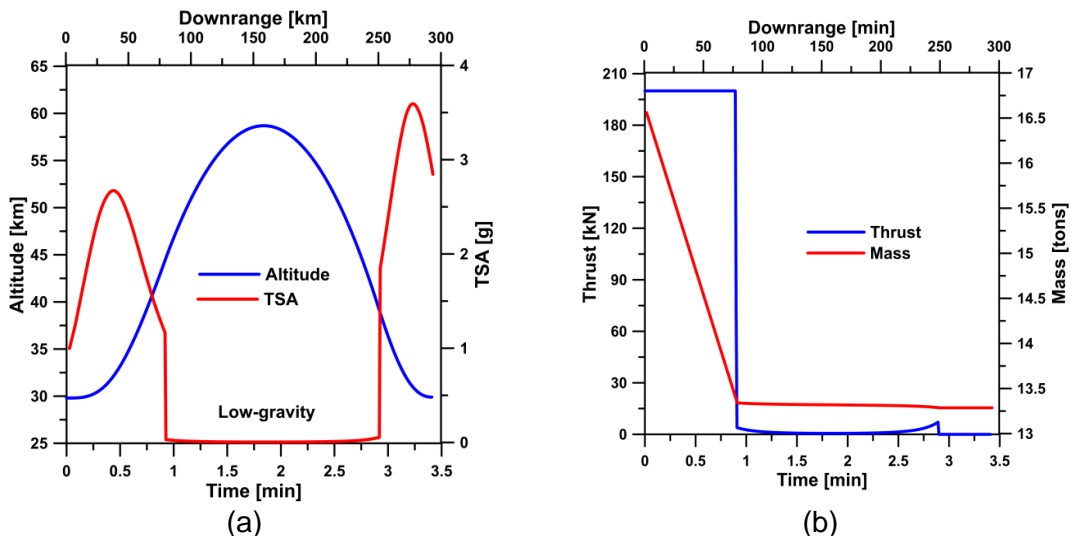


Figure 2.10: HyPlane performances along a possible sub-orbital parabola trajectory. Altitude and Total Sensed Acceleration (TSA) profiles (a); thrust provided by the rocket engine and mass variation profiles (b)

2.3.2 Hypersonic cruise mission

In a hypersonic point-to-point scenario the vehicle accelerates along a constant dynamic pressure flight path to the maximum Mach number (4-5).

The final altitude is reached after about 15 minutes, with a relatively low fuel consumption, due to the relatively high specific impulse of the TBCC operating as a turbojet.

The hypersonic cruise can be performed with a small flight path angle, to maintain the aerodynamic efficiency relatively high, in order to maximize the downrange.

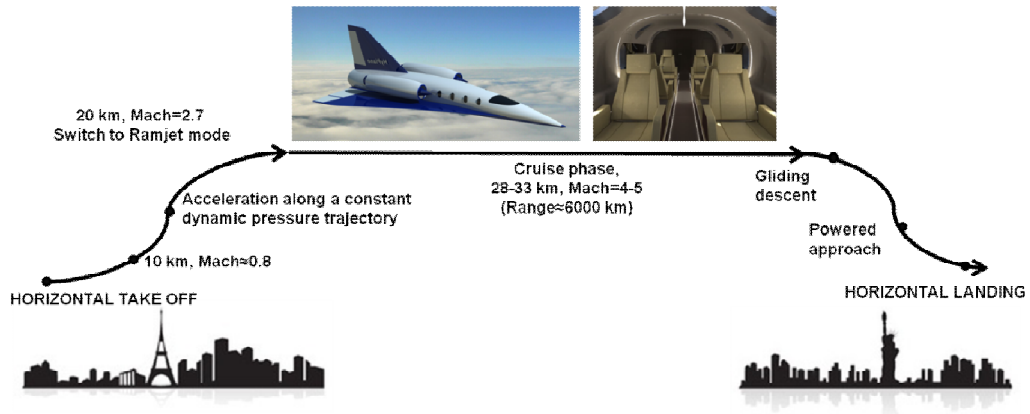


Figure 2.11: Hypersonic point-to-point mission scenario

In Figure 2.12 a possible hypersonic cruise trajectory is shown along with the corresponding Mach number and sonic boom profiles. Sonic boom has been estimated with the simplified formula

$$\Delta p = \frac{KW^{\frac{1}{2}}(M^2 - 1)^{\frac{3}{8}}}{MH^{\frac{3}{4}}}$$

where $K = 260 \frac{N}{m^2} \left(\frac{m^{\frac{3}{4}}}{N^{\frac{1}{2}}} \right)$ has been deduced from data of the Concorde and the Space Shuttle, W is the instantaneous weight of the vehicle, M is the Mach number and H is the altitude.

During cruise and supersonic descent approach the sonic boom felt on the ground is far below 100 Pa, ensuring a very limited environmental impact.

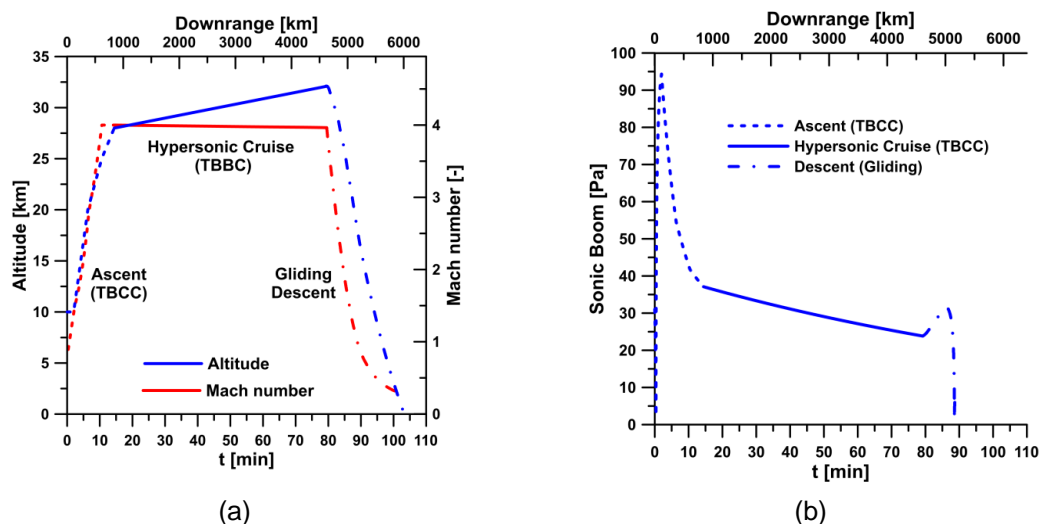


Figure 2.12: HyPlane performances along a possible hypersonic point-to-point trajectory. Altitude and Mach number profiles (a); sonic boom profile (b)

References

- [1] G. Russo, A. Autino, The Space Tourism Program of Space Renaissance Italia, 22nd Conference of the Italian Association of Aeronautics and Astronautics, Naples, Italy (2013)
- [2] R. Savino, G. Russo, V. Carandente, V. D'Oriano, Hyplane for Space Tourism and Business Transportation, Proceedings of the 22nd Italian Association of Aeronautics and Astronautics Conference, Naples (Italy), 9-12 September 2013, 12 pp.
- [3] V. Carandente, V. D'Oriano, A. Gallina, G. Russo, R. Savino, Aerothermodynamic and System Analysis of a Small Hypersonic Airplane (HyPlane), Proceedings of the 64th International Astronautical Congress, Beijing (China), 23-27 September 2013, 10 pp.
- [4] R. Savino, G. Russo, V. Carandente, V. D'Oriano, Hyplane: Challenges for Space Tourism and Business Transportation, Journal of Aeronautics & Aerospace Engineering, ISSN: 2168-9792 JAAE, Vol. 2(5), 8 pp. (2013)
- [5] R. Savino, G. Russo, V. Carandente, V. D'Oriano, HyPlane for Space Tourism and Business Transportation, Journal of the British Interplanetary Society, ISSN: 0007-084X JBIS, Vol. 67(2), 8 pp (2014)
- [6] R. Savino, G. Russo, V. D'Oriano, M. Visone, M. Battipede, P. Gili, Performances of a Small Hypersonic AirPlane (HyPlane), Proceedings of the 65th International Astronautical Congress, Toronto (Canada), 29 September -3 October 2014, 13 pp.
- [7] W. H. Heiser, D. T. Pratt, Hypersonic Airbreathing Propulsion Sonic, AIAA Education Series (1994)
- [8] K.J. Kloesel, N.A. Ratnayakey, C.M. Clarkz, A Technology Pathway for Airbreathing, Combined-Cycle, Horizontal Space Launch Through SR-71 Based Trajectory Modeling, 17th AIAA International Space Planes and Hypersonic Systems and Technologies Conference, San Francisco, California (2011)
- [9] M. A. Brock, Performance study of two-stage-to-orbit reusable launch vehicle propulsion alternatives (Master's Thesis), Air Force Institute of Technology, Wright-Patterson Air Force Base, Ohio (2004)
- [10] G.J. Harloff, B.M. Berkowitz, HASA-Hypersonic Aerospace Sizing Analysis for the Preliminary Design of Aerospace Vehicles, NASA Contractor Report 1822262 (1988)
- [11] CATIA V5 User manual, Dassault Systèmes (2009)
- [12] J. D. Anderson, Hypersonic and high temperature gas dynamics, McGraw-Hill Book Company (1989)

3 Aerodynamic models

The aerodynamic characteristics of the HyPlane can be evaluated with different tools. Computational Fluid Dynamic (CFD) simulations are generally very expensive in terms of computational effort, pre and post-processing time.

In fact a very high number of computational cells is necessary for a complete three dimensional compressible viscous analysis with radiative equilibrium boundary conditions. Moreover the grid generation for different configurations requires a long time, taking into account all possible deflections of control surfaces and engine integration. Furthermore the verification of results quality and the evaluation of aerodynamic performances need additional time.

In preliminary design phases the extensive application of complex CFD procedure is therefore prohibitive and more rapid and economical estimation of aerodynamic performances are frequently required. Engineering level nonlinear aerodynamic methods for estimating aerodynamic performances on traditional configuration aircraft (body-wing-tail geometries) in subsonic or supersonic regimes, can provide a relatively fast and accurate estimations of stability and control characteristics, for a wide range of Mach and Reynolds number, corresponding to several flight conditions.

The most popular codes utilized for these analysis are the software USAF Digital Stability and Control DATCOM (suitable for conventional configuration aircraft) and Missile DATCOM (specially developed for slender vehicles), written in Fortran language.

In this work both CFD simulations and Missile DATCOM software have been used to achieve the vehicle aerodynamic database. Missile DATCOM has been preferred over Digital, due to different reasons. Missile DATCOM provide outputs for all flight regimes while Digital is not able to provide several outputs for transonic and super-hypersonic regimes, for the configuration under investigation. Moreover Missile allows to model airbreathing engine intakes, unlike Digital. CFD simulations are necessary to accomplish a more accurate aerodynamic analysis and to characterize the vehicle also from an aero-thermodynamic point of view.

In this chapter the models adopted by Missile DATCOM software and CFD simulations are presented. In the first section the techniques implemented in Missile DATCOM, the approximations introduced in the vehicle model and the accuracy provided by the results are presented.

In the second section the formulations of the models adopted in the CFD simulations - namely the fluid-dynamic governing equations and the turbulence, laminar-turbulent transition and radiation models - are shown. Adopted computational grid and CFD solver are also described.

3.1 Missile DATCOM model

3.1.1 Techniques and accuracy

Missile DATCOM is a semi-empirical aerodynamic prediction code which offers the possibility to quickly and economically carry out aerodynamic performance analysis of conventional configurations of aircraft and missiles, with a predictive accuracy suitable for the conceptual and preliminary design phase.

The program combines approximate theoretical relationships and empirical data and provides good accuracy for traditional configurations.

The program is based on component build-up techniques, which calculates the aerodynamics of each component of the aircraft separately, then estimates the effects of the interactions between the various components and finally attempts to synthesize a solution for the complete configuration.

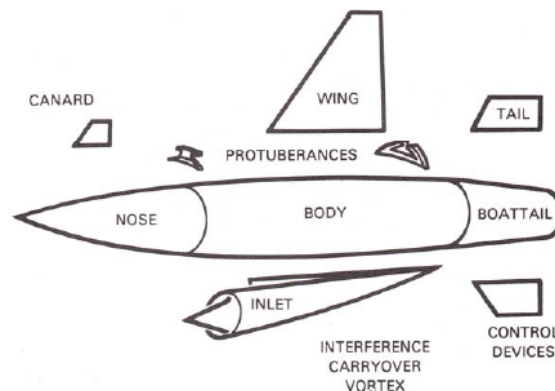


Figure 3.1: Component build-up technique

Computed data include aerodynamic force and moment coefficients, stability and control derivatives (longitudinal and lateral-directional, static and dynamic).

These results can be also obtained varying the flight parameters (angle of attack, sideslip angle, Mach number, altitude and control surface deflections) for subsonic, transonic, supersonic and hypersonic regimes.

The 1997 FORTRAN 90 version has been used for this study. The software requires a input file named for005.dat, written according to DATCOM syntax, containing the flight conditions and the geometry description of the vehicle and prints an output file which encompasses the aerodynamic parameters listed in Tables 3.1 and 3.2, all expressed in the body axes (Figure 3.2) except for the drag and lift coefficients.

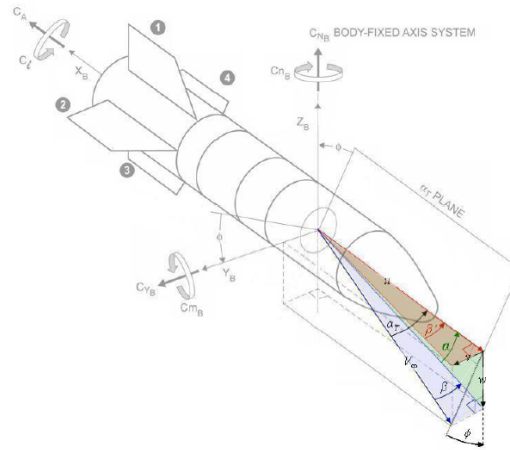


Figure 3.2: Missile DATCOM body axis system

Longitudinal Force and Moment Coefficients	C_A	Axial force coefficient
	C_N	Normal force coefficient
	C_D	Drag coefficient
	C_L	Lift coefficient
	C_M	Pitch moment coefficient
Longitudinal Static Derivatives	$C_{L\alpha}$	Lift coefficient derivative with angle of attack
	$C_{M\alpha}$	Pitching moment coefficient derivative with angle of attack
Longitudinal Dynamic Derivatives	$C_{L\dot{\alpha}}$	Lift coefficient derivative with rate of change of angle of attack
	$C_{M\dot{\alpha}}$	Pitching moment coefficient derivative with rate of change of angle of attack
	C_{Lq}	Lift coefficient derivative with pitch rate
	C_{Mq}	Pitching moment coefficient derivative with pitch rate

Table 3.1: Longitudinal aerodynamic parameters computed by Missile DATCOM

Lateral-Directional Force and Moment Coefficients	C_Y	Side force coefficient
	C_l	Rolling moment coefficient
	C_N	Yawing moment coefficient
Lateral-Directional Static Derivatives	$C_{Y\beta}$	Side force coefficient derivative with sideslip angle
	$C_{l\beta}$	Rolling moment coefficient derivative with sideslip angle
	$C_{N\beta}$	Yawing moment coefficient derivative with sideslip angle
Lateral-Directional Dynamic Derivatives	C_{Yp}	Side force coefficient derivative with roll rate
	C_{lp}	Rolling moment coefficient derivative with roll rate
	C_{lr}	Rolling moment coefficient derivative with yaw rate
	C_{Np}	Yawing moment coefficient derivative with roll rate
	C_{Nr}	Yawing moment coefficient derivative with yaw rate

Table 3.2: Lateral-directional aerodynamic parameters computed by Missile DATCOM

The methods implemented in the software to predict the aerodynamic parameters of the various components of the aircraft (body, fins, airbreathing engine inlets) and the effects of the interaction between them are summarized in Tables 3.3-6 [1].

BODY AERODYNAMIC METHODOLOGY			
AERODYNAMIC PARAMETER	SUBSONIC ($M<0.8$)	TRANSONIC ($0.8\leq M\leq 1.2$)	SUPER-HYPERSONIC ($M>1.2$)
Skin Friction Drag	Laminar: Blasius, Hoerner Fluid Dynamic Drag Turbulent: Van Driest II, MDAC (McDonnell Douglas Aircraft Company) West Handbook		
Pressure/Wave Drag	USAF DATCOM 4.2.3.1 (Hoerner Fluid Dynamic Drag)	Transonic Area Rule	SOSE (Second Order Shock Expansion) VDH (Van Dyke Hybrid) Hypersonic Newtonian Theory
Base Drag	Nose-Cylinder: NSWC (Naval Surface Warfare Center) charts Boattail: NASA TR-R100		
Axial force at angle of attack	Allens and Perkins Crossflow, Jorgensen		SOSE (Second Order Shock Expansion) VDH (Van Dyke Hybrid) Hypersonic Newtonian Theory
Potential Normal Force and Pitching Moment	Nose-Cylinder: Messersmitt-Bölkow-Blohm Boattail: NSWC (Naval Surface Warfare Center) charts		
Viscous Normal Force and Pitching Moment	Jorgensen viscous crossflow		
Dynamic Derivatives	Slender Body Theory, Ericsson		
Damping Derivatives	SPIN 73 code		

Table 3.3: Main methodologies implemented in Missile DATCOM for body aerodynamic parameters computation

FIN AERODYNAMIC METHODOLOGY			
AERODYNAMIC PARAMETER	SUBSONIC ($M < 0.6$)	TRANSONIC ($0.8 \leq M \leq 1.4$)	SUPER- HYPERSONIC ($M > 1.4$)
Airfoil Section	Weber		
Skin Friction Drag	Hoerner Fluid Dynamic Drag MDAC (McDonnell Douglas Aircraft Company) West Handbook USAF Datcom 4.1.5.1		
Pressure/Wave Drag	Hoerner		Potential Flow Theory
Base Drag	Empirical (NWL-TR-3018)		
Induced Drag	USAF DATCOM, section 4.1.5.2		
Potential Normal Force	USAF DATCOM, section 4.1.3.2 (Lowry-Polhamus)	R.A.S. (Royal Aeronautical Society) Data Sheets	USAF DATCOM, section 4.1.3.2
Viscous Normal Force	USAF DATCOM, section 4.1.3.3		
Pitching Moment	USAF DATCOM, section 4.1.4.2		
Dynamic and Damping Derivatives	Methods based on lifting surface theory for subsonic speeds and on linearized theory for supersonic speeds, Look-up Tables		

Table 3.4: Main methodologies implemented in Missile DATCOM for fin aerodynamic parameters computation

INLET AERODYNAMIC METHODOLOGY		
AERODYNAMIC PARAMETER	SUBSONIC ($M < 1$)	SUPERSONIC ($M > 1$)
Skin Friction Drag	Laminar: Blasius, Hoerner Fluid Dynamic Drag Turbulent: Van Driest II, MDAC (McDonnell Douglas Aircraft Company) West Handbook	
Pressure/Wave Drag	USAF DATCOM section 4.2.3.1, Transonic Area Rule	Supersonic Area Rule
Additive Drag		Engineering Method (AIAA 91-0712)
Potential Normal Force and Pitching Moment	Engineering Method (AIAA 90-3091)	
Viscous Normal Force and Pitching Moment	Jorgensen viscous crossflow	

Table 3.5: Main methodologies implemented in Missile DATCOM for inlet aerodynamic parameters computation

AERODYNAMIC PARAMETER	FIN-BODY SYNTHESIS AERODYNAMIC METHODOLOGY
Body-Fin Upwash	Empirical Correlation (AIAA 96-3395)
Fin-Body Carryover	Slender Body Theory (NACA-TR-1307)
Fin deflection	Slender Body Theory (AGARD-R-711)
Body Vortex	Empirical (NWC-TP-5761)
Fin Vortex	Line Vortex Theory (NACA-TR-1307)
Dynamic Derivatives	Equivalent Angle of Attack (AIAA 97-2280)

Table 3.6: Main methodologies implemented in Missile DATCOM for fin-body interference estimate

The ability of Missile DATCOM in predicting aerodynamic performances for various aircrafts and missile configurations has been studied in many research works [2,3,4]. Literature results have shown good agreement with experimental data, but have also revealed that this software is not able to provide accurate results for every configuration. Studies have shown that normal force is predicted with the minimal error, while the axial force is one of the most difficult aerodynamic forces to accurately predict. In particular, for body-wing-tail configurations, the normal force coefficient is expected to be predicted with an error lower than 9%, while the axial force and the pitching moment coefficients with error lower than 12% [2]. Both over and under prediction were observed. While the accuracy of specific quantities depends on input geometry and flight conditions, the overall accuracy of the code is deemed to be at a level suitable to support preliminary design studies.

3.1.1 HyPlane model

The methods implemented in Missile DATCOM encompass a wide range of configurations and flight conditions, according to their range of applicability requirements.

The HyPlane configuration includes a body (the fuselage), three fins (two wings and a vertical tail) and two airbreathing engines.

Unfortunately Missile DATCOM limitations do not allow reproducing exactly the real shape of the HyPlane. Indeed, a simplified shape, as similar as possible to the original geometry, has been modelled, according to the software limitations.

In particular some approximations have been introduced, for fuselage and wing. HyPlane fuselage complex shape has been modelled as an axisymmetric body, with elliptical cross-sections, since the used software version allows to model only axisymmetric bodies, with circular or elliptical cross-sections.

The variable delta wing has been modelled as a double delta wing, since the software allows reproducing only few sweep angles for each fin. HyPlane vertical tail has been exactly modelled, thanks to its simple shape. Wing and vertical tail airfoil has been defined by specifying upper and lower surface coordinates at different chord stations. The achieved model is presented in Figure 3.3.

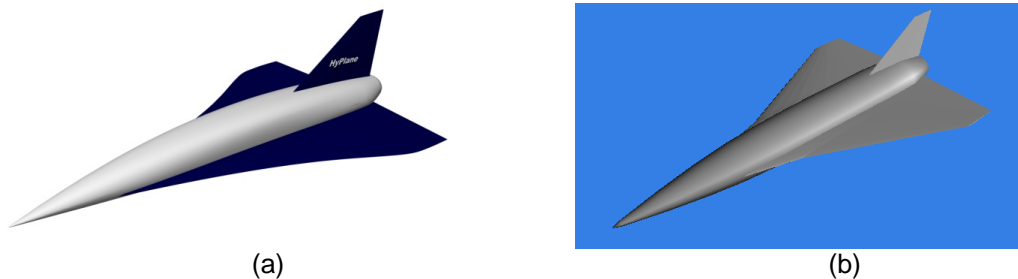


Figure 3.3: HyPlane clean configuration.
Original geometry (a) and Missile DATCOM model (b)

Also control surfaces have been modelled without any approximation. The axisymmetric inlets of the two airbreathing engines have been modelled by specifying the inlet ramp angle and cowl external diameter at five axial locations. The achieved complete model is presented in Figure 3.4.



Figure 3.4: HyPlane complete configuration.
Original geometry (a) and Missile DATCOM model (b)

Tables 3.7 and 3.8 show the range of applicability required by Missile DATCOM methods. It is possible to observe that HyPlane configuration and flight envelope can be quite good handled by Missile DATCOM.

Parameters		Priority 1	Priority 2	HyPlane
Angle of attack [deg]	α	$-20 \leq \alpha \leq 20$	$180 \leq \alpha \leq 180$	$0 \leq \alpha \leq 20$
Angle of sideslip [deg]	β	$-20 \leq \beta \leq 20$	$180 \leq \beta \leq 180$	$-20 \leq \beta \leq 20$
Mach number	M_∞	$0 \leq M_\infty \leq 6$	$0 \leq M_\infty \leq 10$	$0 \leq M_\infty \leq 6$
Body fineness ratio	$(l/d)_B$	$6 \leq (l/d)_B \leq 20$	$1 \leq (l/d)_B \leq 30$	$(l/d)_B = 7.9$
Nose fineness ratio	$(l/d)_N$	$0.5 \leq (l/d)_N \leq 5$	$0 \leq (l/d)_N \leq 7$	$(l/d)_N = 4$
Fin exposed span to diameter	$(b/d)_F$	$1 \leq (b/d)_F \leq 6$	$0 \leq (b/d)_F \leq 10$	Wing: $(b/d)_F = 1.8$ Vert. Tail: $(b/d)_F = 1.2$
Fin aspect ratio	AR	$0.6 \leq AR \leq 4$	$0.1 \leq AR \leq 10$	Wing: $AR = 1.3$ Vert. Tail: $AR = 0.93$
Fin planform		Triangular, trapezoidal	All	Wing: Double Delta Vert. Tail: Trapezoidal
Control method		All moveable fin	All	All moveable fin
Fin deflection incidence [deg]	δ	$0 \leq \delta \leq 30$	$0 \leq \delta \leq 60$	$0 \leq \delta \leq 30$
Reynolds number/ft	R_N	$3 \times 10^5 \leq R_N \leq 2 \times 10^7$	$10^3 \leq R_N \leq 3 \times 10^7$	$3 \times 10^5 \leq R_N \leq 2 \times 10^7$

Table 3.7: Missile DATCOM applicability to different geometric configurations and flight conditions

Geometric feature/ Flight condition		Subsonic	Transonic	Supersonic	HyPlane
Nose shape	Cone	V	V	V	Tangent Ogive
	Tangent Ogive	V	V	V	
	Other	?	V	V	
Nose bluntness	Sharp	V	V	V	Spherical
	Spherical	?	?	V	
	Truncated	X	X	V	
	Other	X	X	V	
Body configuration	Nose-Cylinder	V	V	V	Nose-Cylinder-Boattail
	Nose-Boattail	?	?	V	
	Nose-Flare	?	?	V	
	Nose-Cylinder-Boattail	V	V	V	
	Nose-Cylinder-Flare	?	?	V	
Body Fineness Ratio	$2 \leq l/d \leq 28$	V	V	V	$(l/d) = 7.9$
Body angle of attack	$0 \leq \alpha \leq 30$	V	V	V	$0 \leq \alpha \leq 20$
	Trapezoidal	V	V	V	
Fin planform	Double Delta - Cranked	V	V	V	Wing: Double Delta Vert. Tail: Trapezoidal
	Other	?	X	X	
Fin taper ratio	$0 \leq \lambda \leq 1$	V	V	V	Wing: $\lambda = 0.15$ Vert. Tail: $\lambda = 0.5$
Fin aspect ratio	$0.5 \leq AR \leq 4$	V	V	V	Wing: $AR = 1.3$ Vert. Tail: $AR = 0.93$
Fin airfoil section	Supersonic	V	V	V	User Defined
	NACA	V	V	X	
	Other	V	V	X	
Fin leading edge	Spherically blunted	V	V	V	Spherically blunted
Fin trailing edge	Non sharp	V	V	V	Non sharp
Fin angle of attack	$0 \leq \alpha \leq 60$	V	V	V	$0 \leq \alpha \leq 30$
Fins combination	Planar	V	V	V	Planar
	Cruciform	V	V	V	
	Other	?	?	?	

V : Application suitable ? : Application questionable/limited X: Does not apply

Table 3.8: Component build-up approach applicability to different geometric configurations

3.2 CFD Models

3.2.1 Fluid dynamic governing equations

The considered fluid dynamics governing equations take into account the effects of turbulence and compressibility. They are obtained properly averaging the compressible Navier-Stokes equations which express the conservation of mass, momentum and energy. The equations, in Cartesian integral form, for an arbitrary control volume V enclosed in the surface A with normal \underline{n} , may be written:

$$\begin{aligned} \frac{\partial}{\partial t} \int_V \rho dV + \oint_A \rho \underline{v} \cdot \underline{n} dA &= 0 \\ \frac{\partial}{\partial t} \int_V \rho \underline{v} dV + \oint_A \rho \underline{v} \underline{v} \cdot \underline{n} dA &= - \oint_A p \underline{I} \cdot \underline{n} dA + \oint_A \underline{\tau} \cdot \underline{n} dA \\ \frac{\partial}{\partial t} \int_V \rho E dV + \oint_A \rho H \underline{v} \cdot \underline{n} dA &= - \oint_A \underline{q} \cdot \underline{n} dA + \oint_A (\underline{\tau} \cdot \underline{v}) \cdot \underline{n} dA \end{aligned}$$

where:

- ρ, \underline{v}, p are the flow density, velocity vector and pressure
- $\underline{\tau}$ is the viscous stress tensor
- \underline{q} is the heat flux vector, given by the Fourier's law $\underline{q} = -k \underline{\nabla} T$, where k is the thermal conductivity and T is the flow temperature
- $E = e + \frac{1}{2} |\underline{v}|^2$ and $H = h + \frac{1}{2} |\underline{v}|^2 = E + \frac{p}{\rho}$ are the flow total energy and the total enthalpy, per unit mass, respectively, where e and h are the internal energy and the enthalpy, per unit mass, respectively.

The flow, considered an ideal gas, is also governed by the equation of state $p = \rho RT$.

Let $\phi(x, t)$ a dependent variable. The time (Reynolds) average and the Reynolds decomposition into the average and the fluctuation components are defined by:

$$\bar{\phi} = \frac{1}{T} \int_T \phi(x, t) dt, \quad \phi = \bar{\phi} + \phi'$$

The density weighted time (Favre) average and the Favre decomposition are defined by:

$$\tilde{\phi} = \frac{\overline{\rho \phi}}{\bar{\rho}}, \quad \phi = \tilde{\phi} + \phi''$$

The Favre-averaged Navier-Stoker (FANS) equations are obtained inserting the Reynolds decomposition for ρ and p , and the Favre decomposition for u, e and h into the governing equations and averaging them.

The resulting equations for the mean quantities are similar to the original equations, except for some additional terms:

- the viscous stress is augmented by the so-called Reynolds stress tensor

$$\underline{\underline{\tau_t}} = \overline{\rho \underline{v''} \underline{v''}}$$

- the heat flux is augmented by the so-called Reynolds heat flux $\overline{\rho \underline{v''} h''}$
- a term representing the transport for turbulent kinetic energy by turbulent velocity fluctuation and the work done by the viscous stress due to turbulent velocity fluctuation.

Using the Boussinesq approximation, the Reynolds stress tensor can be written as:

$$\underline{\underline{\tau_t}} = 2\mu_t \underline{\underline{S}} - \frac{2}{3}(\mu_t \underline{\nabla} \cdot \underline{v} + \rho k) \underline{\underline{I}}$$

where:

- μ_t is the eddy dynamic viscosity
- $\underline{\underline{S}} = \frac{1}{2} (\underline{\nabla} \underline{v} + \underline{\nabla} \underline{v}^T)$ is the strain rate tensor
- k is the turbulent kinetic energy

The fluid dynamic governing equations are closed by the Menter's Shear Stress Transport (SST) $k - \omega$ turbulence model, widely used in aerospace applications.

3.2.2 SST $k - \omega$ turbulence model

The $k - \omega$ turbulence model is based on two transport equations, for the turbulent kinetic energy k and the specific dissipation rate ω (identified as a frequency of the turbulence).

In the book by D.C. Wilcox [6] the original form of the model is discussed and comparisons with other turbulence models are presented. The main advantage of the $k - \omega$ model over the $k - \varepsilon$ model is its superior performance for boundary layers under adverse pressure gradients. The biggest disadvantage, in its original version, is a strong sensitivity to the values of ω in the free stream outside the boundary layer [7], a non-issue for the $k - \varepsilon$ model. This shortcoming was addressed by Menter, who combined the original $k - \omega$ model for use near walls and the $k - \varepsilon$ model away from walls using blending functions (which include functions of wall distance). In particular Menter transformed the ε transport equation into a ω transport equation, presenting a cross-diffusion term containing the dot product $\underline{\nabla} k \cdot \underline{\nabla} \omega$. Moreover Menter modified the eddy viscosity formulation to account for the transport effects of the principle turbulent

shear stress and dubbed the model containing this modification the SST (Shear-Stress Transport) $k - \omega$ model [8,9].

The transport equations, for k and ω are:

$$\begin{aligned} \frac{\partial}{\partial t} \int_V \rho k dV + \int_A \rho k \underline{v} \cdot \underline{n} dA = \int_A (\mu + \sigma_k \mu_t) \underline{\nabla} k \cdot \underline{n} dA + \\ + \int_V [\gamma_{eff} G_k - Y' \rho \beta^* f_{\beta^*} (\omega k - \omega_o k_o)] dV \end{aligned}$$

$$\begin{aligned} \frac{\partial}{\partial t} \int_V \rho \omega dV + \int_A \rho \omega \underline{v} \cdot \underline{n} dA = \int_A (\mu + \sigma_\omega \mu_t) \underline{\nabla} \omega \cdot \underline{n} dA + \\ + \int_V [G_\omega - \rho \beta f_\beta (\omega^2 - \omega_o^2) + D_\omega] dV \end{aligned}$$

The production of k and ω are computed as, respectively:

$$\begin{aligned} G_k &= \mu_t S^2 - \frac{2}{3} \rho k \underline{\nabla} \cdot \underline{v} - \frac{2}{3} \mu_t (\underline{\nabla} \cdot \underline{v})^2 \\ G_\omega &= \rho \gamma \left[\left(S^2 - \frac{2}{3} (\underline{\nabla} \cdot \underline{v})^2 \right) - \frac{2}{3} \omega \underline{\nabla} \cdot \underline{v} \right] \end{aligned}$$

where S is the modulus of the strain rate tensor \underline{S} .

D_ω is a cross-diffusion term, defined as $D_\omega = 2(1 - F_1) \rho \sigma_{\omega^2} \frac{1}{\omega} \underline{\nabla} k \cdot \underline{\nabla} \omega$.

The eddy turbulent viscosity is evaluated as $\mu_t = \rho k T$, with $T = \min \left[\frac{1}{\max(\omega, \frac{SF_2}{0.31})}, \frac{0.6}{\sqrt{3}S} \right]$.

F_1 and F_2 are blending functions, defined as:

$$\begin{aligned} F_1 &= \tanh(\arg_1^4), \arg_1 = \min \left[\max \left(\frac{\sqrt{k}}{0.09\omega y}, \frac{500v}{\omega y^2} \right), \frac{2k}{y^2 CD_{k\omega}} \right] \\ F_2 &= \tanh(\arg_2^2), \arg_2 = \max \left(\frac{2\sqrt{k}}{\beta^* \omega y}, \frac{500v}{y^2 \omega} \right) \end{aligned}$$

where $CD_{k\omega} = \max \left(\frac{1}{\omega} \underline{\nabla} k \cdot \underline{\nabla} \omega, 10^{-20} \right)$, $\beta^* = 0.09$ and y is the distance to the nearest wall.

The coefficients β , σ_k , σ_ω , γ are computed from the blending function F_1 , according to the equation (for the generic coefficient ϕ):

$$\phi = F_1 \phi_1 + (1 - F_1) \phi_2$$

where the coefficients ϕ_1 and ϕ_2 are:

$$\begin{aligned} \beta_1 &= 0.075, \sigma_{k1} = 0.85, \sigma_{\omega1} = 0.5, Y_1 = \frac{\beta_1}{\beta^*} - \sigma_{\omega1} \frac{K^2}{\sqrt{\beta^*}} \\ \beta_2 &= 0.0828, \sigma_{k2} = 1, \sigma_{\omega2} = 0.856, Y_2 = \frac{\beta_2}{\beta^*} - \sigma_{\omega2} \frac{K^2}{\sqrt{\beta^*}} \end{aligned}$$

with $K = 0.41$.

γ_{eff} is the effective intermittency and $\gamma = \min[\max(Y_{eff}, 0.1), 1]$. k_o and ω_o are the ambient turbulence values in source terms that counteract turbulence decay.

In order to evaluate the effects of compressibility, coefficients β and β^* are replaced by, respectively:

$$\begin{aligned}\beta_{comp} &= \beta - 1.5 \beta^* \max(M_t^2 - M_{t0}^2) \\ \beta_{comp}^* &= \beta^* [1 - 1.5 \max(M_t^2 - M_{t0}^2)]\end{aligned}$$

where $M_{t0}^2 = \frac{1}{4}$.

The SST $k - \omega$ model is particularly suitable for complex boundary layer flows under adverse pressure gradient and separation, typical phenomena of external aerodynamics. Moreover it is a prerequisite for the $\gamma - Re_{\theta}$ transition model, presented in the next section.

3.2.3 $\gamma - Re_{\theta}$ transition model

The $\gamma - Re_{\theta}$ transition model [10,11] is a correlation-based transition model specifically formulated for unstructured CFD codes.

The model is based on two transport equations, for the intermittency γ and for the transported transition momentum thickness Reynolds number $\overline{Re_{\theta t}}$. By the latter a correlation for the transition onset momentum thickness Reynolds number $Re_{\theta t}$ defined in the freestream is propagated into the boundary layer, through the variable $\overline{Re_{\theta t}}$. In this work the free stream has been defined in terms of an iso-value based on wall distance.

$$\begin{aligned}\frac{\partial}{\partial t} \int_V \rho \gamma dV + \int_A \rho \gamma \underline{v} \cdot \underline{n} dA &= \int_A \left(\mu + \frac{\mu_t}{\sigma_f} \right) \nabla \gamma \cdot \underline{n} dA + \int_V [P_\gamma - E_\gamma] dV \\ \frac{\partial}{\partial t} \int_V \rho \overline{Re_{\theta t}} dV + \int_A \rho \overline{Re_{\theta t}} \underline{v} \cdot \underline{n} dA &= \int_A \sigma_{\theta t} (\mu + \mu_t) \nabla \gamma \cdot \underline{n} dA + \int_V P_{\theta t} dV\end{aligned}$$

where:

$$\begin{aligned}P_\gamma &= F_{length} c_{a1} \rho S [\gamma F_{onset}]^{\frac{1}{2}} (1 - c_{e1} \gamma) \\ P_{\theta t} &= c_{\theta t} \frac{\rho U^2}{500\nu} (Re_{\theta t} - \overline{Re_{\theta t}}) (1 - F_{\theta t}) \\ E_\gamma &= c_{a2} \rho W \gamma F_{turb} (c_{e2} \gamma - 1)\end{aligned}$$

W is the modulus of the vorticity tensor $\underline{\underline{W}} = \frac{1}{2} (\nabla \underline{v} - \nabla \underline{v}^T)$ and U is the local velocity magnitude.

The transport equations are controlled by the following functions. In particular F_{length} and F_{onset} control the length and onset location of transition respectively, while F_{turb} and $F_{\theta t}$ control the boundary layer destruction and detector respectively.

$$\begin{aligned}
F_{onset1} &= \frac{Re_v}{2.193 Re_{\theta c}}, F_{onset2} = \min[\max(F_{onset1}^4, F_{onset1}), 2], \\
F_{onset3} &= \max[1 - \left(\frac{Re_T}{2.5}\right)^3, 0], F_{onset} = \max(F_{onset2} - F_{onset3}, 0) \\
F_{turb} &= \exp\left[-\left(\frac{Re_T}{4}\right)^4\right], F_{wake} = \exp\left[-\left(\frac{Re_\omega}{10^5}\right)^2\right] \\
F_{\theta t} &= \min\left\{\max\left[F_{wake} \exp\left(-\left(\frac{d}{\delta}\right)^4\right), 1 - \left(\frac{c_{e2}\gamma - 1}{c_{e2} - 1}\right)^2\right], 1\right\}
\end{aligned}$$

Re_v is the strain rate Reynolds number, Re_T is the turbulence Reynolds number. $Re_{\theta c}$ is the critical momentum thickness Reynolds number where the intermittency first appears in the boundary layer.

$$\begin{aligned}
Re_v &= \frac{\rho d^2 S}{\mu}, Re_T = \frac{k}{\nu \omega}, Re_\omega = \frac{\rho \omega y^2}{\mu} \\
\delta &= 50W \frac{d}{U} \delta_{BL}, \delta_{BL} = \frac{15}{2} \vartheta_{BL}, \vartheta_{BL} = \frac{\overline{Re_{\theta t} \nu}}{U}
\end{aligned}$$

The coefficients are defined as:

$$c_{a1} = 2.0, c_{a2} = 0.06, c_{e1} = 1.0, c_{e2} = 50, \sigma_f = 1.0, c_{\theta t} = 0.03, \sigma_{\theta t} = 2.0$$

The effective intermittency is obtained from:

$$\begin{aligned}
\gamma_{eff} &= \max(\gamma, \gamma_{sep}), \\
\gamma_{sep} &= \min\left[2 \max\left(\frac{Re_v}{3.235 Re_{\theta c}} - 1, 0\right) F_{reattach}, 2\right] F_{\theta t}, F_{reattach} = \exp\left(-\left(\frac{Re_T}{20}\right)^4\right)
\end{aligned}$$

Three correlations, for $Re_{\theta t}$, $Re_{\theta c}$ and F_{length} , close the $\gamma - Re_\theta$ transition model. The model was originally published incomplete [10], since only the correlation for $Re_{\theta t}$ was reported while the other two correlations were omitted.

In this work the correlation for $Re_{\theta t}$ developed by Menter et al. [10] and later revisited by Langtry [11] has been used. The missing correlations have been introduced via field function, using the two correlations derived from calibration against zero-pressure gradient flat plate data, by Suluksna et al. [12].

The correlation for $Re_{\theta t}$ has the following form:

$$\begin{aligned}
Re_{\theta t} &= \begin{cases} \left[1173.51 - 589.428 T_u + \frac{0.2196}{T_u^2}\right] F(\lambda_\theta, T_u); & T_u \leq 1.3 \\ 331.5(T_u - 0.5658)^{-0.671} F(\lambda_\theta, T_u); & T_u > 1.3 \end{cases} \\
F(\lambda_\theta, T_u) &= \begin{cases} 1 + \exp\left[-\left(\frac{2T_u}{3}\right)^{1.5}\right] (12.986\lambda_\theta + 123.66\lambda_\theta^2 + 405.689\lambda_\theta^3); & \lambda_\theta \leq 0 \\ 1 + 0.275 \exp(-2T_u) [1 - \exp(-35\lambda_\theta)]; & \lambda_\theta > 0 \end{cases}
\end{aligned}$$

λ_ϑ is the Thwaite's parameter and T_u is the turbulence intensity:

$$\lambda_\vartheta = \frac{\vartheta^2}{\nu} \frac{dU}{ds} , \quad T_u = 100 \sqrt{\frac{2k}{3}} \frac{1}{U}$$

where $\frac{dU}{ds}$ is the acceleration along the streamwise direction.

The correlations for $Re_{\vartheta c}$ and F_{length} are as follows:

$$Re_{\vartheta c} = \min(0.615 \overline{Re_{\vartheta t}} + 61.5, \overline{Re_{\vartheta t}})$$

$$F_{length} = \min[0.5 + \exp(7.168 - 0.01173 \overline{Re_{\vartheta t}}), 300]$$

3.2.4 Radiation model

The considered radiation model allows simulating thermal radiation exchange between diffuse surfaces forming a closed set, considering the medium between them non-participating.

The radiation flux on each surface is a function of the surface radiation properties (emissivity, reflectivity, transmissivity and radiation temperature) and thermal boundary conditions imposed on the surface. In the present work an emissivity of 0.8, a reflectivity of 0.2 (and, consequently, a zero transmissivity) have been assigned to the vehicle surface.

The considered model, based on the theories described in detail in [13,14] operates in the following steps:

- 1) Spatial discretization of the boundary surfaces into patches
- 2) View factors calculation using ray tracing method
- 3) Imposition of the radiation balance on the entire closed set of surfaces and calculation of radiative fluxes on the surfaces.

The amount of radiation exchanged between surfaces depends on the diffuse emission from the surface, the position and orientation of the surfaces relative to each other and the presence of any specularly transmissive or reflective surfaces that may alter the direct transfer between the surfaces. The latter two are taken into account for the calculation of the view factors which represent the fraction of uniform diffuse radiation leaving a surface that directly reaches another surface [13].

For two finite surfaces view factor F_{1-2} is the ratio between the radiation power emitted by S_1 and received by S_2 and the total radiation power emitted from S_1 and can be obtained by integration over constituent elemental surfaces.

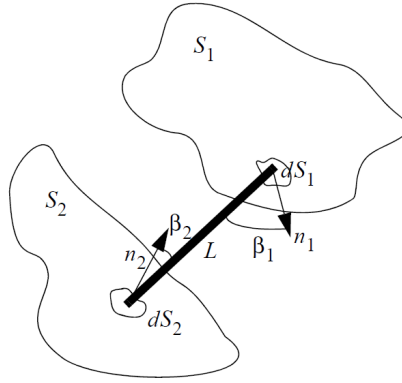


Figure 3.5: Radiation exchange between two finite surfaces

$$F_{1-2} = \frac{1}{S_1} \iint_{S_1 S_2} \frac{\cos \beta_1 \cos \beta_2}{\pi L^2} dS_1 dS_2$$

where β is the angle between the surface normal and a line joining the two surfaces and L is the distance between the two surfaces.

The view factors must satisfy the reciprocity relation:

$$F_{1-2} S_1 = F_{2-1} S_2$$

In the adopted model the boundary surfaces are discretized into small elements called patches and view factors are calculated for each patch pair. An environmental patch is also created by the code in order to collect and account for all the energy radiated to and from the environment around the regions. The emissive power and the radiation properties are assumed to be uniform over the surface of each patch.

The double integral is approximated using a ray tracing approach: for each patch, a predefined number of rays is traced through the computational domain starting at the patch centroid; the directions are based on discretization of an ideal hemisphere over the patch.

After the calculation of the view factors for the patch pairs, radiant fluxes on each patch are obtained by enforcing radiation equilibrium on the entire closed set of surfaces for each radiation spectrum of spectral band. In this work the simplified grey spectrum model has been assumed, for which radiation properties surfaces are considered the same for all wavelengths.

For a generic patch i the radiation contributions are the incident, emitted and transmitted radiations.

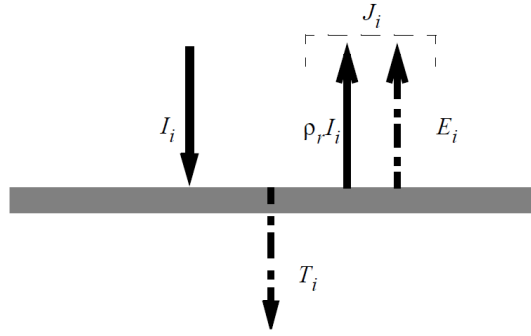


Figure 3.6: Schematic representation of radiation fluxes on patch i

For the radiation balance over the entire closed set of surfaces, all the radiation received by each patch must come from the other patches. Summing over all the N_p patches, the incident radiation flux of the patch i is:

$$Q_{I,i} = S_i I_i = \sum_{j=1}^{N_p} \frac{F_{j-i}}{(1 - \tau_i - \rho_{s,i})} J_{d,j} S_j + \frac{F_{e-i}}{(1 - \tau_i - \rho_{s,i})} J_e S_e$$

where:

- S_i is the surface of the patch i
- I_i is the incident radiation on the patch i
- F_{j-i} is the view factor j to i calculated using ray tracing
- $(1 - \tau_i - \rho_{s,i})$ is the diffuse portion of the surface properties at patch i , where τ_i is the transmissivity and $\rho_{s,i}$ is specular component of reflectivity
- $J_{d,j}$ is the diffuse radiosity of the patch j
- subscript e is used for the environmental patch.

The general reciprocity relationship for view factors between surfaces that may be transmissive and/or specularly reflective is:

$$\frac{F_{j-i} S_j}{(1 - \tau_i - \rho_{s,i})} = \frac{F_{i-j} S_i}{(1 - \tau_j - \rho_{s,j})}$$

Combining the last two equations and introducing the effective radiosity as

$$J_i^{eff} = \frac{J_{d,i}}{(1 - \tau_i - \rho_{s,i})}$$

the incident radiation can be written as:

$$I_i = \sum_{j=1}^{N_p} F_{i-j} J_j^{eff} + F_{i-e} J_e^{eff}$$

The diffuse radiosity of the patch i is the sum of the emitted and the diffusely reflected radiations:

$$J_{d,i} = E_i + \rho_{d,i} I_i$$

Combining the last two equations for each patch a set of radiation balance equations for J_j^{eff} is obtained

$$(1 - \tau_j - \rho_{s,j})J_i^{eff} - \rho_{d,i} \sum_{j=1}^{N_p} F_{i-j} J_i^{eff} = E_i + \rho_{d,i} F_{i-e} J_e^{eff}$$

The surface emissive power is given by the Stefan-Boltzmann law $E_i = \varepsilon_i \sigma T_i^4$, where ε_i is the emissivity, σ is the Stefan-Boltzmann constant and T_i is the surface temperature. Similarly the effective radiosity of the environment, modelled as a black body with unity emissivity, is proportional to the fourth power of the environment temperature $J_e^{eff} = \sigma T_e^4$.

The emissive power, reflectivity, and transmissivity for the patch i are obtained by surface-averaging the face (f) values for the N boundary faces that constitute each patch:

$$E_i = \frac{\sum_{f=1}^{f_N(i)} \varepsilon_{fk} T_{fk}^4 S_{fk}}{\sum_{f=1}^{f_N(i)} S_{fk}}, \quad \rho_i = \frac{\sum_{f=1}^{f_N(i)} \rho_{fk} S_{fk}}{\sum_{f=1}^{f_N(i)} S_{fk}}, \quad \tau_i = \frac{\sum_{f=1}^{f_N(i)} \tau_{fk} S_{fk}}{\sum_{f=1}^{f_N(i)} S_{fk}}$$

At this point the set of radiation balance equations is solved by the software.

The radiative heat flux to the face is given by the difference between the total absorption and the total emission:

$$(q_r)_f = (1 - \tau_f)I_f - J_f$$

where the incident radiation at each face is simply equal to the irradiation on the associated patch i and the face diffuse radiosity is the sum of the emitted and the diffusely reflected radiations:

$$I_f = I_i, \quad J_f = \rho_f I_i + E_f$$

Finally, the effects of radiation are taken into account by augmenting the total boundary heat flux by radiative heat flux.

$$q_f = (q_{no\ rad})_f + (q_r)_f$$

3.2.5 Computational grid

In the present work both structured and unstructured grids have been generated. Two and three dimensional structured grids have been constructed to model simple geometries, such as the fuselage and the wing taken individually and the engine air intake, taking advantage of the commercial CAE pre-processing software ANSA [15].

The three dimensional unstructured grid used to model the entire vehicle have been achieved using the commercial software STAR-CCM+ [16], used also as solver.

In this case meshing guidelines provided by [16] were generally followed, taking into account that the generated grid would have been used for subsonic, trans-supersonic and hypersonic regimes.

The external boundary position has been chosen to avoid problems of interference with the flow field around the vehicle. In particular the overall length of the computational domain was about eight times the length of the body.

A robust prism layer meshing algorithm has been used to capture the boundary layer. The volume mesh has been refined in different areas, by using arbitrarily-shape volumetric control regions. First of all, an overall refinement has been made around the entire vehicle, then a finer one around the wing and the vertical tail. Moreover special refinements have been applied in high spatial gradient zones, such as the nose and the leading edges of lifting surfaces (characterized by small curvature radii) and the body-wing junction, in order to better capture the flow gradients in the solution. Finally the volume mesh has been refined at tips of lifting surfaces and downstream them in order to capture wake vortices. The obtained grid provides proper resolution of geometry and good cell quality.

Key mesh parameters are summarized in Table 3.9. A grid convergence analysis, for the hypersonic cruise condition. is reported in section 4.3.

Mesh parameters	
Number of Cells	6.5 M
Number of Surface Faces	1.3 M
Number of Prism Layers	20

Table 3.9: Computational grid main parameters

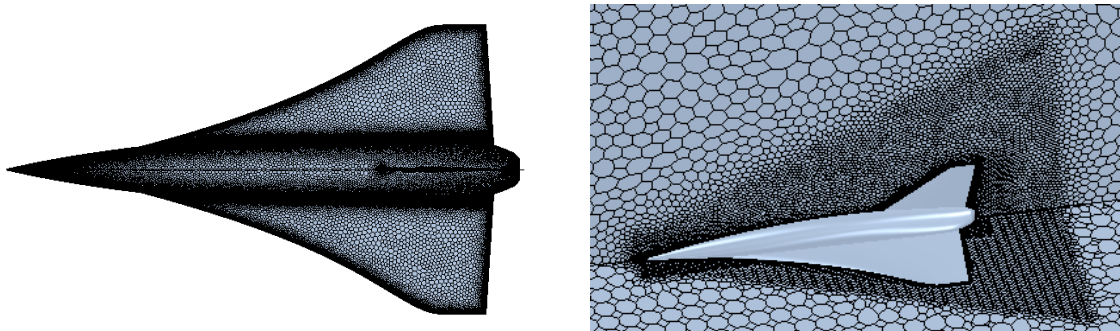


Figure 3.7: Polyhedral grid

Different grids have been generated in order to simulate the effect of the elevons deflections. In these grids further refinements have been defined in the area between the wing trailing edge and the elevons, in order to capture separate flow regions (Figure 3.8).

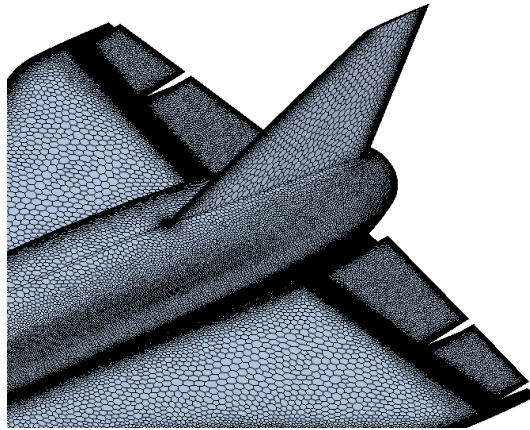


Figure 3.8: Computational grid refinement near the elevons

A different mesh has been generated for the configuration including turboramjet engines. The obtained volume grid consists of 7.2 million cells (Figure 3.9).

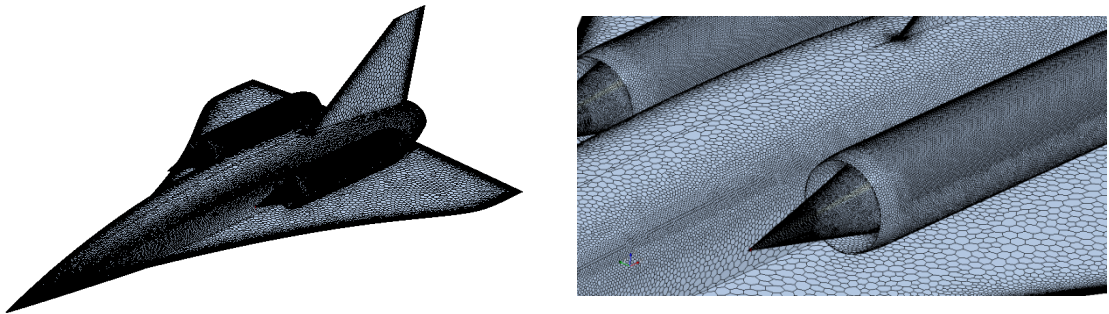


Figure 3.9: Surface grid on the vehicle with engines

Grids have not been customized for any particular attitude. Angles of attack were accomplished by rotating the domain while leaving the grid unaltered.

3.2.6 Solver

The transport equations with suitable boundary conditions have been numerically solved taking advantage of STAR-CCM+, based on the finite-volume method. Discrete versions of the integral form of the transport equations are applied to each cell of the computational grid, in order to obtain a set of linear algebraic equations, which are solved with an algebraic multigrid solver. This approach can be applied both to generated structured and unstructured grids.

Steady state solutions have been evaluated, using a coupled implicit numerical resolutions scheme.

The coupled approach consists in the simultaneous solution of the mass, momentum and energy equations. The non-linear governing equations have been linearized, by

means of an implicit formulation, in order to produce an algebraic system of equations for the dependent variables in every computational cell.

An implicit scheme foresees that, in each cell the unknown quantity of a generic variable is evaluated using a relation which includes both existing and unknown values from neighbouring cells. Unknown therefore appears in more than one equation in the system and these equations are solved simultaneously to achieve the unknown values. Since the governing equations are non-linear and coupled, an iterative process is applied in order to obtain a converged solution. There are two levels of iteration: an outer iteration loop controlling the solution update and an inner loop governing the iterative solution of the linear system. The linear system is solved approximately at each iteration, by means of algebraic multigrid methods.

The different boundary conditions used in this work are:

- Free-stream, to model the flow conditions encountered in the flight envelope pressure outlet, for the downstream surfaces.
- Wall (non-slip) to model the impermeable surface of the vehicle immersed in the viscous flow.
- Axis/symmetry plane, to model 2D axisymmetric and 3D symmetric problems, respectively.

References

- [1] S. R. Vukelich, S. L. Stoy, K. A. Burns, J. A. Castillo, M. E. Moore, Missile DATCOM – VOLUME I – FINAL REPORT, McDonnell Douglas Missile System Company, St. Louis, Missouri 63133 – December 1988 (Final report for period September 1981 – December 1985)
- [2] T. J. Sooy, R. Z. Schmidt, Aerodynamic predictions, comparisons, validations using Missile DATCOM (97) and Aeroprediction 98 (AP98), Journal of Spacecraft and Rockets, vol. 42(2), pp 257-265 (2005)
- [3] E. J. Abney, M. A. McDaniel, High angle of attack aerodynamic predictions using Missile DATCOM, the 23rd AIAA Applied Aerodynamics Conference, Toronto, Ontario, Canada (2005)
- [4] H. Atik, B. Erdem, M. Ilgaz, I. M. Kargancioglu, A. Katirci, E. Mahmutyazicioglu, L. Yalcin, Prediction capabilities and comparison of panel, semi-empiric and CFD codes for missile aerodynamic analysis, the 26th AIAA Applied Aerodynamics Conference, Honolulu, HI, USA (2008)
- [5] W. B. Blake, Missile DATCOM: User's Manual – 1997 FORTRAN 90 Version, Air Force Research Laboratories Document AFRL-VA-WP-TR-1998-3009 (1998)
- [6] D. C Wilcox, Turbulence Modeling for CFD, 2nd edition, DCW Industries, Inc. (1998)
- [7] F. R. Menter, Influence of freestream values on k-w turbulence model predictions, AIAA Journal, Vol. 30, No. 6 (1992)
- [8] F. R. Menter, Two-equation eddy-viscosity turbulence modeling for engineering applications, AIAA Journal 32(8) pp. 1598-1605 (1994)
- [9] F. R. Menter, M. Kuntz, R. Langtry, Ten Years of Industrial Experience with the SST Turbulence Model, Turbulence, Heat and Mass Transfer 4, ed: K. Hanjalic, Y. Nagano, M. Tummers, Begell House, Inc., pp. 625 - 632 (2003)
- [10] R. B. Langtry, A Correlation-Based Transition Model Using Local Variables for Unstructured Parallelized CFD Codes (Doctoral Thesis), University of Stuttgart (2006)
- [11] F. R. Menter, R. B. Langtry, S. R. Likki, Y. B. Suzen, P. G. Huang, S. Volker, A Correlation-Based Transition Model Using Local Variables Part 1 --- Model Formulation, Proc. ASME Turbo Expo, June 14-17, Vienna, Austria (2004)
- [12] K. Suluksna, P. Dechaumphai, E. Juntasaro, Correlations for Modeling Transitional Boundary Layers under Influences of Freestream Turbulence and Pressure Gradient, International Journal of Heat and Fluid Flow (2008)
- [13] R. Siegel, J.R. Howell, Thermal Radiation Heat Transfer, Third Edition, Hemisphere Publishing Co. (1992)
- [14] J. P. Holman, Heat Transfer, Eighth SI Metric Edition, McGraw-Hill (2001)
- [15] ANSA (BETA CAE Systems S.A.) Version 13.0.2 User's Guide
- [16] STAR-CCM+ (CD-adapco) Version 7.06 User's Guide

4 Assessment of aerodynamic prediction capabilities

4.1 Study logic

Missile DATCOM software and CFD simulations have been used to predict HyPlane aerodynamic behaviour. The first one has several limitations: only traditional configurations can be addressed, some analysis assume only axisymmetric configurations, very different models are employed for the analysis of subsonic or super-hypersonic regimes and transonic regimes are often not well modelled.

For this reason, before carrying out an extensive parametric analysis to completely assess the aerodynamic performances of the aircraft at all the relevant operative flight conditions particular efforts have been dedicated to verify the validity of this method for the problem under investigation, also by means of CFD simulations.

In Figure 4.1 a synthetic study logic scheme of this validation procedure and the final goals of this work are presented.

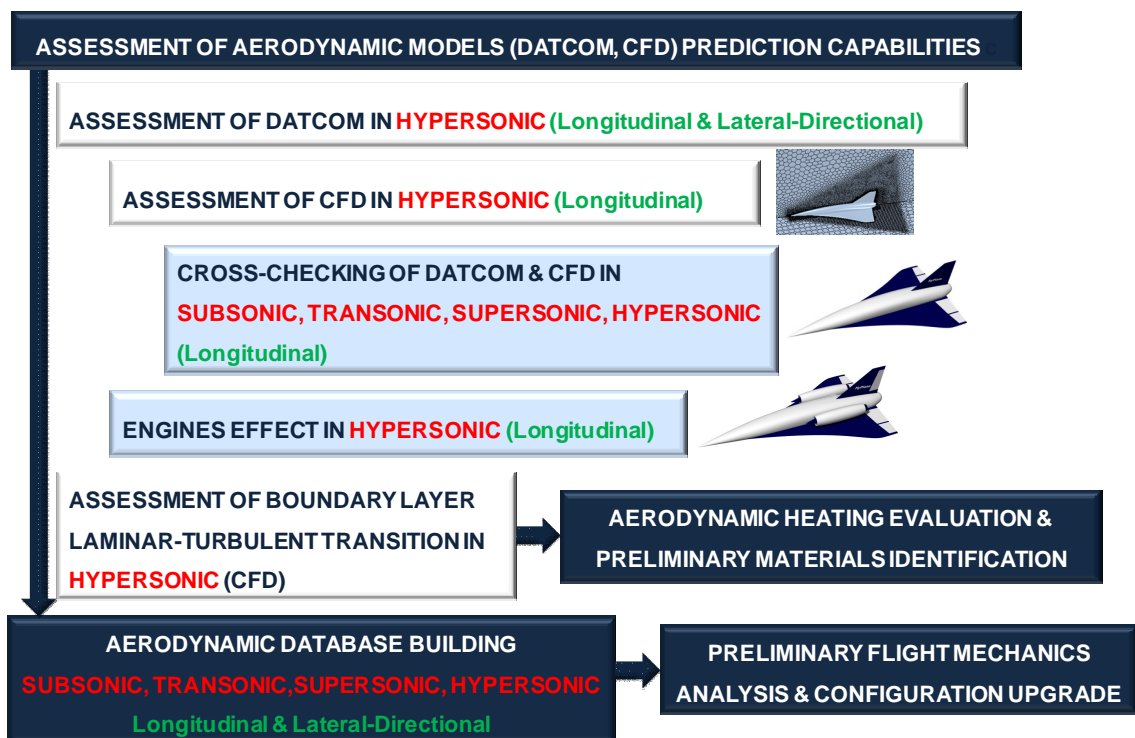


Figure 4.1: Study logic scheme

First of all a preliminary assessment of Missile DATCOM and CFD prediction capabilities in hypersonic regime, since HyPlane primarily operates in this regime.

In particular an assessment of Missile DATCOM has been carried out, by means of a comparison with experimental data for a preliminary configuration of the X-15 (body-wing-tails-elevons) in terms of both longitudinal and lateral-directional aerodynamic characteristics. This analysis is reported in the first section of this chapter.

Then an assessment of the adopted CFD model for the configuration body-wing-tail in hypersonic cruise condition has been achieved, with a grid convergence analysis, presented in the second section.

Subsequently both the aerodynamic prediction methods have been utilized to predict longitudinal aerodynamic coefficients for several flight conditions in subsonic, transonic, supersonic and hypersonic regimes, for the configuration body-wing-tail-elevons. The comparison between the results achieved by the two methods is presented in the third section. One of the most important results of this validation analysis is that the aerodynamic characteristics computed with Missile DATCOM can be properly corrected (particularly in transonic regime) using CFD techniques, to support vehicle design work.

Finally the effects of the TBCC engines on the aerodynamic predictions, for the hypersonic cruise condition, have been studied. This analysis is reported in the fourth section of this chapter.

After the procedure of assessment of prediction capabilities described in this chapter, the validated engineering model has been extensively used for the building of the vehicle complete aerodynamic database, presented in chapter 5.

Further CFD analyzes aimed at investigating the boundary layer laminar-turbulent transition process have also been carried out, in order to investigate its effect on aerodynamic heating occurring in the hypersonic cruise phase and to establish a preliminary materials assessment, presented in chapter 6.

Finally the aerodynamic database has been implemented in a flight simulator, to perform flight mechanics analysis (chapter 7).

4.2 Preliminary assessment of Missile DATCOM prediction capabilities in hypersonic regime

In this section a comparison between Missile DATCOM results and experimental data is presented, for a preliminary configuration of the X-15.

The experimental data are the results of a study on different preliminary configurations of the X-15, carried out in the Langley Research Center in 1969 [1].

The analyzed configuration, illustrated in Figure 4.2, is characterized by a flat-top, negative-camber dihedral delta wing (with incorporated trapezoidal elevons to provide pitch control), an upper and a lower vertical tails. Tip fins are not considered in the Missile DATCOM model, such as in the reported experimental analysis. The experimental tests were conducted in a Mach 6 wind tunnel, at a free-stream Reynolds number of $2.71 \cdot 10^7$ per meter.



Figure 4.2: X-15 preliminary configuration

Figures 4.3 and 4.4 show the comparison between experimental data and Missile DATCOM results, in terms of longitudinal aerodynamic coefficients and lateral-directional static derivatives, respectively.

A satisfactory agreement has been found with longitudinal experimental data. In particular lift coefficient prediction has a minimal error, drag coefficient is slightly overestimated for low angles of attack and underestimated for higher angles of attack; the pitching moment prediction presents a more consistent error. Some discrepancies have also been found for lateral-directional static derivatives.

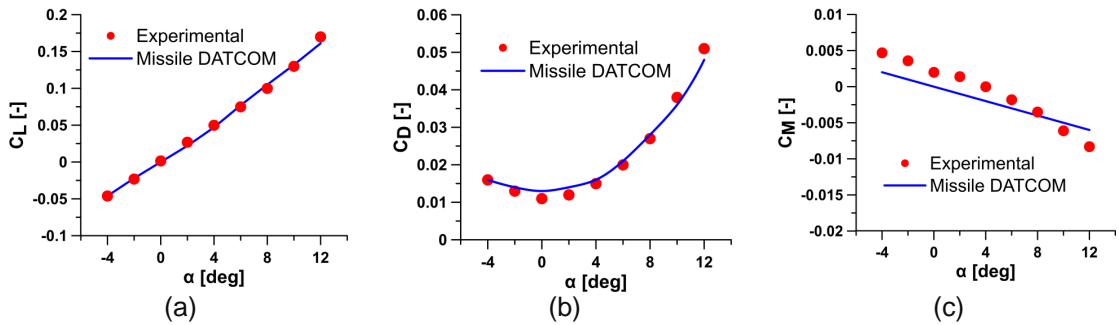


Figure 4.3: Lift (a), drag (b) and pitching moment (c) coefficients as a function of angle of attack at $M_\infty = 6$, $Re_\infty = 2.71 \cdot 10^7$. Comparison between experimental data and Missile DATCOM results

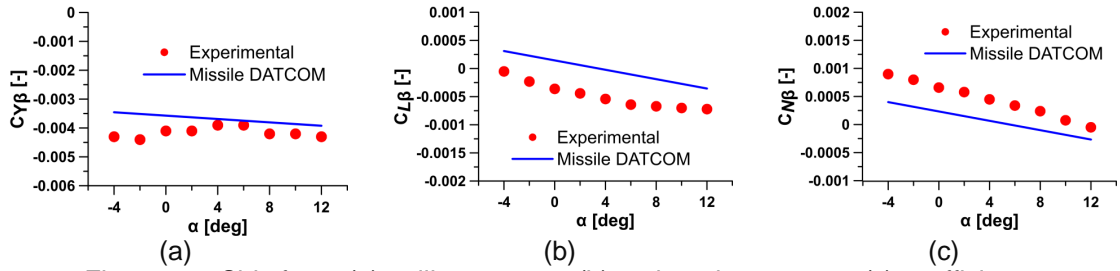


Figure 4.4: Side force (a), rolling moment (b) and yawing moment (c) coefficients as a function of angle of attack at $M_\infty = 6$, $Re_\infty = 2.71 \cdot 10^7$. Comparison between experimental data and Missile DATCOM results

The effect of the elevons deflection has also been investigated. Figure 4.5 shows a comparison between experimental and numerical results in terms of c_L and c_D , for a 10° elevons deflection. A satisfactory agreement has been found for the lift coefficient, while an underestimation of the drag coefficient for high angles of attack has emerged.

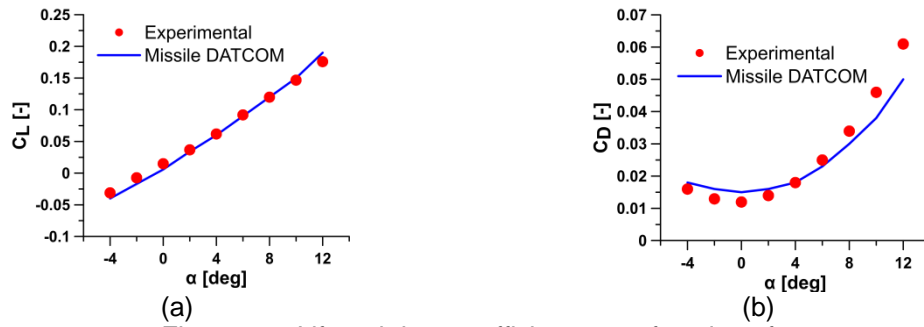


Figure 4.5: Lift and drag coefficients as a function of angle of attack, with $\delta_e = 10^\circ$, at $M_\infty = 6$, $Re_\infty = 2.71 \cdot 10^7$. Comparison between experimental data and Missile DATCOM results

4.3 Preliminary assessment of CFD model in hypersonic regime

Three unstructured meshes have been generated using STAR-CCM+ to perform a grid sensitivity analysis in hypersonic conditions, in order to ensure the independence of computed results from the mesh size. For this analysis the HyPlane body-wing-tail configuration has been considered.

A "medium" polyhedral grid with 20 prism layers on the body surface has been generated. This mesh has been properly refined in critical areas such as the nose and the leading edges of lifting surfaces and to the body-wing junction, in order to better capture the flow gradients in the solution. Further refinements have been applied at tips of lifting surfaces and downstream them in order to capture wake vortices, for total of 6.5 M cells.

A "coarse" grid has been generated by increasing the global cell size of the mesh by 60%, reducing the number of prism layers and removing some refinements, while a "fine" grid has been obtained by reducing the size of 40% and increasing the number of prism layers. Key mesh parameters are summarized in Table 4.1. The obtained grids provide proper resolution of geometry and good cell quality.

Parameters	Coarse	Medium	Fine
Number of Cells	4.6 M	6.5 M	13.5 M
Number of Surface Faces	1.1 M	1.3 M	1.5 M
Number of Prism Layers	15	20	25

Table 4.1: Coarse, medium and fine grids main parameters

Figure 4.6 shows the grid density on the vehicle and the symmetry plane, respectively, for the coarse, the medium and the fine meshes.

The assumed flow conditions for the simulations are shown in Table 4.2.

Results of the simulations in terms of longitudinal aerodynamic coefficients are presented in Table 4.3. Longitudinal forces and moment are nondimensionalized by the freestream dynamic pressure and the reference area, which is the wing area. In addition, pitching moment is nondimensionalized by the reference length, which is the wing mean aerodynamic chord. Pitching moment is evaluated with respect to a pole at 15 m distance from the apex of the vehicle nose.

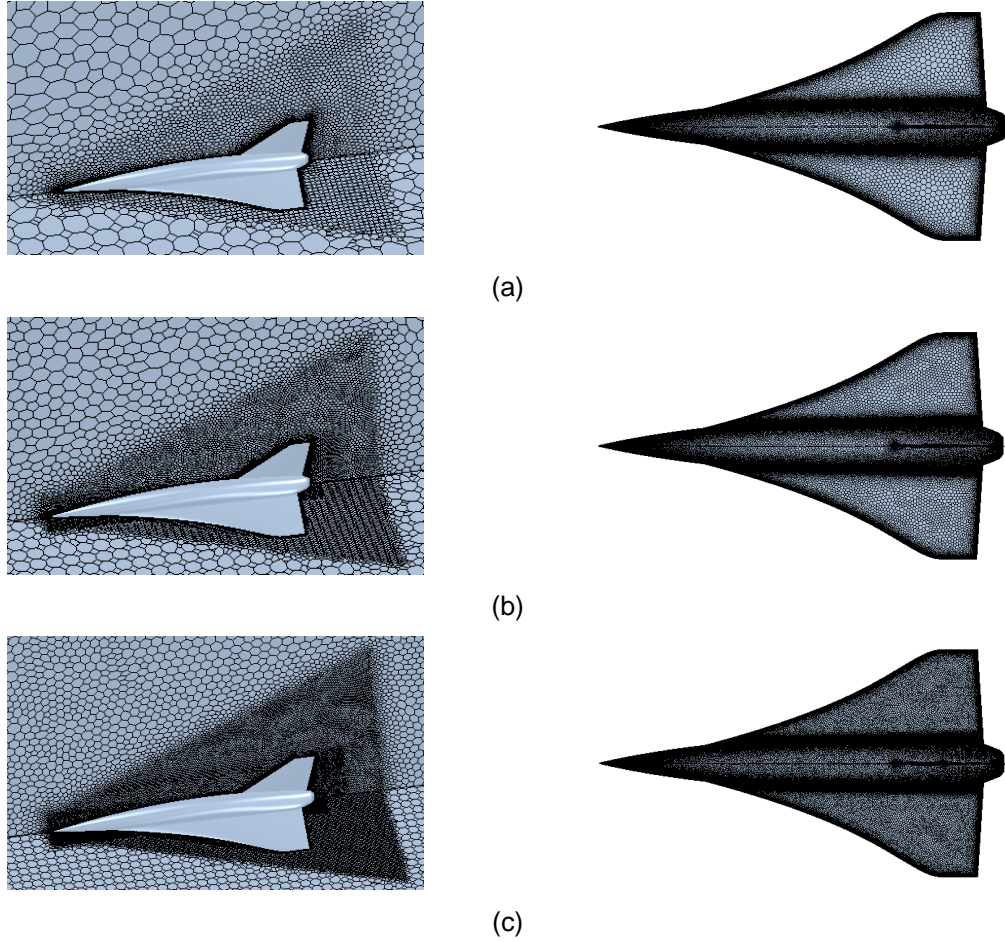


Figure 4.6: Coarse (a), medium (b) and fine (c) grids

Case	M_∞	$H[km]$	$\alpha [deg]$
1	4	30	0
2	4	30	4

Table 4.2: Flow conditions for the grid sensitivity analysis

Case	Grid	C_L	C_D	C_M
1	Coarse	-0.00670	0.00880	-0.00560
	Medium	-0.00702	0.00902	-0.00549
	Fine	-0.00701	0.00909	-0.00547
2	Coarse	0.0570	0.0124	-0.0102
	Medium	0.0569	0.0127	-0.0100
	Fine	0.0570	0.0128	-0.0100

Table 4.3: Longitudinal aerodynamic coefficients computed by CFD simulations adopting different grids

Since deviations in results with the fine grid are lower than 2%, the medium grid has been chosen to perform the CFD analysis. This grid has been used not only for calculations in hypersonic regime, but also in subsonic and trans-supersonic regimes.

4.4 Utilization of Missile DATCOM and CFD model for different flight conditions

Preliminary computations have been performed to cross-check the longitudinal aerodynamic coefficients obtained by means of Missile DATCOM software and CFD simulations, for the HyPlane body-wing-tail-configuration, for several flight conditions, in subsonic, transonic, supersonic and hypersonic regimes (Figure 4.7). The effect of the elevons deflection has also been investigated, for some flight conditions.

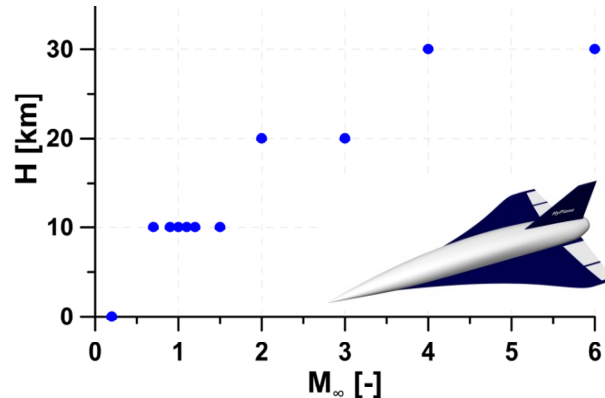


Figure 4.7: Flight conditions investigated with Missile DATCOM and CFD simulations

For CFD simulations the boundary layer has been assumed fully turbulent, in order to be conservative in the estimation of the skin friction drag. Pitching moment is evaluated with respect to a pole at 15 m distance from the apex of the vehicle nose.

4.4.1 Body-wing-tail configuration

The analysis is performed for Mach numbers from 0.2 to 6, altitudes up to 30 km and angles of attack from 0° to 20°, as shown in Table 4.4.

Regimes	M_∞	$H[km]$	$\alpha [deg]$
Subsonic	0.2	0	0,4,8,12,16,20
	0.7	10	0,4,8,12,16,20
Transonic	0.9	10	0,4,8,12,16,20
	1.0	10	0,4,8,12,16,20
	1.1	10	0,4,8,12,16,20
	1.2	10	0,4,8,12,16,20
	1.5	15	0,4,8,12,16,20
Supersonic	2.0	20	0,4,8,12,16,20
	3.0	20	0,4,8,12,16,20
	4.0	30	0,4,8,12,16,20
Hypersonic	6.0	30	0,4,8,12,16,20

Table 4.4: Flight conditions investigated with Missile DATCOM and CFD simulations

Subsonic regime

The longitudinal characteristics computed with the two different tools, for the analyzed subsonic flight conditions, are reported in Figures 4.8 and 4.9.

A very good agreement has been found for the prediction of c_L and c_D , while discrepancies in the computation of c_M have emerged, for angles of attack of 4° , 8° and 12° .

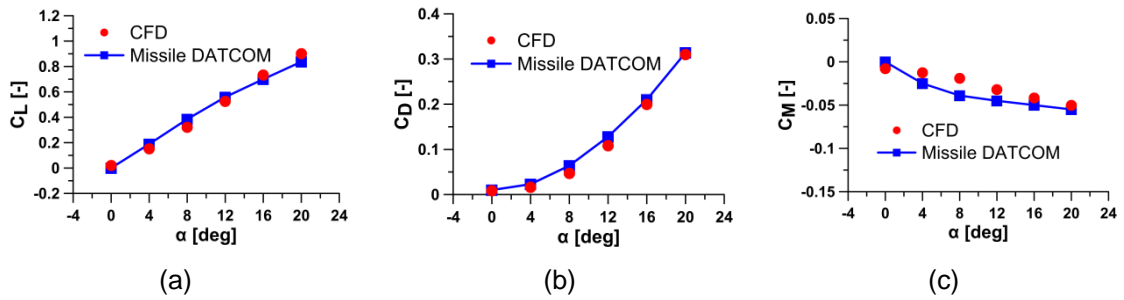


Figure 4.8: Predicted lift (a), drag (b) and pitching moment (c) coefficients as a function of angle of attack, for $M_\infty = 0.2$, $H = 0$ km. Comparison between Missile DATCOM and CFD results

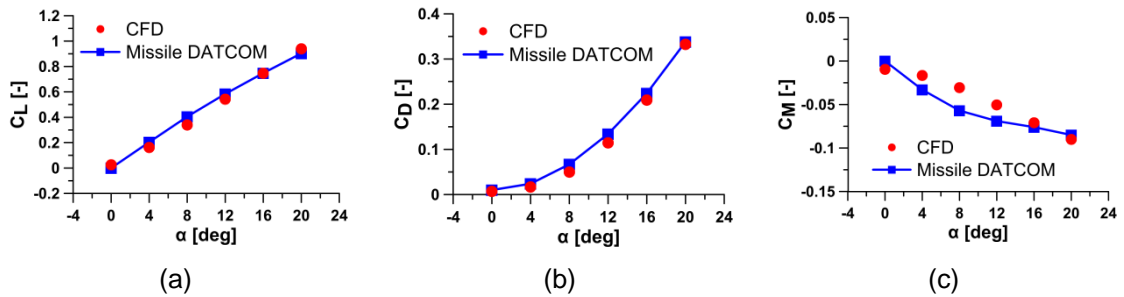


Figure 4.9: Predicted lift (a), drag (b) and pitching moment (c) coefficients as a function of angle of attack, for $M_\infty = 0.7$, $H = 10$ km. Comparison between Missile DATCOM and CFD results

The pressure distributions on the vehicle and on the symmetry plane corresponding to the solutions computed with CFD simulations at $M_\infty=0.2$ and $H=0$ km, at different angles of attack are presented in Figure 4.10.

In Figure 4.11 it is possible to observe the vortical structures forming over the delta wing in high-subsonic regime ($M_\infty=0.7$, $H=10$ km), as the angle of attack increases. The vorticity contours and surface streamlines on different sections along the vehicle length (10 m, 14 m, 18 m and 22 m etc distance from the nose apex) computed at $\alpha=8^\circ$ are presented in Figure 4.12.

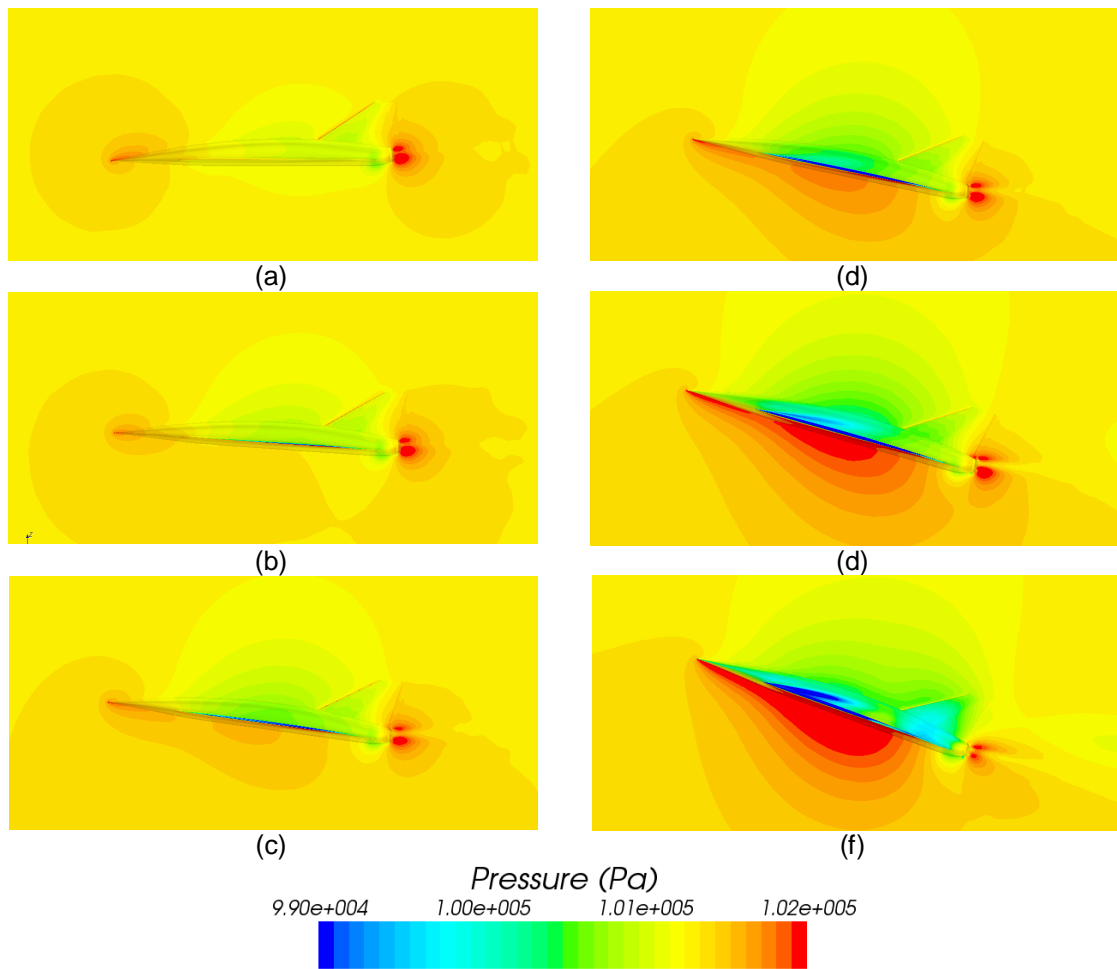


Figure 4.10: Pressure contour on the vehicle and the symmetry plane computed with CFD simulations. $M_\infty = 0.2$, $H = 0$ km. $\alpha = 0^\circ$ (a), $\alpha = 4^\circ$ (b), $\alpha = 8^\circ$ (c), $\alpha = 12^\circ$ (d), $\alpha = 16^\circ$ (e), $\alpha = 20^\circ$ (f)

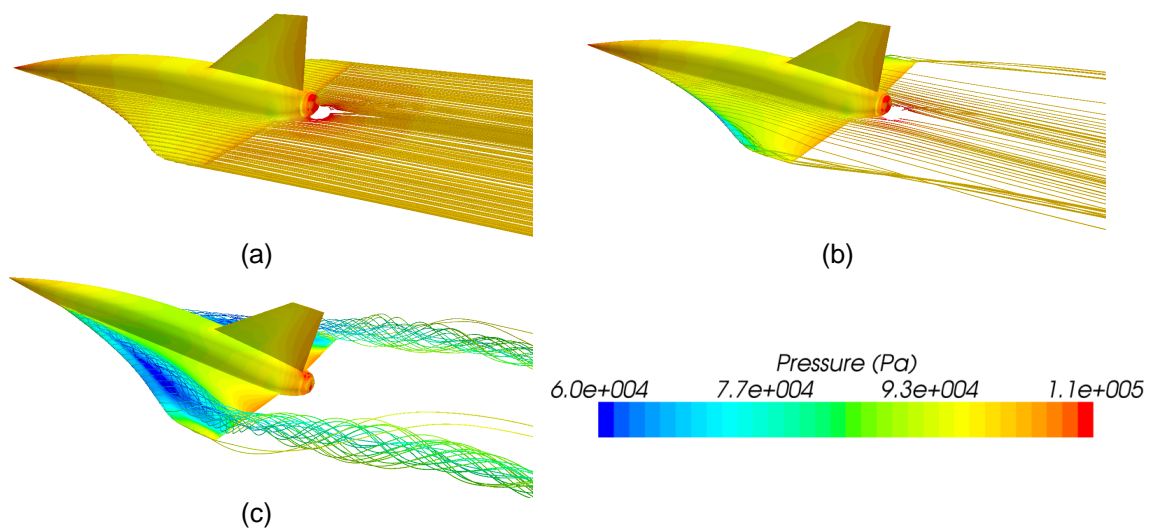


Figure 4.11: Pressure contour on the vehicle and streamlines computed with CFD simulations. $M_\infty = 0.7$, $H = 10$ km. $\alpha = 0^\circ$ (a), $\alpha = 4^\circ$ (b), $\alpha = 8^\circ$ (c)

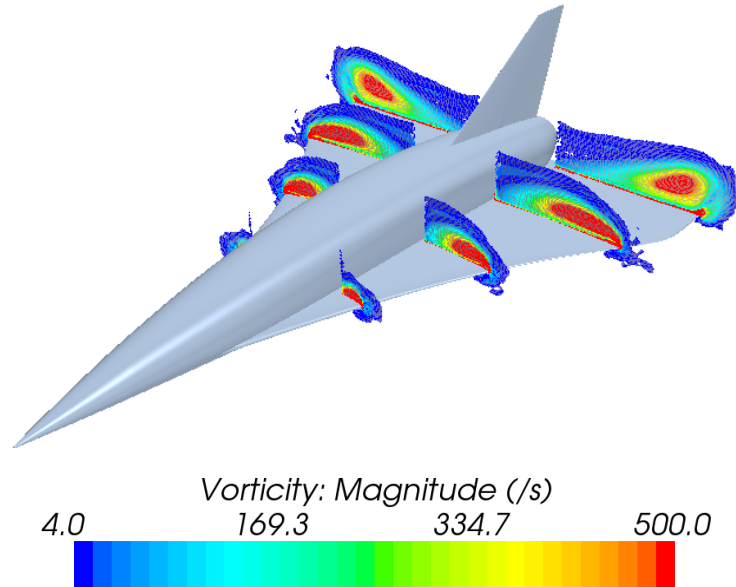


Figure 4.12: Vorticity contours and surface streamlines computed with CFD simulations.
 $M_\infty = 0.7$, $H = 10 \text{ km}$, $\alpha = 8^\circ$

Transonic regime

Figures 4.12-15 show lift, drag and pitching moment coefficients computed with the two different aerodynamic prediction methods, for the selected transonic flight conditions. In transonic regime Missile DATCOM overpredicts lift and drag coefficients and underpredicts pitching moment coefficient, if compared to CFD. Discrepancies are very pronounced, especially for $M_\infty=1$.

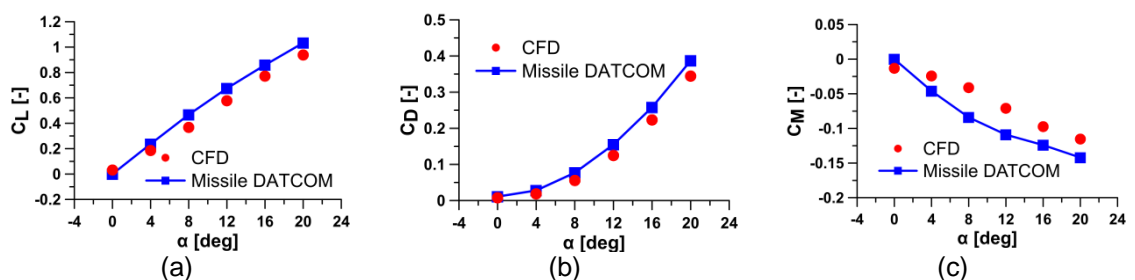


Figure 4.12: Predicted lift (a), drag (b) and pitching moment (c) coefficients as a function of angle of attack, for $M_\infty = 0.9$, $H = 10 \text{ km}$. Comparison between Missile DATCOM and CFD results

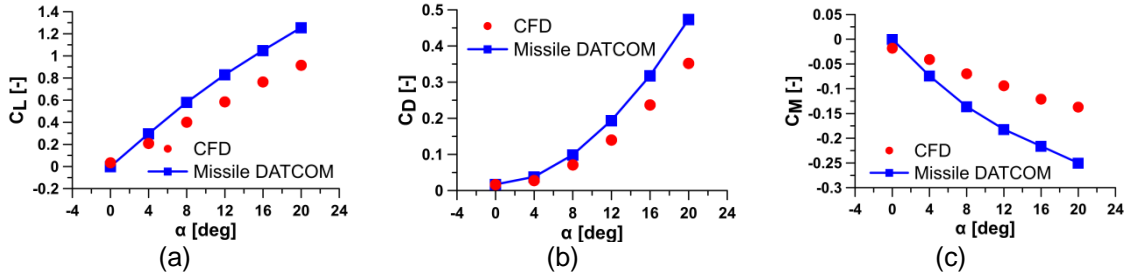


Figure 4.13: Predicted lift (a), drag (b) and pitching moment (c) coefficients as a function of angle of attack, for $M_\infty = 1.0$, $H = 10$ km. Comparison between Missile DATCOM and CFD results

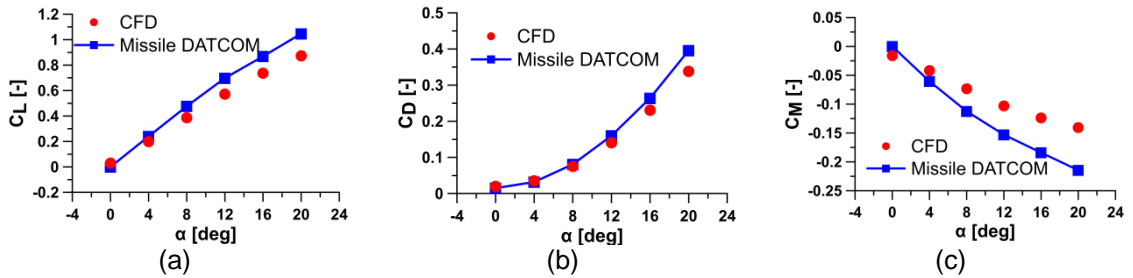


Figure 4.14: Predicted lift (a), drag (b) and pitching moment (c) coefficients as a function of angle of attack, for $M_\infty = 1.1$, $H = 10$ km. Comparison between Missile DATCOM and CFD results

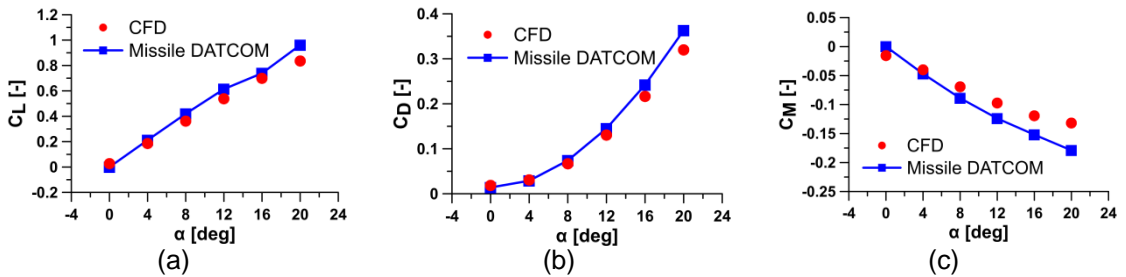


Figure 4.15: Predicted lift (a), drag (b) and pitching moment (c) coefficients as a function of angle of attack, for $M_\infty = 1.2$, $H = 10$ km. Comparison between Missile DATCOM and CFD results

Supersonic regime

The longitudinal characteristics computed with two different methods, for the analyzed supersonic flight conditions, are reported in Figures 4.16-18.

It is possible to observe that the discrepancy registered in transonic regime reduces as the Mach number increases. In fact, for $M_\infty=3$, the semi-empirical prediction code produces results very close to the CFD ones, for all the coefficients.

In this regime Missile DATCOM tends to overestimate lift and drag coefficients for high angles of attack, with respect to CFD results.

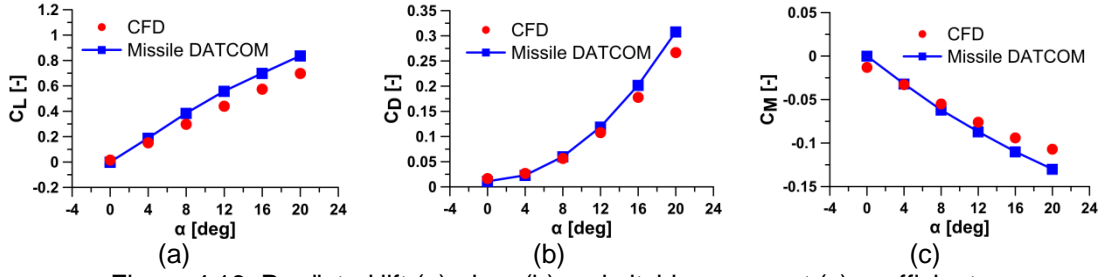


Figure 4.16: Predicted lift (a), drag (b) and pitching moment (c) coefficients as a function of angle of attack, for $M_\infty = 1.5$, $H = 15$ km. Comparison between Missile DATCOM and CFD results

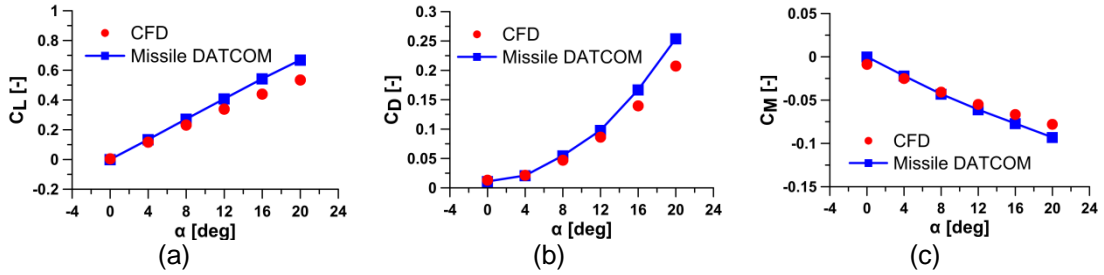


Figure 4.17: Predicted lift (a), drag (b) and pitching moment (c) coefficients as a function of angle of attack, for $M_\infty = 2.0$, $H = 20$ km. Comparison between Missile DATCOM and CFD results

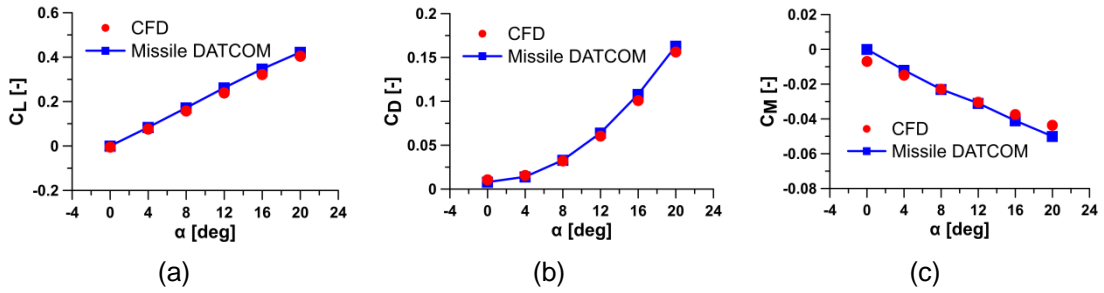


Figure 4.18: Predicted lift (a), drag (b) and pitching moment (c) coefficients as a function of angle of attack, for $M_\infty = 3.0$, $H = 30$ km. Comparison between Missile DATCOM and CFD results

The Mach number contour and the pressure distribution on the vehicle corresponding to the solutions computed with CFD at $M_\infty=2.0$ and $H=20$ km, at different angles of attack, are presented in Figure 4.19.

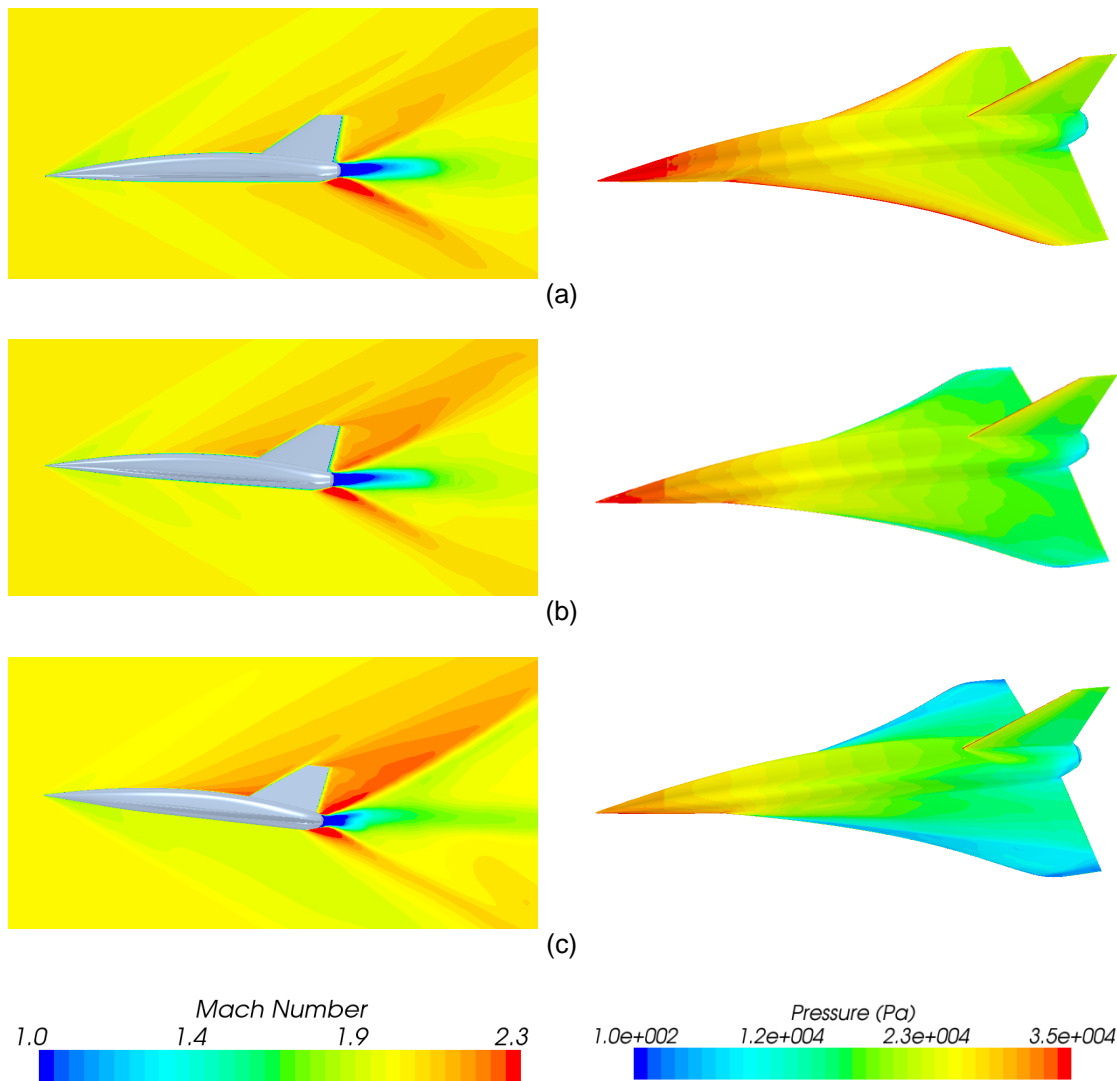


Figure 4.19: Mach number and pressure contours on the vehicle and the symmetry plane computed with CFD simulations. $M_\infty = 2.0$, $H = 20 \text{ km}$.
 $\alpha = 0^\circ$ (a), $\alpha = 4^\circ$ (b), $\alpha = 8^\circ$ (c)

Hypersonic regime

In Figures 4.20 and 4.21 longitudinal aerodynamic coefficients evaluated with the adopted techniques are presented, for two different hypersonic conditions, corresponding to $M_\infty=4$ and $M_\infty=6$ respectively, at $H=20$ km.

Results provided by the two different methods are very close, for all the coefficients. Also in this regime Missile DATCOM tends to overestimates lift and drag coefficients for high angles of attack, with respect to CFD results.

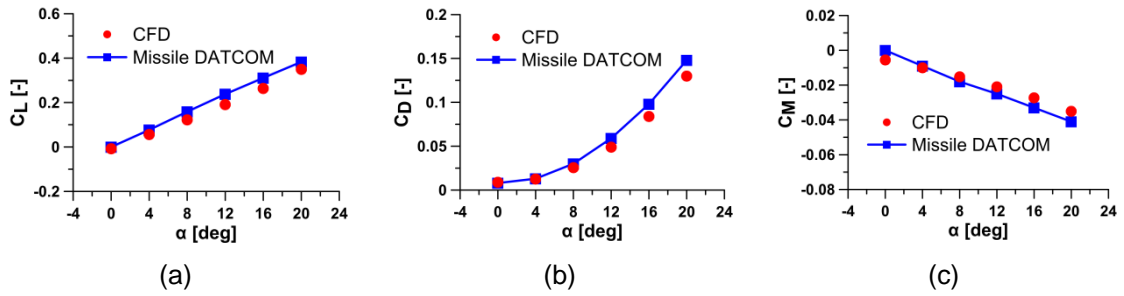


Figure 4.20: Predicted lift (a), drag (b) and pitching moment (c) coefficients as a function of angle of attack, for $M_\infty = 4.0$, $H = 30$ km. Comparison between Missile DATCOM and CFD results

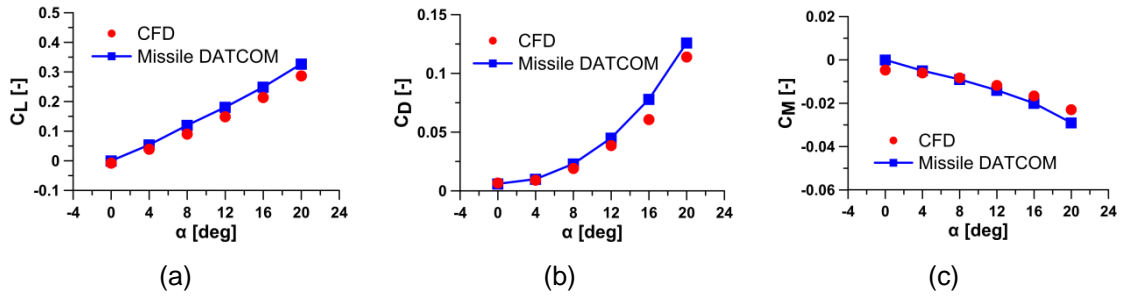


Figure 4.21: Predicted lift (a), drag (b) and pitching moment (c) coefficients as a function of angle of attack, for $M_\infty = 6.0$, $H = 30$ km. Comparison between Missile DATCOM and CFD results

In Figure 4.22 it is possible to observe the evolution of the conical shock wave that originates from the vehicle nose varying the angle of attack, for $M_\infty=4$ and $H=30$ km.

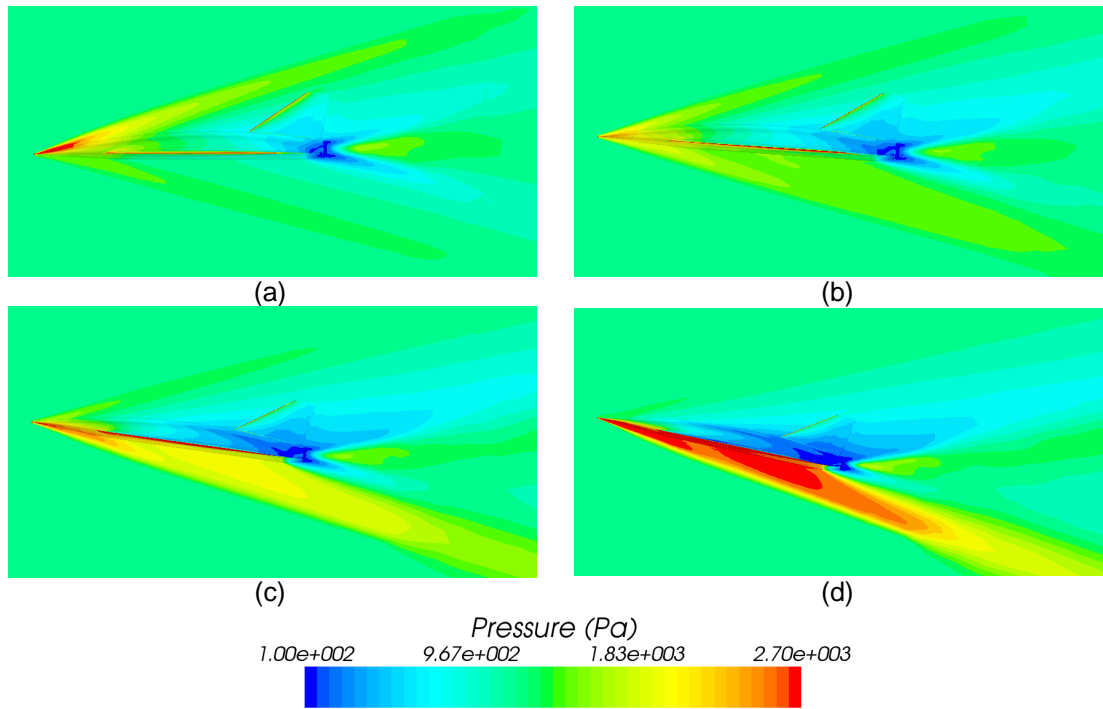


Figure 4.22: Pressure contour on the vehicle and the symmetry plane computed with CFD simulations. $M_\infty = 2.0$, $H = 20$ km.
 $\alpha = 0^\circ$ (a), $\alpha = 4^\circ$ (b), $\alpha = 8^\circ$ (c), $\alpha = 12^\circ$ (d)

Summary for all flight regimes

Figure 4.23 shows lift, drag and pitching moment coefficients as a function of Mach number, for different angles of attack, computed by the two methods. Solid lines refer to Missile DATCOM results while dots are CFD values.

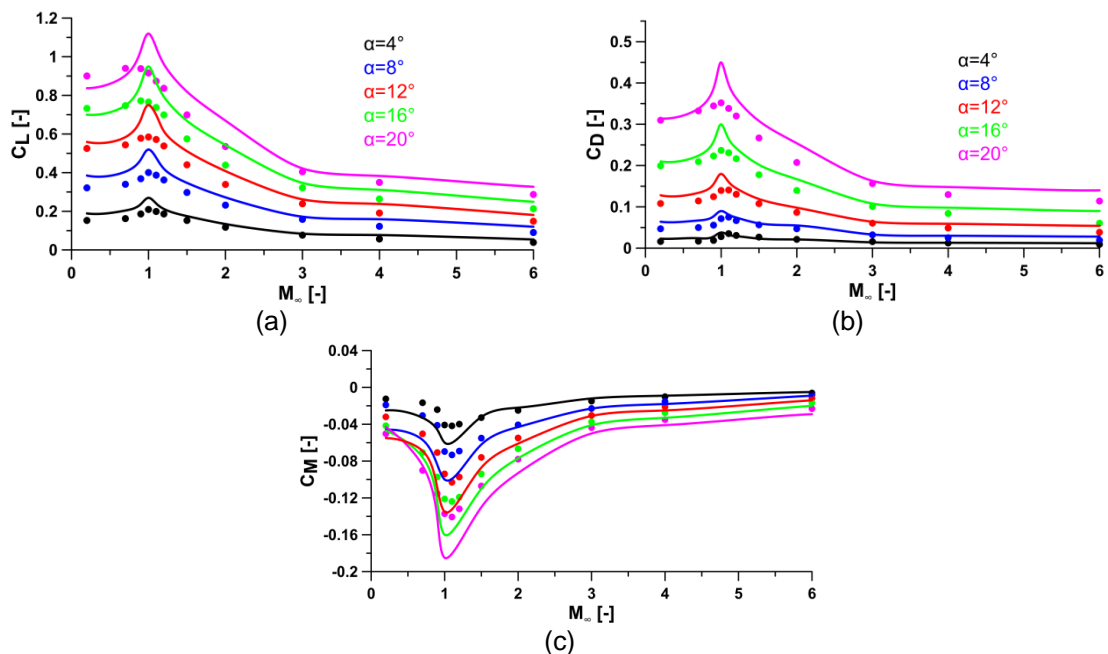


Figure 4.23: Lift (a), drag (b), pitching moment (c) coefficients as a function of Mach number for different angles of attack, computed by Missile DATCOM (solid lines) and CFD simulations (dots)

The averaged deviation of Missile DATCOM computations, with respect to CFD results is presented in the Table 4.5, for the lift, drag and pitching moment coefficients, varying the flight regime. CFD values have been chosen to nondimensionalise the absolute deviation.

An important result of this analysis is that the aerodynamic characteristics computed with Missile DATCOM can be properly corrected (particularly in transonic regime) using CFD techniques, to support vehicle design work. For the other flight regimes, obtained correlation is generally satisfactory.

CFD analysis confirms that Missile DATCOM is particularly suitable during conceptual and preliminary design phases.

Regimes	Lift Deviation	Drag Deviation	Pitching Moment Deviation	Averaged Deviation
Subsonic	4.6%	15.1%	29.2%	19.0%
Transonic	20.3%	18.2%	39.0%	25.7%
Supersonic	14.4%	6.8%	12.0%	11.1%
Hypersonic	8.3%	12.1%	8.5%	9.6%

Table 4.5: Deviation of Missile DATCOM computations, with respect to CFD results, for lift drag and pitching moment coefficients, varying the flight regime

4.4.2 Body-wing-tail-elevons configuration

Analysis of the effect of pitch control surfaces has been conducted for some flight conditions and different elevons deflections, shown in Table 4.6.

The elevons deflection is assumed positive when both the elevons are deflected downward. With this convention a positive elevons deflection produces a negative pitching moment.

M_∞	$H[km]$	$\alpha [deg]$	$\delta_e [deg]$
0.7	10	0	0,10,20
2.0	20	0	0,10,20
4.0	30	0	0,-10,-20

Table 4.6: Flight conditions investigated with Missile DATCOM and CFD simulations

In figures 4.24-26 contributes to lift, drag and pitching moment coefficients predicted by the two different tools are presented, as a function of elevons deflections.

A reasonable agreement between results has been found. In particular the two methods predict very close contribute to c_D , while the contributes to c_L and c_M

computed by Missile DATCOM are slightly lower in subsonic and higher in supersonic regime, if compared to CFD results.

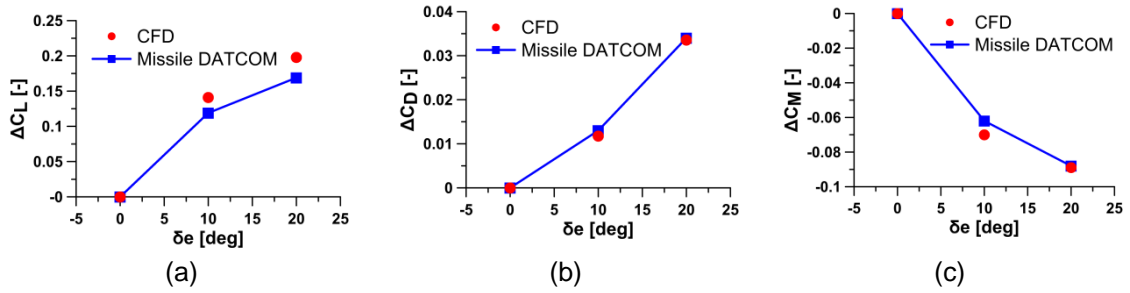


Figure 4.24: Predicted contributes to lift (a), drag (b) and pitching moment (c) coefficients as a function of elevons deflection, for $M_\infty = 0.7$, $H = 10 \text{ km}$, $\alpha = 0^\circ$. Comparison between Missile DATCOM and CFD results

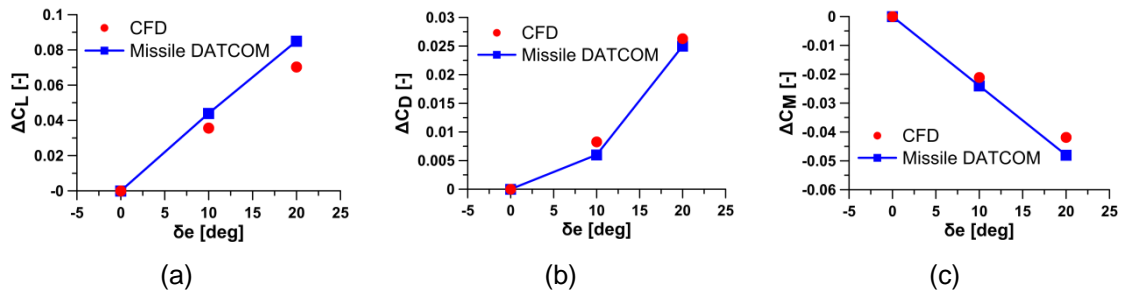


Figure 4.25: Predicted contributes to lift (a), drag (b) and pitching moment (c) coefficients as a function of elevons deflection, for $M_\infty = 2.0$, $H = 20 \text{ km}$, $\alpha = 0^\circ$. Comparison between Missile DATCOM and CFD results

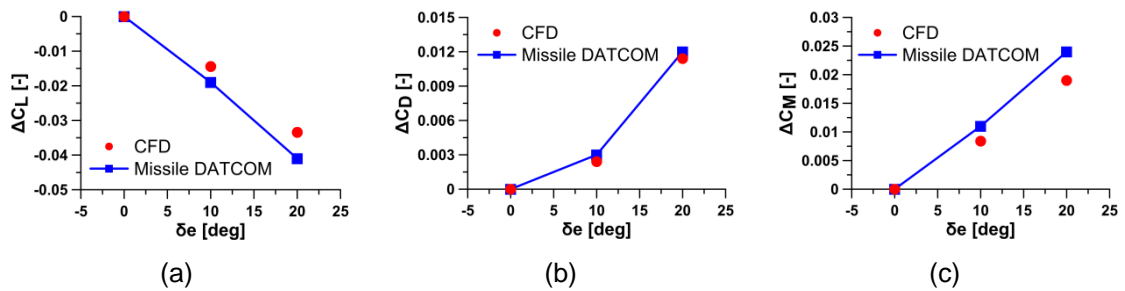


Figure 4.26: Predicted contributes to lift (a), drag (b) and pitching moment (c) coefficients as a function of elevons deflection, for $M_\infty = 4.0$, $H = 30 \text{ km}$, $\alpha = 0^\circ$. Comparison between Missile DATCOM and CFD results

Figures 4.27-29 illustrate the pressure distribution on the vehicle for the analyzed flight conditions.

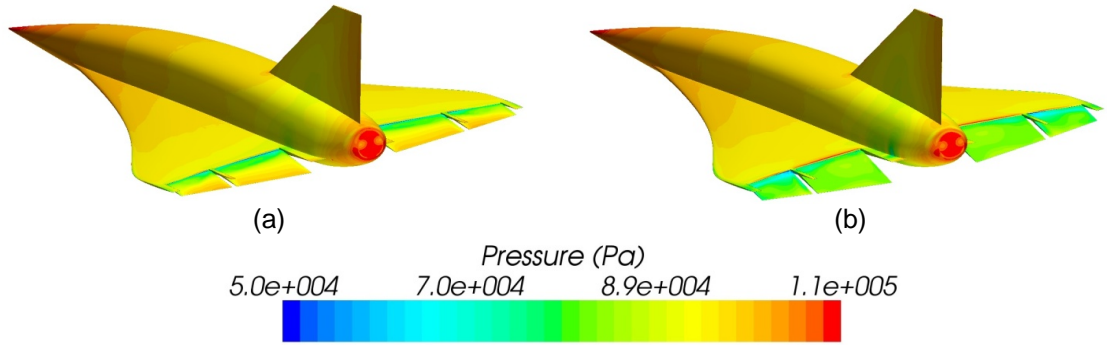


Figure 4.27: Pressure contour on the vehicle computed with CFD simulations ($M_\infty = 0.7$, $H = 10 \text{ km}$, $\alpha = 0^\circ$). $\delta_e = 10^\circ$ (a), $\delta_e = 20^\circ$ (b)

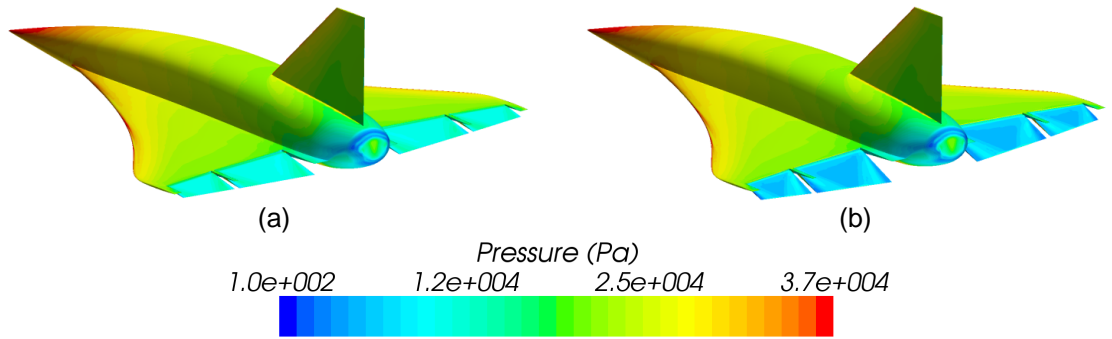


Figure 4.28: Pressure contour on the vehicle computed with CFD simulations ($M_\infty = 2.0$, $H = 20 \text{ km}$, $\alpha = 0^\circ$). $\delta_e = 10^\circ$ (a), $\delta_e = 20^\circ$ (b)

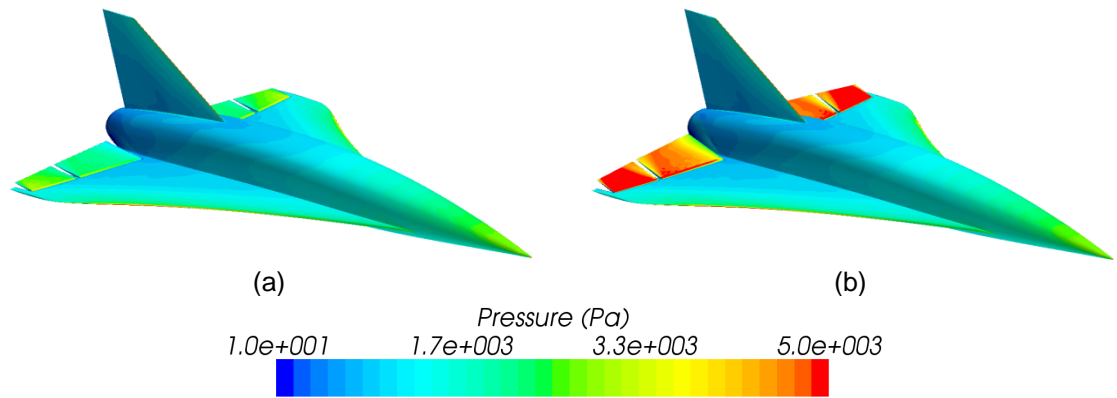


Figure 4.29: Pressure contour on the vehicle computed with CFD simulations ($M_\infty = 4.0$, $H = 30 \text{ km}$, $\alpha = 0^\circ$). $\delta_e = -10^\circ$ (a), $\delta_e = -20^\circ$ (b)

4.5 Effects of engines on aerodynamic predictions in hypersonic regime

For a correct estimate of the aerodynamic database it is necessary to take into account the presence of the TBCC engines.

Therefore the air-intake and the engine external configuration have been preliminarily designed, in order to assess the effect on the aerodynamic performances.

In this section the designed variable geometry air intake is presented and its functioning is briefly shown. Then the CFD analysis aimed at achieving the inlet main performances are presented. In particular two operating conditions have been investigated: the nominal hypersonic cruise condition and a supersonic condition, corresponding to different spike configurations. Finally the effect of the presence of the engines on the HyPlane global lift and drag coefficients, in hypersonic cruise conditions, evaluated by CFD simulations and Missile DATCOM, is presented.

4.5.1 Mixed compression variable geometry inlet

The extent of the HyPlane operating speed and altitude ranges necessitates a variable-geometry inlet, able to supply to the engine a flow at correct pressure and velocity throughout the flight envelope. In particular an axisymmetric mixed internal/external compression supersonic inlet, using a translating spike has been considered.

The considered air intake has been designed to produce, at nominal conditions (at cruising speed and altitude), a cone-shaped shock impinging at the cowl lip (external compression) and getting reflected along the duct enclosed by the spike and cowl internal surface, leading to a further internal compression which terminates with a normal shock in the throat (at Mach number near one), ensuring subsonic conditions at the entrance of the combustion chamber and producing a relatively high total pressure recovery.

In operation, the spike translates as a function of altitude and Mach number, varying the position of the cone shaped shock wave and the size of the inlet throat area, in order to capture and maintain the normal shock wave in the optimal position.

In Figure 4.30 the geometry of the designed inlet and the schematic of flow at the nominal cruise condition are illustrated.

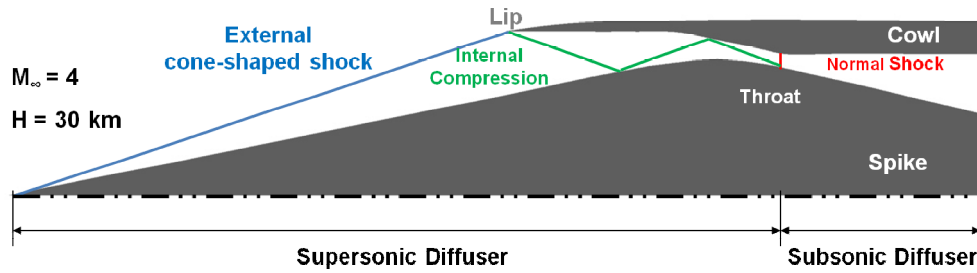


Figure 4.30: Schematic of flow field for the HyPlane turbo-ramjet inlet at the nominal condition

4.5.2 CFD analysis and inlet performances

Two different spike configurations have been modelled (Figure 4.31). The first, corresponding to the nominal condition ($M_\infty=4$, $H=30$ km) is characterized by a throat area of 0.17 m^2 . The second configuration is obtained by translating the spike of 0.66 m forward and provides a throat area of 0.4 m^2 ; the corresponding flight condition is $M_\infty=2$, $H=15$ km, as summarized in Table 4.7.

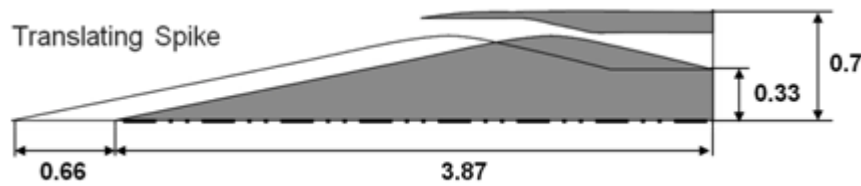


Figure 4.31: Turbo-ramjet variable geometry inlet. Dimensions expressed in meters

	$A_t [\text{m}^2]$	M_∞	$H [\text{km}]$
Nominal (Cruise)	0.17	4.0	30
Supersonic	0.4	2.0	15

Table 4.7: Analysed turbo-ramjet inlet operating conditions

A two-dimensional structured grid of about 0.12 million quadrilateral cells has been generated with the pre-processor ANSA. Steady state, axisymmetric RANS equations, closed by the $k - \omega$ turbulence model, have been solved, using a coupled implicit numerical resolutions scheme. The effect of the presence of the combustion chamber is taken into account by imposing a high back pressure at the exit of the engine inlet.

The results of the numerical simulations are presented in terms of contours of the main fluid dynamic quantities. In particular the distributions of Mach number, pressure, temperature, total pressure and streamlines for the nominal (cruise) condition and the

considered supersonic condition, at zero angle of attack, are presented in Figures 4.32 and 4.33, respectively.

An oblique shock wave attached to spike's tip, that externally compresses the flow, is originated. At the nominal condition ($M_\infty=4$, $H=30$ km) the shock-on-lip condition is satisfied while for the supersonic condition ($M_\infty=2$, $H=15$ km) the shock angle is larger, causing an external bleeding of flow. The throat area increase, resulted from the spike forward translation, allows catching and retaining the normal shock wave in the throat. In fact in both examined cases, it is possible to see a series of reflected compression shock waves, along the duct enclosed by the spike and the cowl internal surface, through which the flow is decelerated, approaching Mach number near to one in the throat section, where a normal shock wave occurs. This functioning guarantees a good total pressure recovery, ensuring a relatively high air intake efficiency, defined as:

$$\eta = p_{02}/p_{01}$$

where p_{01} and p_{02} are the total pressure values upstream and downstream the inlet, respectively.

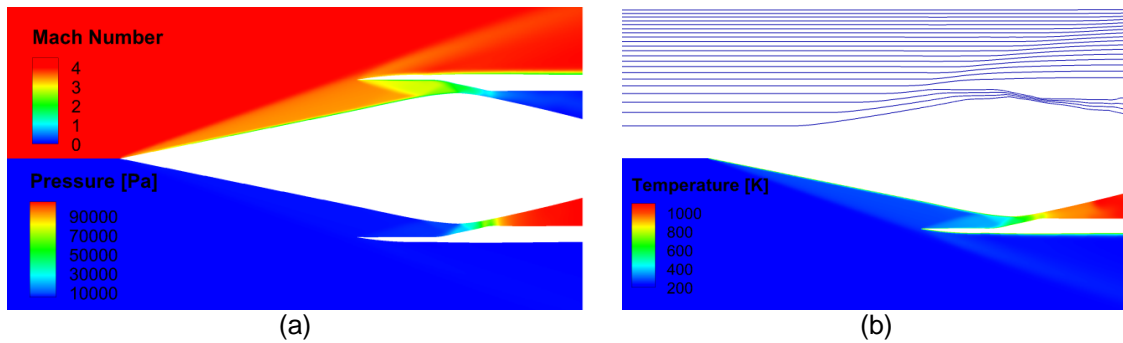


Figure 4.32: Mach number, pressure (a), streamlines and temperature (b) distributions at $M_\infty = 4$, $H = 30$ km and $\alpha = 0^\circ$, computed by CFD simulations

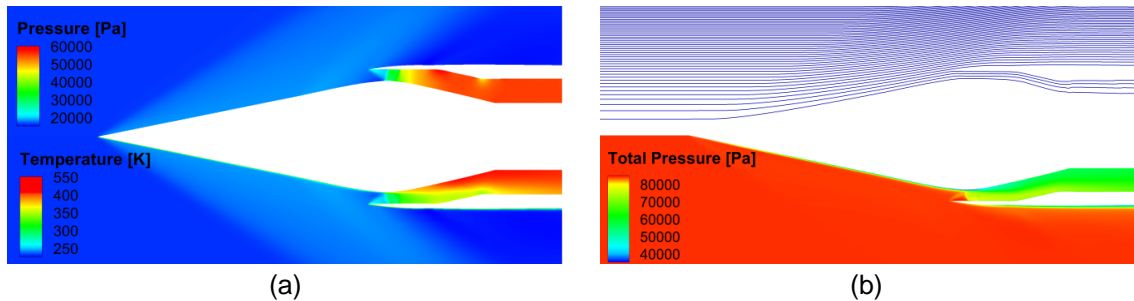


Figure 4.33: Pressure, temperature (a), streamlines and total pressure (b) distributions at $M_\infty = 2$, $H = 15$ km and $\alpha = 0^\circ$, computed by CFD simulations

A three-dimensional structured grid of 0.78 million hexahedral cells has been created in order to evaluate the alteration of the inlet performances as the angle of attack increases during the hypersonic cruise (Figure 4.34).

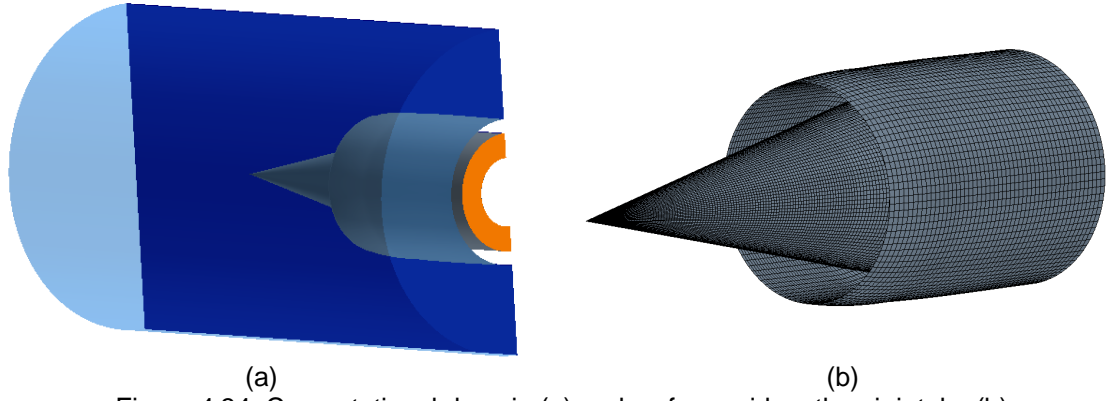


Figure 4.34: Computational domain (a) and surface grid on the air intake (b)

Figure 4.35 shows the flow field at an angle of attack of six degrees (expected maximum angle of attack during the cruise phase).

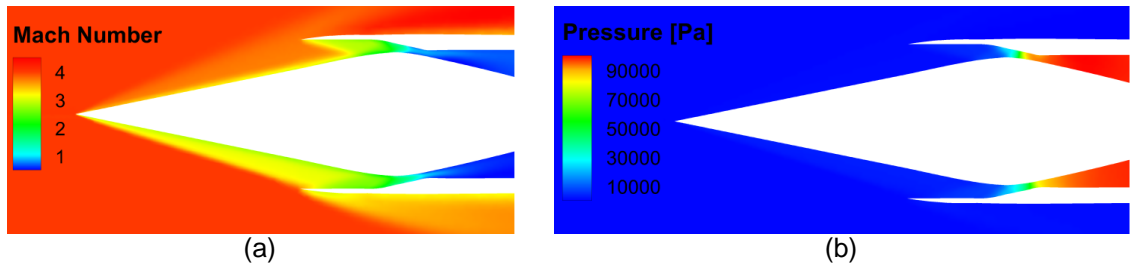


Figure 4.35: Mach number (a) and pressure (b) distributions at $M_\infty = 4$, $H = 30 \text{ km}$ and $AoA = 6^\circ$, computed by CFD simulations

The computed performances, in terms of mass capture and efficiency, for the different cases, are reported in Table 4.8. Results are in agreement with experimental and numerical results for similar air intakes available in literature [2]. Furthermore, the very limited deterioration of the inlet performances due to the asymmetry of the shock structures ensures a stable combustion during the hypersonic cruise.

	M_∞	$H \text{ [km]}$	$\alpha [^\circ]$	Mass capture [%]	Efficiency η
Nominal (Cruise)	4.0	30	0	100	0.617
Supersonic	2.0	15	0	35	0.662
Off-design (Cruise)	4.0	30	6	91	0.605

Table 4.8: Turbo-ramjet supersonic inlet main performances

4.5.3 Body-wing-tail-engine configuration

Engines have been integrated to the vehicle body-wing-tail configuration, to perform CFD analysis aimed at studying their effects on lift and drag coefficients for hypersonic cruise conditions.

Figure 4.36 shows the comparison between the computed surface pressure distribution for the configurations without and with engines, at zero angle of attack.

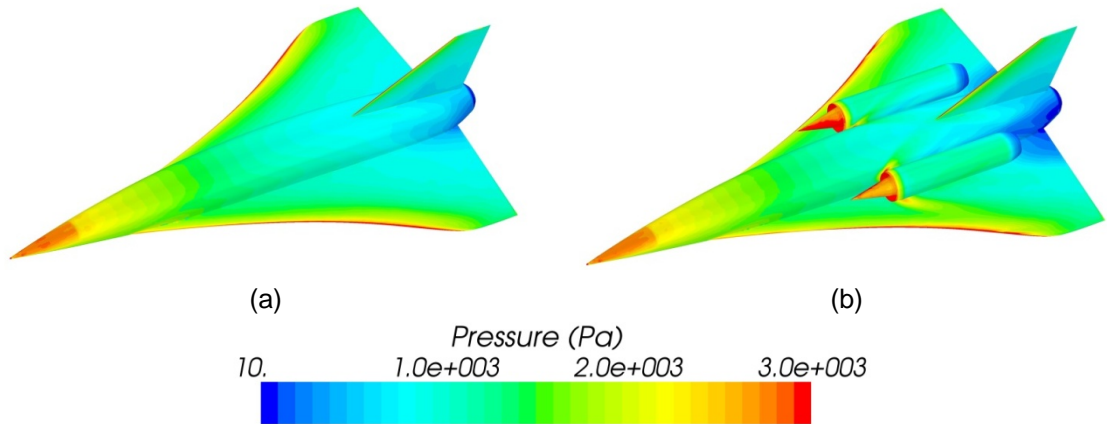


Figure 4.36: Pressure distribution for $M_\infty = 4$, $H = 30 \text{ km}$ and $\alpha = 0^\circ$ on the configuration without (a) and with engines (b), computed by CFD simulations

In Table 4.9 results provided by CFD simulations and Missile DATCOM software, for two hypersonic cruise conditions are reported.

It can be observed that the presence of the engines causes a relatively slight increase of drag force acting on the aircraft.

In particular for $\alpha=0^\circ$ Missile DATCOM and CFD predict a drag force increase of 4.5% and 12.5%, respectively. For $\alpha=4^\circ$ it can be observed a reduced discrepancy between the predictions of the two methods: CFD computes an increase of 21%, Missile DATCOM of 23%.

Configuration	Flight Condition			CFD		Missile DATCOM	
	M_∞	$H \text{ [km]}$	$\alpha [^\circ]$	c_L	c_D	c_L	c_D
Body-Wing-Tail	4.0	30	0	-0.0072	0.0088	0	0.008
Body-Wing-Tail-Engines				-0.0105	0.0094	0	0.009
Body-Wing-Tail	4.0	30	4	0.0529	0.012	0.077	0.013
Body-Wing-Tail-Engines				0.0572	0.0145	0.084	0.016

Table 4.9: Lift and drag coefficients during hypersonic cruise, for the configuration with and without engines, computed by CFD simulations and Missile DATCOM

References

- [1] T. J. Goldberg, J. N. Hefner, D. R. Stone, Hypersonic aerodynamic characteristics of two delta-wing X-15 airplane configurations, NASA TECHNICAL NOTE, TN D-5498 (1969)
- [2] S. Saha, D. Chakraborty, Hypersonic Intake Starting Characteristics—A CFD Validation Study, Defence Science Journal, Vol. 62, No. 3, pp. 147-152 (2012)

5 Aerodynamic database

In this chapter the aerodynamic database of the vehicle, achieved by Missile DATCOM, is presented. It refers to the complete vehicle configuration (body-wing-tail-engines-elevons-ailerons-rudder) and includes longitudinal and lateral-directional force and moment coefficients, static and dynamic derivatives, varying Mach number (from low subsonic to hypersonic regime), altitude (from sea level to 70 km), angle of attack (from -6° to 20°) and control surfaces deflections.

Longitudinal forces and moments are nondimensionalized by the freestream dynamic pressure and the reference area. In addition, longitudinal and lateral-directional moments are nondimensionalized by the reference lengths, which are the wing mean aerodynamic chord \bar{c} and the wingspan b , respectively.

The longitudinal (pitch rate) dynamic derivatives are nondimensionalized by the quantity $q\bar{c}/2V_\infty$, while lateral-directional (roll rate, yaw rate) dynamic derivatives are nondimensionalized by the quantities $pb/2V_\infty$ and $rb/2V_\infty$, respectively.

Aerodynamic moments are evaluated with respect to a pole at 15 m distance from the apex of the nose, which corresponds to an intermediate position of the vehicle CoG as the propellant is consumed (Figure 2.8).

5.1 Longitudinal aerodynamic coefficients

Figures 5.1-3 show the behaviour of longitudinal aerodynamic coefficients with angle of attack for different values of Mach number. The lift and pitching moment coefficient have an almost linear profile in the examined range of angles of attack, while the drag coefficient presents the typical parabolic behaviour.

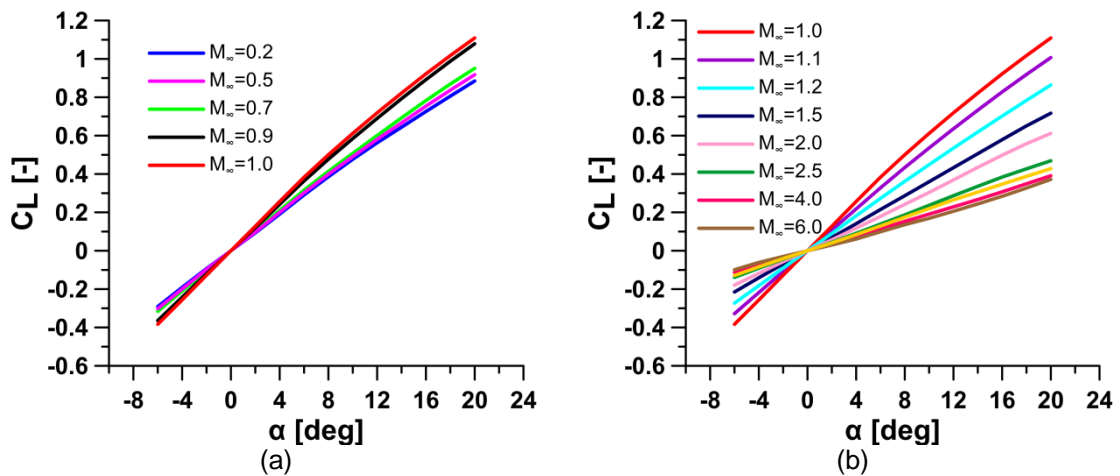


Figure 5.1: Lift coefficient as a function of angle of attack at different Mach numbers. Subsonic (a) and supersonic (b) regimes

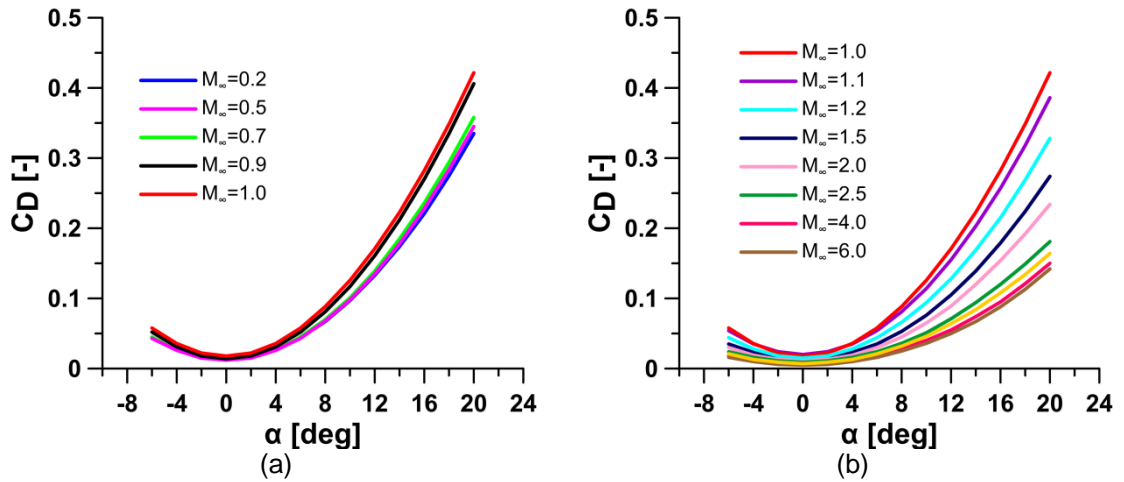


Figure 5.2: Drag coefficient as a function of angle of attack at different Mach numbers. Subsonic (a) and supersonic (b) regimes

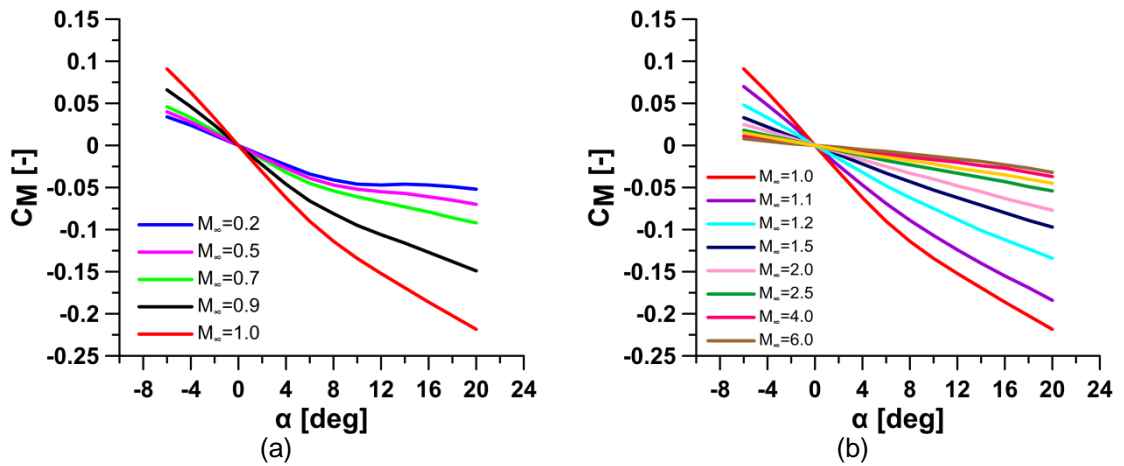


Figure 5.3: Pitching moment coefficient as a function of angle of attack at different Mach numbers. Subsonic (a) and supersonic (b) regimes

Figure 5.4 shows the behaviour of the lift and drag coefficients with the freestream Mach number, at different angles of attack. The coefficients rise with Mach number in the subsonic regime, especially at high angles of attack, reaching a maximum at about $M_\infty=1$, then decrease in the super-hypersonic regime, approaching at a constant value. The trend of the pitching moment coefficients varying the freestream Mach number is also presented in Figure 5.5, for different angles of attack.

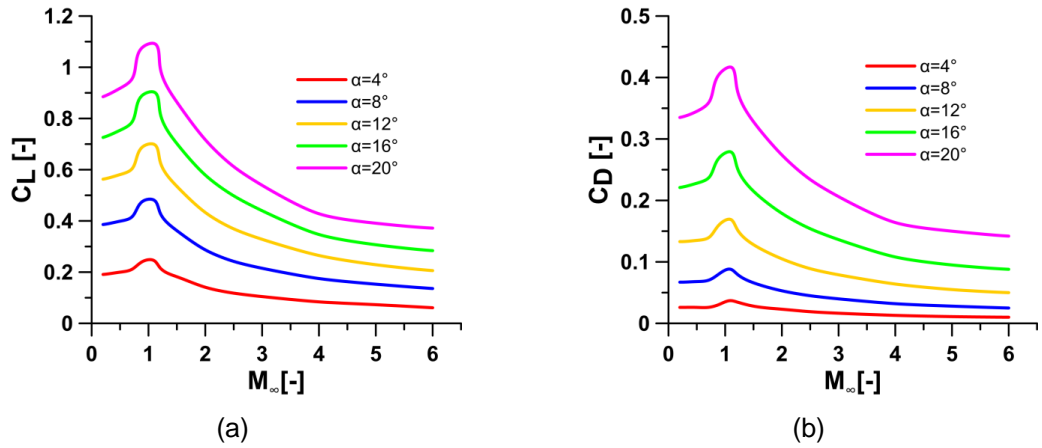


Figure 5.4: Lift (a) and drag (b) coefficients as a function of Mach number, at different angles of attack

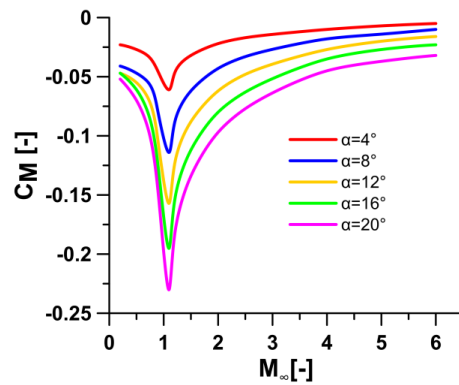


Figure 5.5: Pitching moment coefficient as a function of Mach number, at different angles of attack

The dependence of lift and pitching moment coefficient on altitude is negligible, while the effect of altitude on drag coefficient has been taken into account. Figure 5.6 shows the drag coefficient as a function of angle of attack, at Mach number of 4, at five different altitudes from 10 to 70 km.

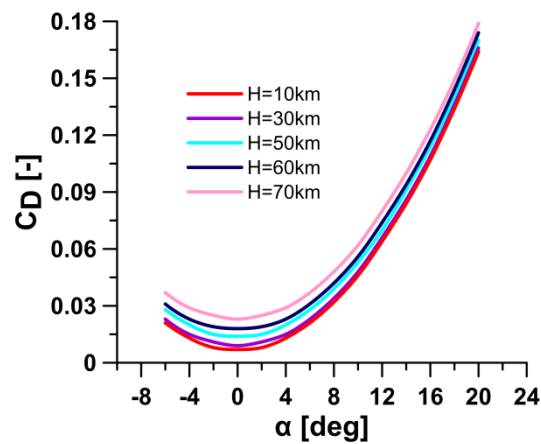


Figure 5.6: Drag coefficient as a function of angle of attack at different altitudes ($M_\infty = 4$)

A comparison with other super-hypersonic vehicles, in terms of lift-to-drag ratio in the cruise phase, has been carried out.

In Figure 5.8 cruise aerodynamic efficiency values performed by a series of super-hypersonic vehicles, including HyPlane (illustrated in Figure 5.7), are reported, along with the Kuchemann's empirical relationship, known as the " L/D barrier" [1].

As well known, high L/D are very difficult to achieve at high Mach numbers, due to the strong viscous effects and shock waves that vehicles suffer in these conditions.

HyPlane vehicle, characterized by a slender shape and sharp leading edges that allow minimizing the super-hypersonic wave drag produced by the wing, exhibits a hypersonic L/D_{cruise} of approximately 4.0. This value is intermediate between the aerodynamic efficiency performed by supersonic business jets and the X-15, flying at Mach 5.

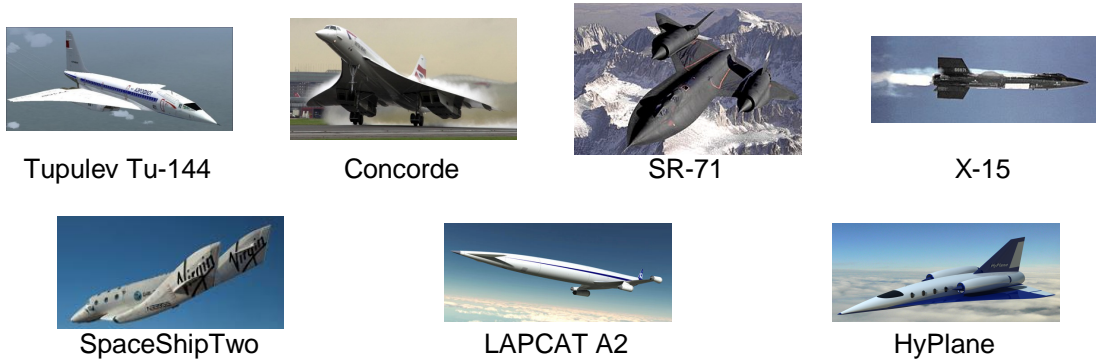


Figure 5.7: Super-hypersonic vehicle configurations

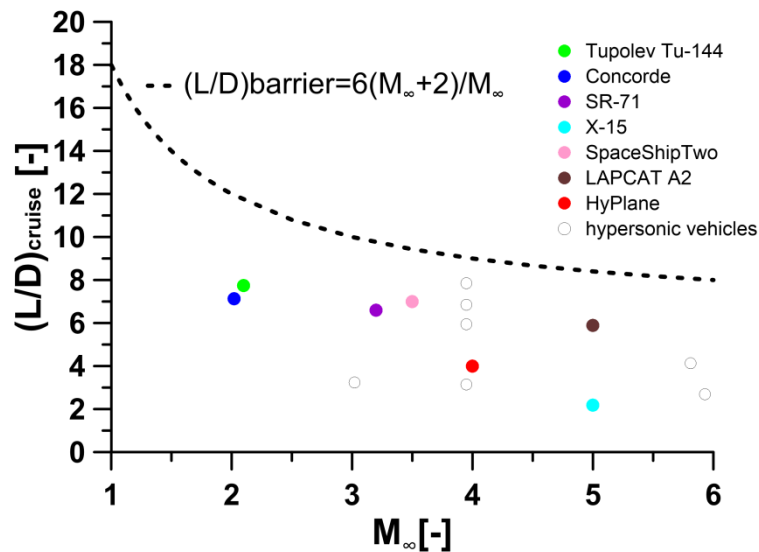


Figure 5.8: Cruise lift-to-drag ratio for super-hypersonic vehicles and the " L/D barrier"

5.2 Lateral-directional derivatives

In this section the trends of the vehicle aerodynamic derivatives are presented, both static and dynamic, both longitudinal and lateral-directional, as a function of angle of attack and Mach number.

Side force coefficient derivative with sideslip angle is presented in Figure 5.9 while rolling and yawing moment coefficients derivatives with sideslip angle are presented in Figure 5.10, as a function of angle of attack, at different Mach numbers.

Lateral-directional stability criteria ($c_{Y\beta} < 0$, $c_{l\beta} < 0$, $c_{N\beta} > 0$) are met for all the HyPlane effective operative conditions.

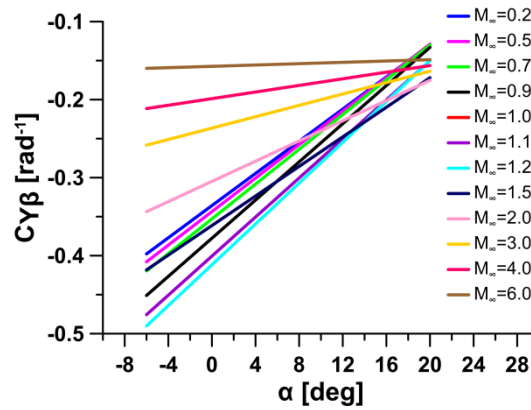


Figure 5.9: Side force coefficient derivative with sideslip angle as a function of angle of attack, at different Mach numbers

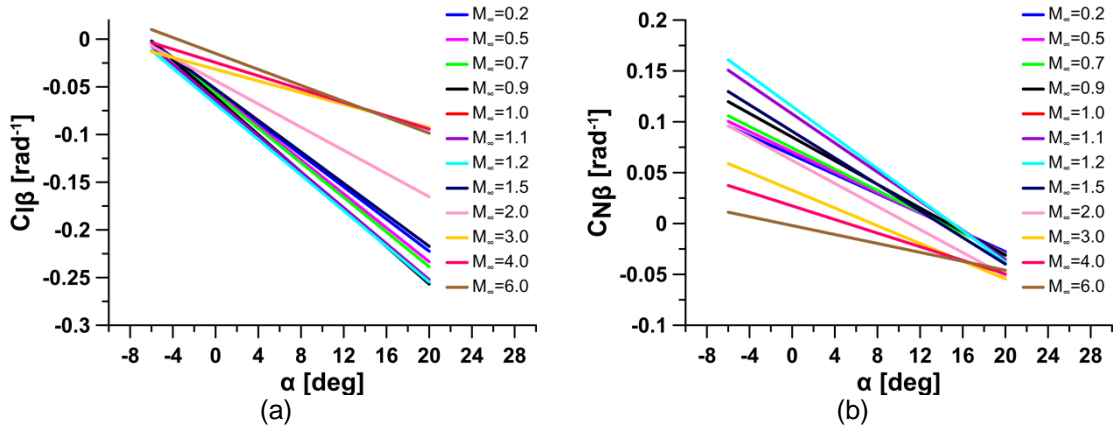


Figure 5.10: Rolling (a) and yawing (b) moment coefficients derivatives with sideslip angle as a function of angle of attack, at different Mach numbers

5.3 Dynamic derivatives

In this section dynamic derivatives are presented, both longitudinal and lateral-directional. Figures 5.11 and 5.12 show lift and pitching moment coefficients derivatives with rate of change of angle of attack and with pitch rate as a function of Mach number.

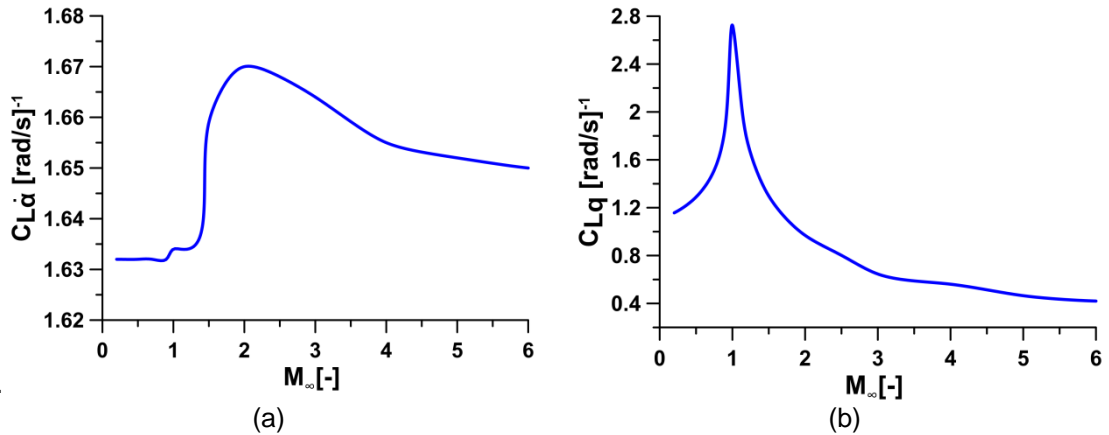


Figure 5.11: Lift derivative with rate of change of angle of attack (a) and pitch rate (b) as a function of Mach number

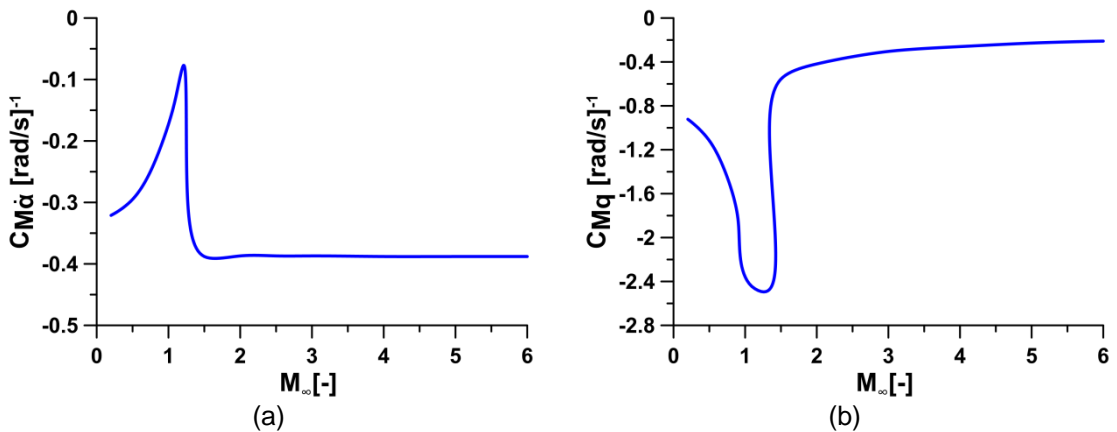


Figure 5.12: Pitching moment derivative with rate of change of angle of attack (a) and pitch rate (b) as a function of Mach number

In Figures 5.13-15 side force, rolling moment and yawing moment coefficients derivatives with roll and yaw rates, as a function of Mach number, are presented.

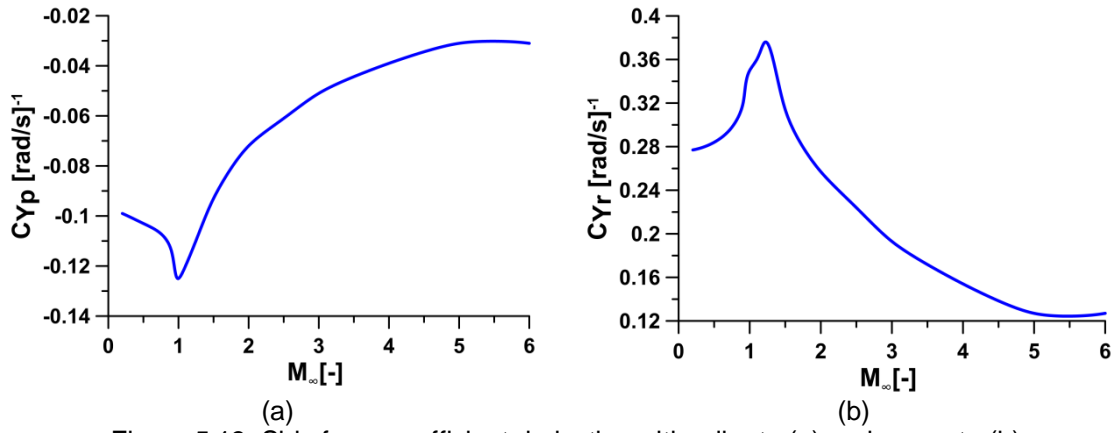


Figure 5.13: Side force coefficient derivative with roll rate (a) and yaw rate (b) as a function of Mach number

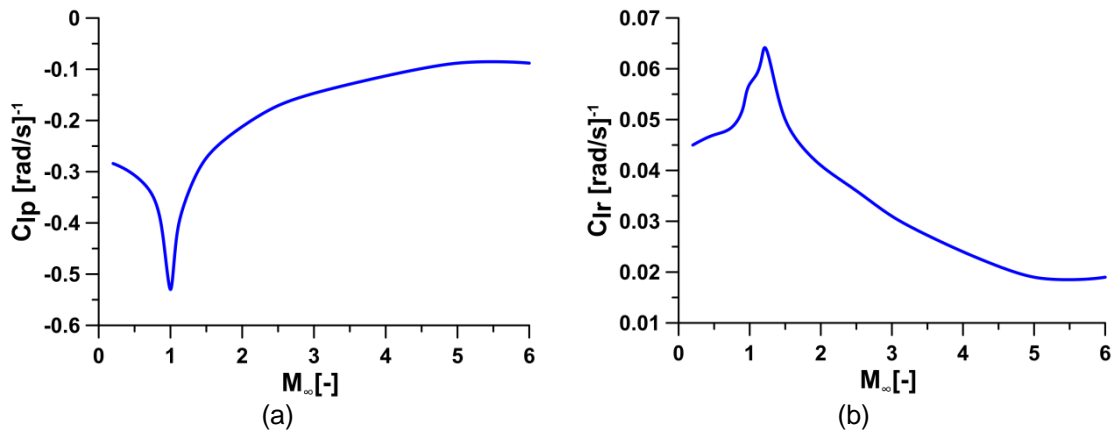


Figure 5.14: Rolling moment coefficient derivative with roll rate (a) and yaw rate (b) as a function of Mach number

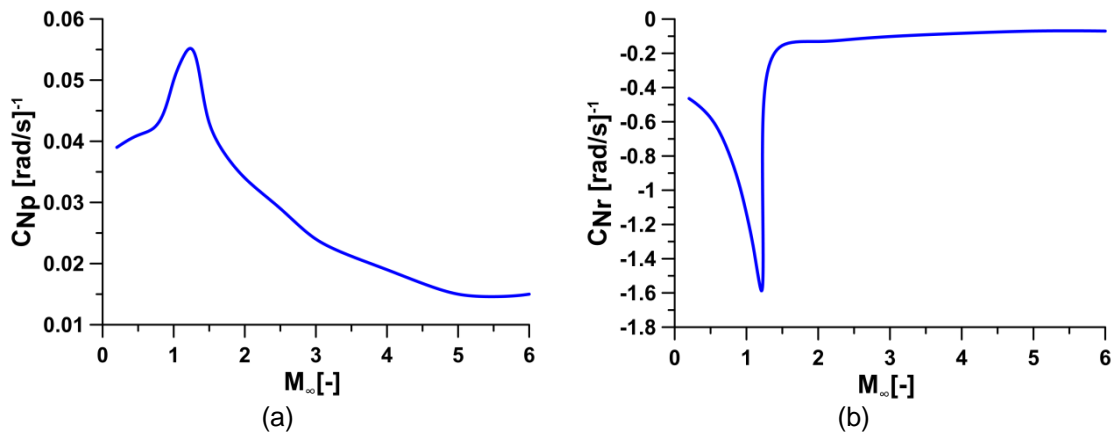


Figure 5.15: Yawing moment coefficient derivative with roll rate (a) and yaw rate (b) as a function of Mach number

Longitudinal and lateral-directional stability criteria ($c_{Mq} < 0$, $c_{lp} < 0$, $c_{Nr} < 0$) are met for all flight conditions.

5.4 Effect of control surface deflection

5.4.1 Elevons effect

Figures 5.16-17 show the contributes to lift, drag and pitching moment coefficients due to pitch control surfaces.

Results are presented as a function of the elevons deflection angle δ_e , at different Mach numbers. The elevons deflection is assumed positive when both the elevons are deflected downward. With this convention a positive elevons deflection produces a negative pitching moment.

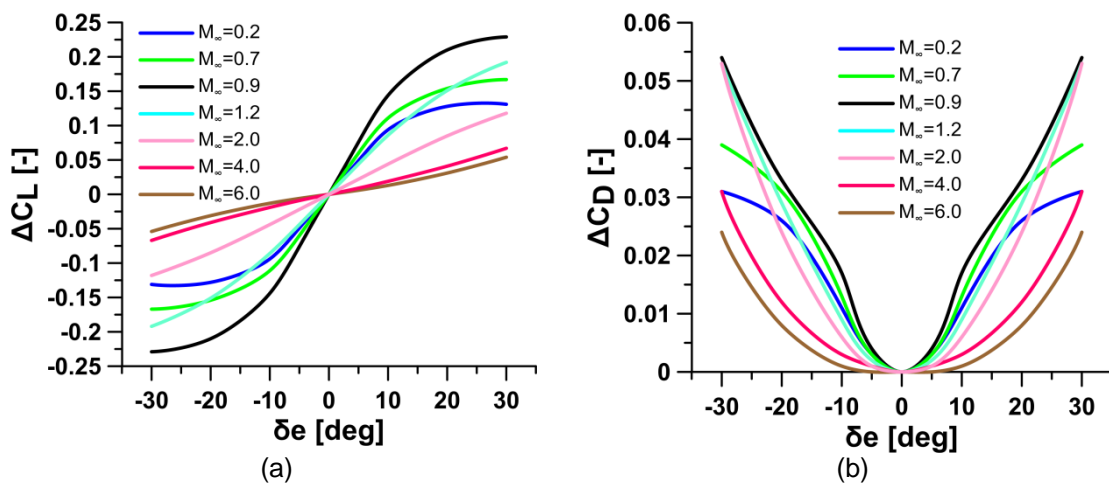


Figure 5.16: Contributes to lift (a) and drag (b) coefficients as a function of elevons deflection angle, at different Mach numbers

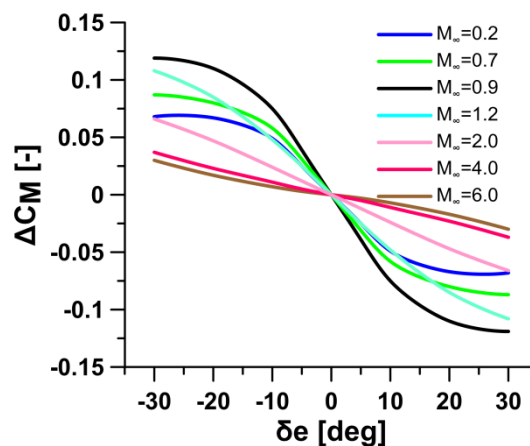


Figure 5.17: Contribute to pitching moment coefficient as a function on elevons deflection angle, at different Mach numbers

5.4.2 Ailerons effect

Figures 5.18-19 show the contributes to lift, drag, pitching and rolling moment coefficients due to roll control surfaces.

Results are presented as a function of the right aileron deflection angle δ_a , at different Mach numbers. The deflection is assumed positive when the right aileron is deflected downward. With this convention a positive aileron deflection produces a rolling moment to the left (negative). The contribute to yawing moment coefficient (adverse yaw) is also presented in Figure 5.20.

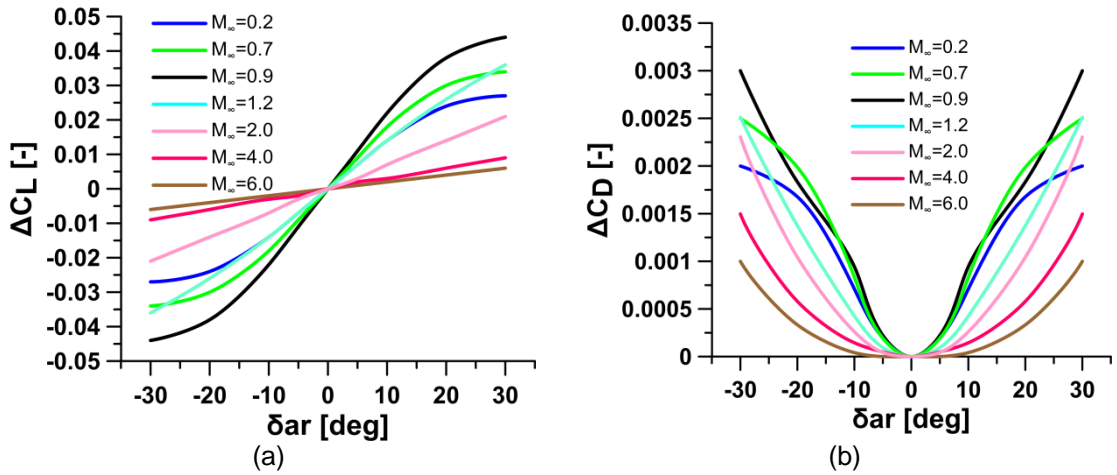


Figure 5.18: Contributes to lift (a) and drag (b) coefficients as a function of aileron deflection angle, at different Mach numbers

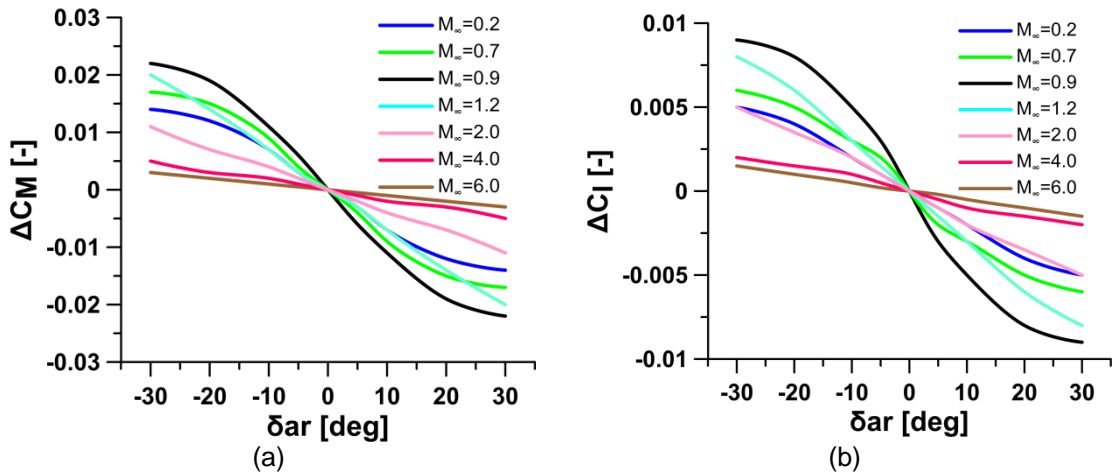


Figure 5.19: Contributes to pitching (a) and rolling (b) moment coefficients as function of aileron deflection angle, at different Mach numbers

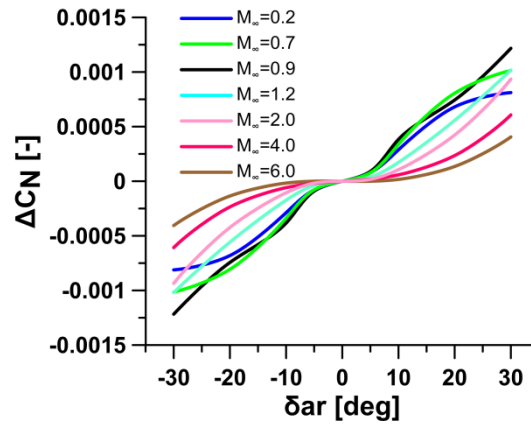


Figure 5.20: Contributes to Yawing moment coefficients as function of aileron deflection angle, at different Mach numbers

5.4.3 Rudder effect

Figure 5.21 shows the contributes to drag and side force coefficients due to yaw control surfaces. The contributes to yawing moment coefficient and rolling moment coefficients (induced roll) are also presented in Figure 5.22.

Results are presented as a function of the rudder deflection angle δ_r , at different Mach numbers. The rudder deflection is assumed positive when the rudder trailing edge is deflected left. With this convention a positive elevons deflection produces a negative yawing moment.

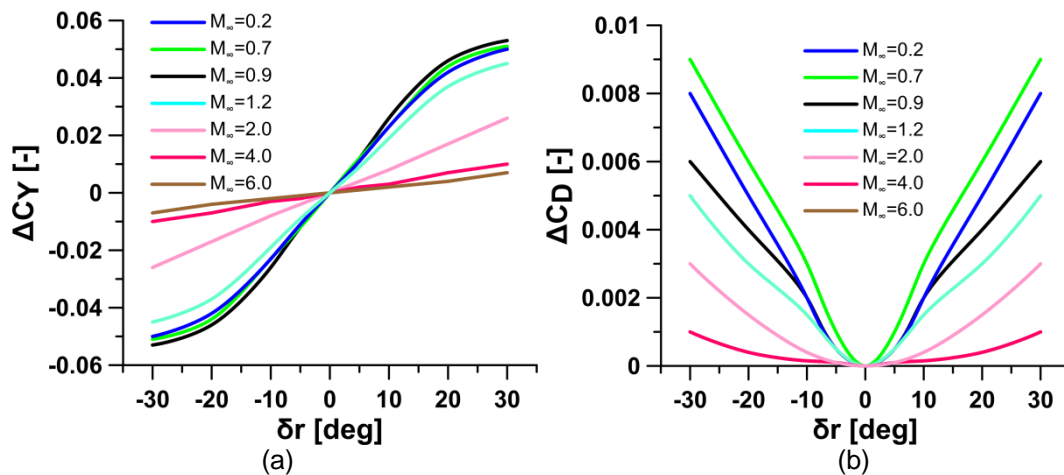


Figure 5.21: Contributes to Drag (a) and Side force (b) coefficients as a function of ailerons deflection angle, at different Mach number

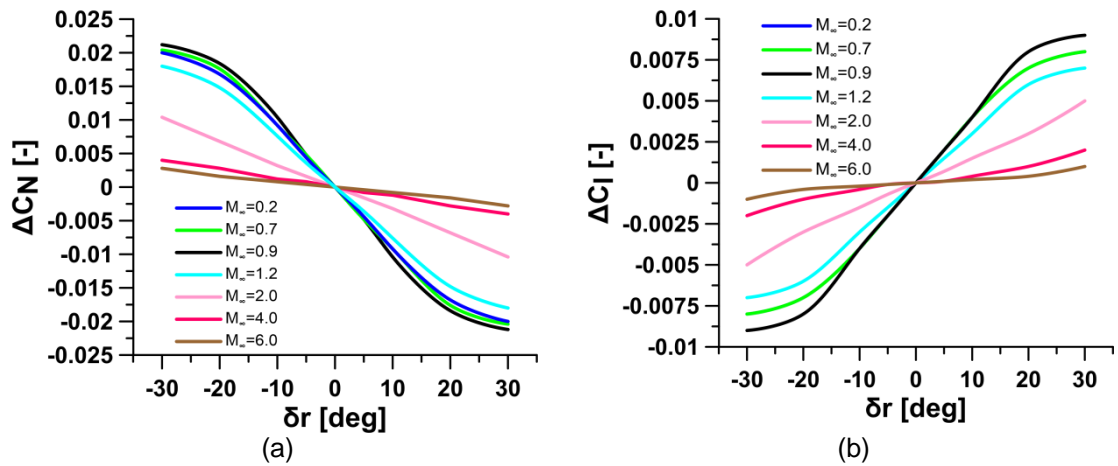


Figure 5.22: Contributes to Yawing (a) and Rolling (b) moment coefficients as a function of ailerons deflection angle, at different Mach number

References

- [1] J. D. Anderson Jr., Hypersonic and High Temperature Gas Dynamics, American Institute of Aeronautics and Astronautics (2000)

6 Aerodynamic heating and preliminary materials identification

The aerodynamic heating is one of the problems during the super-hypersonic flight, due to the high convective heat fluxes on the outer surface of the vehicle, dictated by the very high speeds. Convective heat flux is partly conducted to the solid and partly radiated into the atmosphere. When conduction in the solid may be neglected (i.e. for materials with very low thermal conductivity) and a steady state is achieved, a "radiative equilibrium" is established, in the sense that the overall surface convective heat flux is perfectly balanced by the overall surface radiative flux. The corresponding surface temperature is known as "radiative equilibrium temperature" [1].

This chapter is devoted to the numerical prediction by CFD simulations of the thermal loads acting on the vehicle, during cruise phase (the most severe condition in terms of aerodynamic heating), with particular attention to the most thermally stressed parts, namely the nose and the wing leading edges).

The aerodynamic heating and then the surface temperature distributions strongly depend on the boundary layer laminar-turbulent transition. In fact the transition process has a dramatic effect on many integral quantities. The boundary layer thickness and the momentum thickness roughly double, skin friction and heat transfer significantly increase in the transition region and in the turbulent region heat transfer can be almost an order of magnitude higher than laminar heating.

For this reason a CFD analysis aimed at the assessment of the boundary layer transition process has been performed. The analysis, reported in the first section of this chapter, has revealed that a fully turbulent boundary layer must be assumed for the materials identification, because the assumption of laminar regime would underestimate heat fluxes and then temperatures reached by the vehicle surface.

On the basis of thermal loads computed assuming fully turbulent boundary layer, presented in the second section, a preliminary materials identification has been proposed, in the third section.

6.1 Boundary layer laminar-turbulent transition assessment

The boundary layer laminar-turbulent transition process is dependent upon a number of parameters. The transition process is affected by geometry, Mach and Reynolds numbers, angle of attack, surface temperature, chemistry effects and a number of minor effects. Also the receptivity of the boundary layer to free stream disturbances, surface roughness and body vibrations allows the appearance and growth of instabilities that, ultimately, lead to transition to turbulence [2].

In this section a CFD analysis aimed at the assessment of the boundary layer transition process, on HyPlane fuselage and wing, in the hypersonic cruise conditions, is presented. The process has been predicted adopting $\gamma - Re_\theta$ transition model. The model has been at first applied to predict the transition on a flat plate in hypersonic conditions, producing results in reasonably agreement with experimental data.

6.1.1 A case study: flat plate in hypersonic regime

A CFD analysis aimed at predicting the laminar-turbulent transition on a isothermal flat plate in hypersonic condition has been carried out, in order to validate the adopted $\gamma - Re_\theta$ transition model, by comparing numerical results with experimental data achieved at NASA Langley Research Center [3].

Numerical solutions have been obtained by solving steady state, compressible RANS equations, using a coupled implicit numerical resolution scheme.

The flow conditions are reported in Table 6.1, where M_∞ , T_∞ and Re_∞ are the freestream Mach number, temperature and Reynolds number, respectively, and T_w is the wall temperature.

M_∞	$T_\infty[K]$	$Re_\infty[1/m]$	$T_w[K]$
6.0	65.04	$2.638 \cdot 10^7$	106.67

Table 6.1: Flow conditions for flat plate test

Since the boundary layer is very thin and the normal gradient of flow field parameters is very large, the computational grid must be constructed with sufficient attention, in order to simulate accurately the structure of the flow field in the boundary layer [4]. In fact the adopted $\gamma - Re_\theta$ transition model requires a high-quality, refined low Reynolds number mesh, with near-wall spacing such as $y^+ = \frac{\sqrt{\rho\tau_w}y}{\mu}$ is between 0.1 and 1 [5].

A two-dimensional structured computational grid of about 31000 quadrilateral cells has been generated. The grid, illustrated in Figure 6.1, is characterized by a near wall layer thickness of 10^{-7} and satisfies the constraint on y^+ .

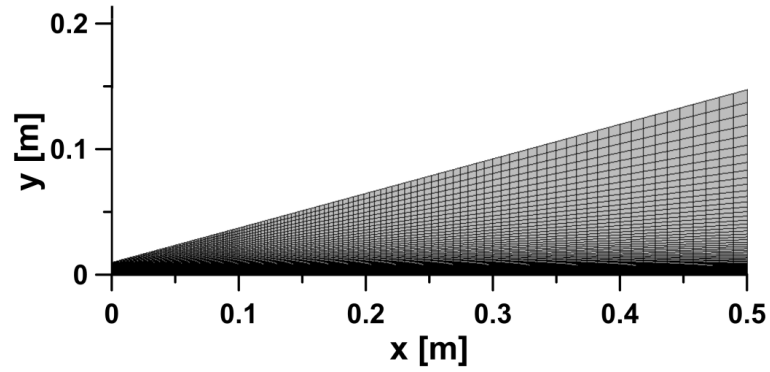


Figure 6.1: 2D structured hypersonic flat plate grid

Comparison between CFD predictions and experimental data, in terms of Stanton number variation as a function of the local Reynolds number are shown in Figure 6.2.

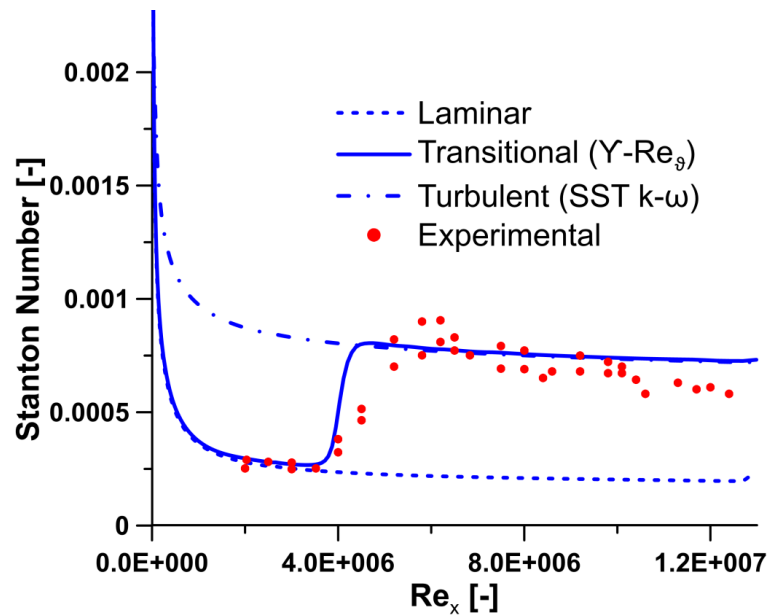


Figure 6.2: Stanton number variation as a function of the local Reynolds number. Comparison between numerical and experimental results

Numerical results of the transitional case and experimental data were quite close. In particular the Stanton number trend in laminar conditions and the transition start are excellently predicted by the numerical simulation. The transition process duration and the Stanton number peak are relatively slight underestimated by the model. The Stanton number trend in turbulent conditions had a certain difference that could be considered acceptable according to the spreading law of the experimental data. However, the overall curve trend basically matched, and then it is possible to retain the adopted turbulence model able to reasonably reflect the development process of turbulence.

6.1.2 Application to HyPlane fuselage and wing

The assessment of the boundary layer transition on HyPlane fuselage and wing, in hypersonic cruise conditions (Table 6.2), has been achieved by solving steady state, compressible RANS equations, using a coupled implicit numerical resolution scheme. An emissivity of 0.8, a reflectivity of 0.2 (and, consequently, a zero transmissivity) have been assigned to the vehicle surface.

M_∞	$H[km]$	$\alpha [deg]$
4	30	0

Table 6.2: Flow conditions for the assessment of the boundary layer transition process on HyPlane fuselage and wing

The three cases summarized in Table 6.3 have been analyzed, both for fuselage and wing of the vehicle under investigation, in order to identify the most critical conditions in terms of aerodynamic heating.

Cases	Boundary layer	Viscous Model
1	Laminar	-
2	Transitional	$\gamma - Re_\theta$ laminar-turbulent transition model
3	Fully turbulent	SST (Menter) $k - \omega$ turbulence model

Table 6.3: Studied cases for aerodynamic heating evaluation on HyPlane fuselage and wing

Fuselage

The considered computational domain has an overall length of about two times the length of the fuselage. A structured grid of about 5.2 million cells, which fulfils the mentioned requirement for wall y^+ , has been generated (Figure 6.3).

Special attention has been paid to the nose, because of its small curvature radius (3 cm), in order to better capture the flow gradients in the solution. Figure 6.3 shows the computational domain and the surface grid on the fuselage forefront.

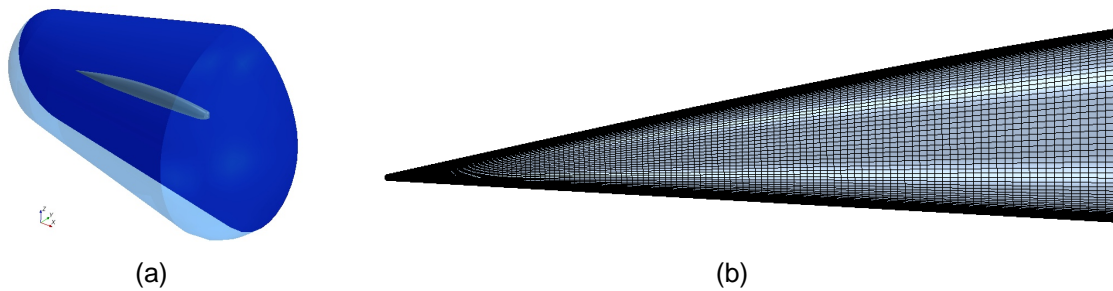


Figure 6.3: Computational domain (a) and surface grid (b) on the vehicle fuselage forefront

Figure 6.4 shows the surface radiative equilibrium temperature distributions on the fuselage forefront, for the three analyzed cases.

It is evident that the temperature jump caused by the laminar-turbulent transition is predicted to occur in different longitudinal stations, depending on the roll position.

This is evidently due to the fact that the fuselage is not axisymmetric.

In particular on the symmetry plane, on the upper side, the transition process is predicted to start at about $X=0.5$ m, before elsewhere, where the temperature discontinuity occurs up to about $X=5$ m.

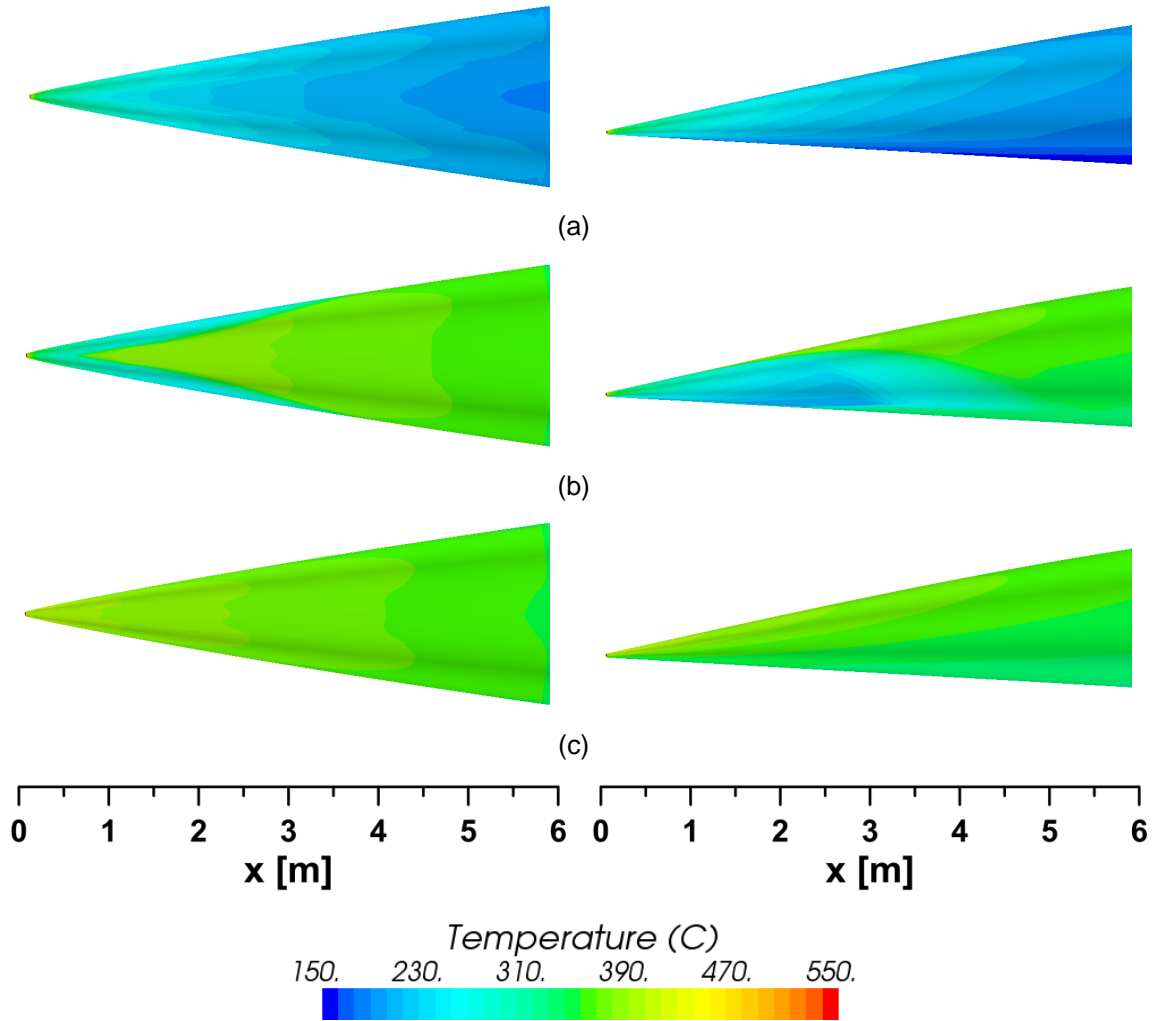


Figure 6.4: Radiative equilibrium temperature distribution on the vehicle forefront fuselage ($M_\infty = 4$, $H = 30 \text{ km}$, $\alpha = 0^\circ$). Laminar (a), transitional (b) and fully turbulent (c) boundary layer

Figure 6.5 shows the radiative equilibrium temperature variation along the fuselage (on the symmetry plane, upper side) for laminar, transitional and fully turbulent boundary layer.

For the identification of the materials able to sustain the hypersonic phase, the fully turbulent CFD solution must be taken into account, which is the most severe in terms of surface temperature peak and distribution.

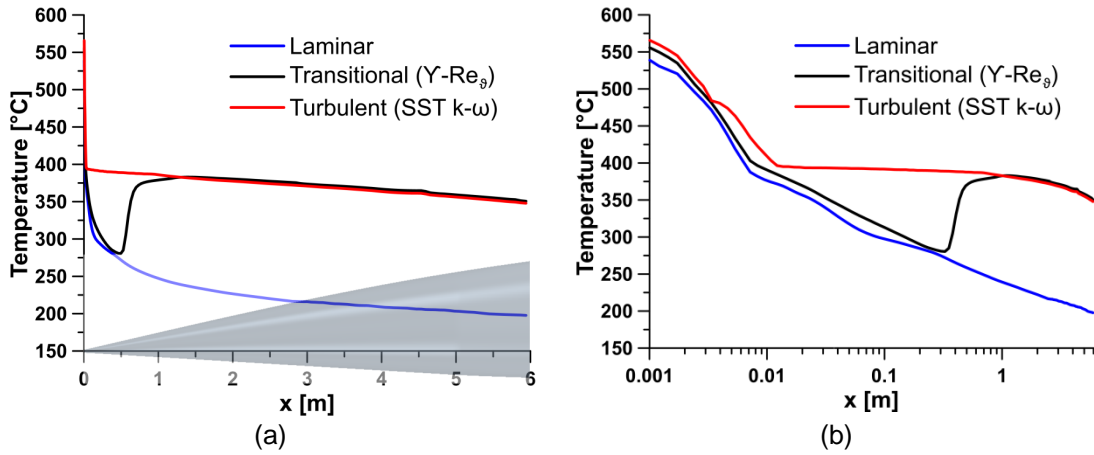


Figure 6.5: Radiative equilibrium temperature variation along the vehicle forefront fuselage for laminar, transitional and fully turbulent boundary layer ($M_\infty = 4$, $H = 30$ km, $\alpha = 0^\circ$). Linear scale (a) and logarithmic scale (b) for the X axis

In figure 6.6 the turbulence intensity and intermittency γ distributions on the symmetry plane are presented. A γ value of 0 suggests laminar flow and a value of 1 refers to fully turbulent flow. In both the contours it is possible to clearly visualize the onset of transition of the flow from laminar to turbulent.

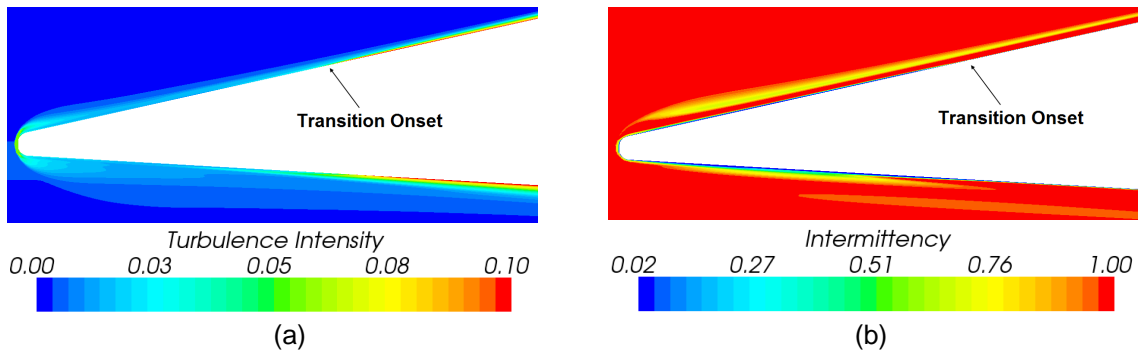
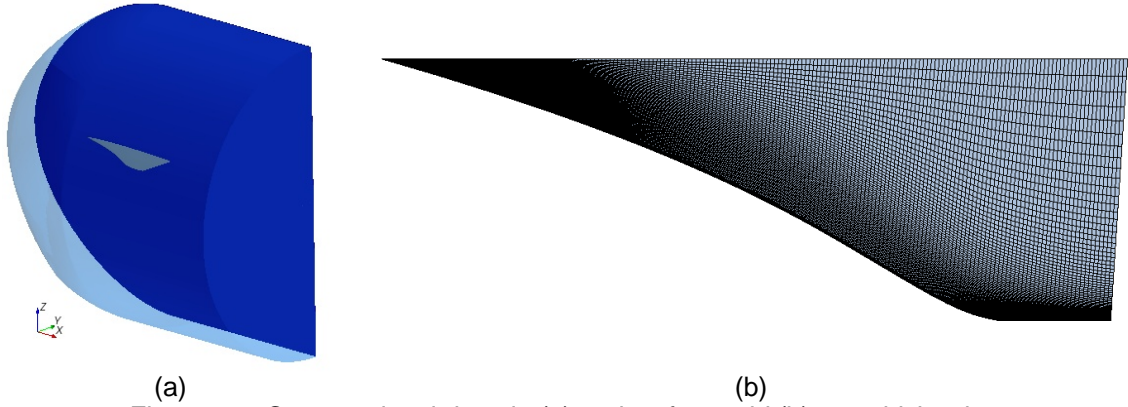


Figure 6.6: Turbulence intensity (a) and intermittency (b) distributions on the symmetry plane ($M_\infty = 4$, $H = 30$ km, $\alpha = 0^\circ$)

Wing

The considered computational domain has been discretized in a structured grid of about 6.5 million cells, which satisfy the requirement for wall y^+ (Figure 6.7). Special attention is paid to the leading edge because of its small curvature radius.



(a) (b)
Figure 6.7: Computational domain (a) and surface grid (b) on vehicle wing

In Figure 6.8 the radiative equilibrium temperature distribution on the vehicle wing is illustrated for the three different analyzed cases. It is possible to observe that the temperature jump caused by the laminar-turbulent transition roughly follows the variable delta wing shape.

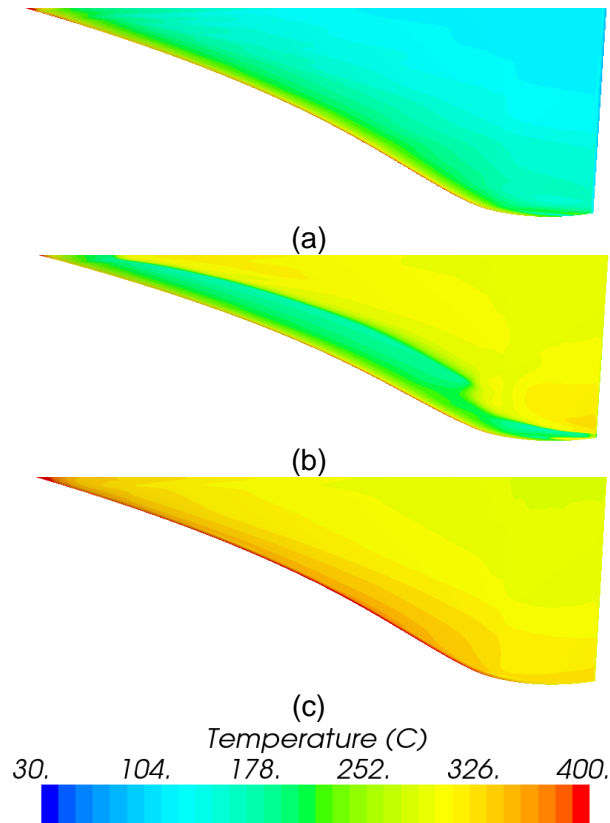


Figure 6.8: Radiative equilibrium temperature distribution on the vehicle wing ($M_\infty = 4$, $H = 30 \text{ km}$, $\alpha = 0^\circ$). Laminar (a), transitional (b), fully turbulent (c) boundary layer

In Figure 6.9 the radiative equilibrium temperature along the vehicle wing mean aerodynamic chord for laminar, transitional and fully turbulent boundary layer, is reported. The transition process starts at about $20\% \bar{c}$. The boundary layer becomes fully turbulent almost at 40% of the chord.

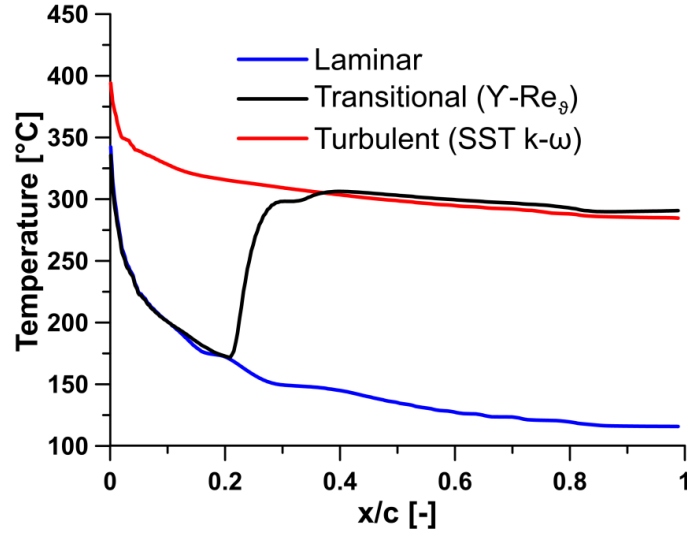


Figure 6.9: Temperature variation along the vehicle wing mean aerodynamic chord for laminar, transitional and turbulent boundary layer ($M_\infty = 4$, $H = 30 \text{ km}$, $\alpha = 0^\circ$)

In the turbulence intensity contour at mean aerodynamic chord span location (Figure 6.10) it is easy to recognize the transition process onset.

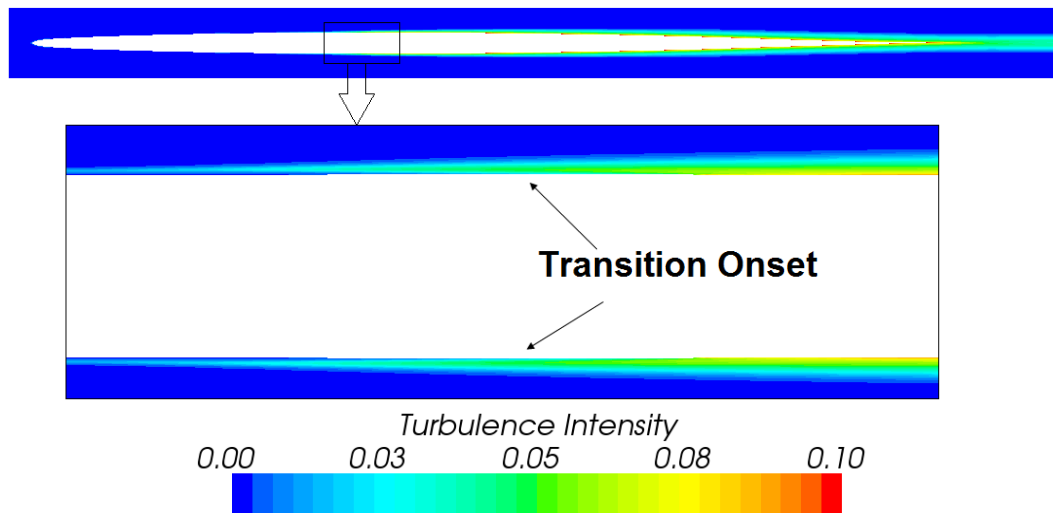


Figure 6.10: Turbulence intensity and intermittency distributions along on the symmetry plane ($M_\infty = 4$, $H = 30 \text{ km}$, $\alpha = 0^\circ$). Transitional (a) and fully turbulent (b) boundary layer.

Also in this case, for the identification of the materials able to sustain the cruise phase, the fully turbulent CFD solution must be taken into account.

6.2 Aero-thermal analysis

In this section more detailed results of the CFD analysis carried out assuming fully turbulent boundary layer are presented, for the vehicle nose and wing in hypersonic cruise conditions.

6.2.1 Nose

The distribution of the radiative equilibrium temperature on the nose is shown in Figure 6.11. The convective heat flux and the corresponding radiative equilibrium temperature variations along the symmetry plane are presented in Figure 6.12.

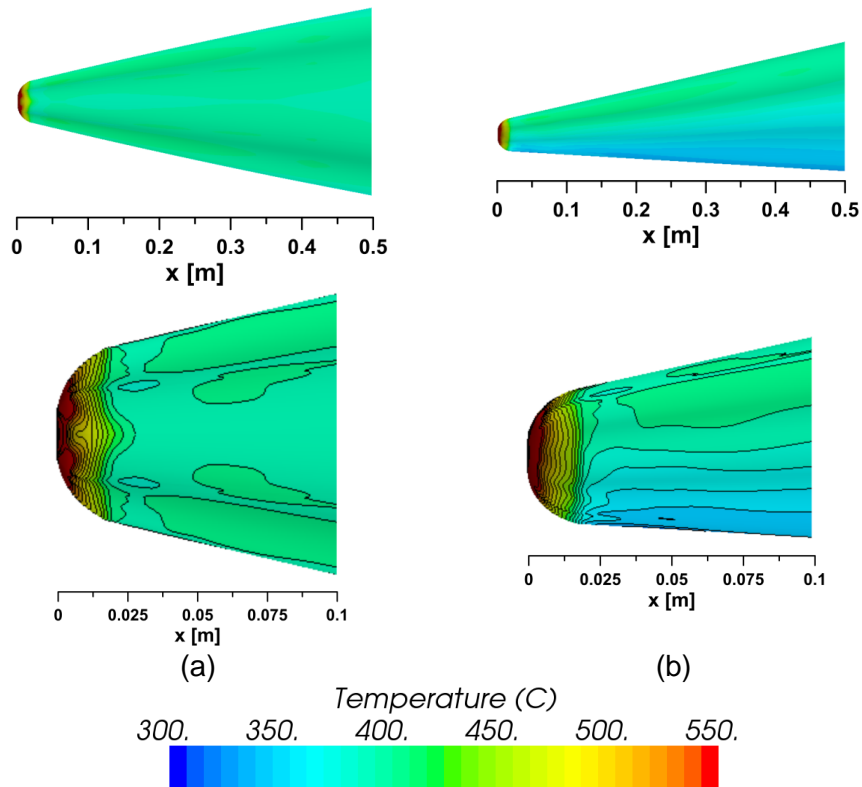


Figure 6.11: Radiative equilibrium temperature distribution on the vehicle nose at $M_\infty=4$, $H=30$ km and $\alpha=0^\circ$. Top view (a) and side view (b)

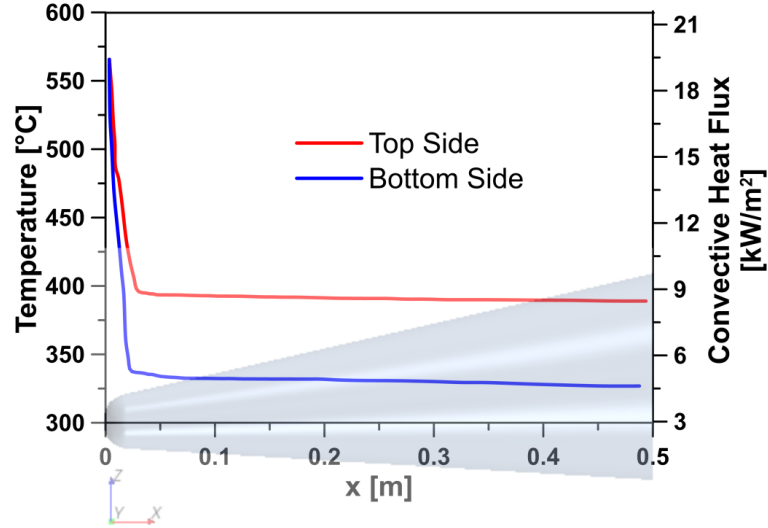


Figure 6.12: Convective heat flux and corresponding radiative equilibrium temperature along the vehicle nose at $M_\infty=4$, $H=30$ km and $\alpha=0^\circ$.

The Sutton and Graves engineering model [6] allows to analytically estimate the convective heat flux at the stagnation point of axisymmetric blunt bodies. The model is characterized by the equation:

$$q_{conv} = K_1 H \sqrt{\frac{\rho V^2}{R_n}}$$

where H is the total specific enthalpy, ρ is the air density, V is the flow velocity, R_n is the nose radius and $K = 3.6 \cdot 10^{-4} [kg^{\frac{1}{2}}/m]$ is a constant based on the gas composition. Radiative equilibrium temperature T_w can be computed by imposing the equilibrium between heat fluxes:

$$q_{conv} \left(1 - \frac{c_p T_w}{H} \right) - \sigma \varepsilon T_w^4 = 0$$

where $c_p = 1005 J/kgK$ and $\sigma = 5.67 \cdot 10^{-8} W/m^2K^4$ are the specific heat at constant pressure and the Stefan-Boltzmann constant, respectively.

This model predicts a surface stagnation-point temperature of $600^\circ C$, very close to the CFD result. In particular the semi-empirical method overpredicts the equilibrium temperature of 5%.

6.2.2 Wing

The distribution of the radiative equilibrium temperature is shown in Figure 6.13. The convective heat flux and radiative equilibrium temperature variations along different sections along the wing span (1 m, 2 m, 3 m and 4 m distance from the wing root) are presented in Figure 6.14.

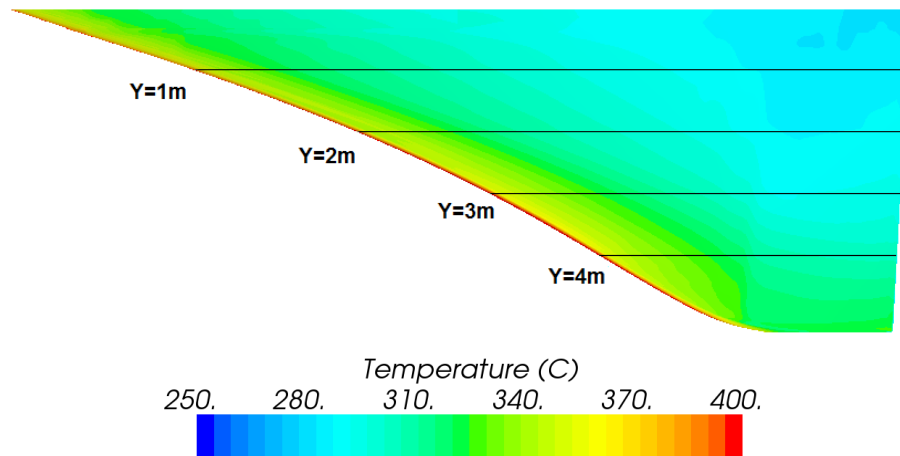


Figure 6.13: Radiative equilibrium temperature distribution on the wing at $M_\infty=4$, $H=30$ km and $\alpha=0^\circ$. Sections at 1 m, 2 m and 3 m distance from the wing root

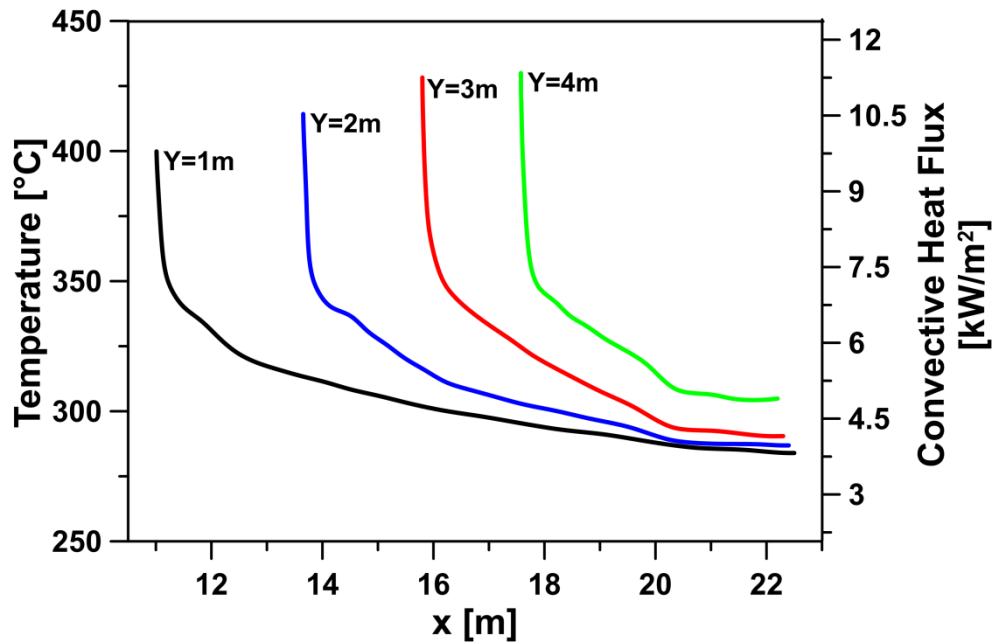


Figure 6.14: Convective heat flux and corresponding radiative equilibrium temperature along the considered wing sections at $M_\infty=4$, $H=30$ km and $\alpha=0^\circ$

It can be observed that stagnation convective heat flux and consequent radiative equilibrium temperature computed at wing leading edge are lower than the corresponding values calculated on vehicle nose, despite the wing leading edge radius of curvature is lower than nose one.

This result is due to geometrical factors. In fact Tauber [7] found that the stagnation convective heat flux on a cylindrical leading edge of a finite length wing is reduced of a factor $\sqrt{2}$, due to the wing bidimensionality effect, with respect to the one evaluated on a spherical nose. A further reduction factor depends on the leading edge sweep angle.

Along the span the peak temperature increases, as the wing leading edge radius of curvature decreases, until a maximum of about 430°C.

6.3 Preliminary materials assessment

On the basis of the equilibrium temperature complete distributions computed assuming a fully turbulent boundary layer, for the hypersonic cruise condition (Figure 6.15), three different areas have been identified with a possible material pre-selection, based on thermal resistance performances. Main idea is to apply advanced but available structural technologies with special thermal protection only for localized elements.

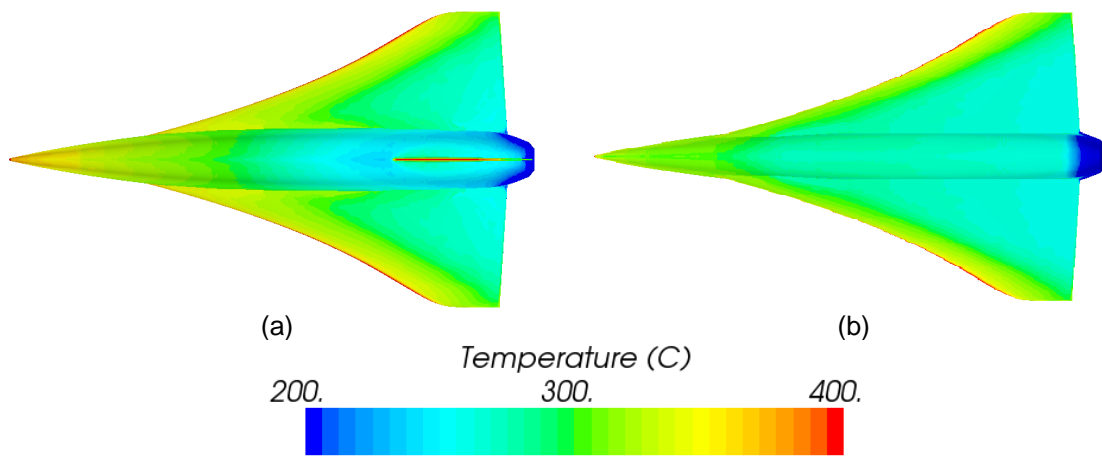


Figure 6.15: Radiation equilibrium temperature distribution for $M_\infty = 4$, $H = 30 \text{ km}$, $\alpha = 0^\circ$.
Leeside (a) and windside (b)

In particular, the following zones have been identified:

- Nose, wing and vertical tail leading edges and control surfaces reach temperatures above 400°C. For these areas carbon fiber reinforced ceramics composite materials (e.g Boron Carbide B_4C or Silicon Carbide SiC) could be used, as well as actively cooled solutions.
- Fuselage and wing surfaces are expected to be at temperature in the range 300-400°C. For such areas titanium alloys could be employed.
- For the aft fuselage, estimated to be exposed at temperature below 300°C, light temperature carbon fiber composite materials (e.g. Bismaleimides BMI) could be selected to gain weight with respect to titanium although the last remains to be applicable.

Such zone identification is shown in Figure 6.16. The main physical properties - density ρ , specific heat capacity c_p , thermal conductivity λ , melting point $T_{Melting}$ and emissivity ϵ - of the considered materials are reported in Table 6.4.

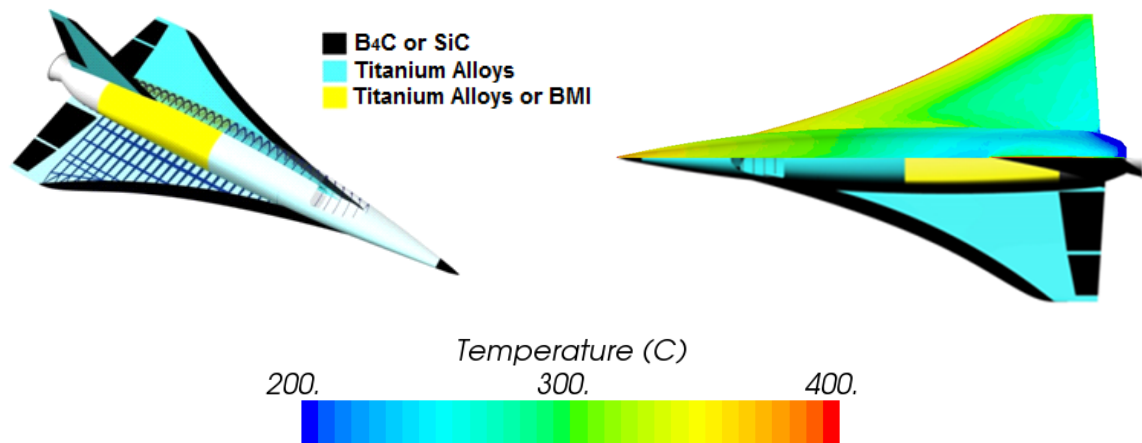


Figure 6.16: Preliminary structure and materials assessment

Materials	ρ [kg/m^3]	c_p [$J/kg \cdot K$]	λ [$W/m \cdot K$]	$T_{Melting}$ [K]	ϵ
Boron Carbide (B ₄ C)	2500	950	90	2723	0.8
Silicon Carbide (SiC)	3100	670	77.5-125.6	3070	0.8
Ti-3Al-2.5V	4480	525	11.8	1973	0.45

Table 6.4: Main properties of the identified materials

References

- [1] R. Savino, M. De Stefano Fumo, D. Paterna, M. Serpico, Aerothermodynamic Study of UHTC-based Thermal Protection Systems, Aerospace Science and Technology, Vol. 9, pp.151-160 (2005)
- [2] J. D. Anderson Jr., Hypersonic and High Temperature Gas Dynamics, American Institute of Aeronautics and Astronautics (2000)
- [3] D. D. Arthur, Evaluation of CFD turbulent heating prediction techniques and comparison with hypersonic experimental data, Technical Report NASA/CR-2001-210837 (2001)
- [4] X. Hong, S. Yuhe, W. Di, G. Xiaocheng, Computational Fluid Dynamics Simulation and Experimental Validation of Hypersonic Turbulence Boundary Layer, Research Journal of Applied Sciences, Engineering and Technology, 6(14): 2550-2560, ISSN: 2040-7459; e-ISSN: 2040-7467 (2013)
- [5] STAR-CCM+ (CD-adapco) Version 7.06 User Guide
- [6] K. Sutton, R. A. Graves, A general stagnation-point convective-heating equation for arbitrary gas mixtures, Technical Report TR-R-376, NASA (1971)
- [7] E. Tauber, A review of High-Speed, Convective, Heat-Transfer Computation Methods, Technical Paper TP- 2914, NASA (1989)

7 Preliminary trim performances

A six degree of freedom nonlinear dynamic model of the aircraft under investigation has been achieved by exploiting a flight simulation platform called MASLab (Multipurpose Aircraft Simulation Laboratory), developed by polytechnic of Turin, in the frame of the Clean Sky project [1].

The obtained model and a proper algorithm have allowed evaluating longitudinal trim performances. This study refers to an upgraded configuration, which meets pilot visibility and aircraft stability requirements.

In this chapter the criteria applied to refine the vehicle are briefly shown and the upgraded configuration is presented. Then the models adopted in the flight simulator and the trim algorithm are described. Finally the trim performances are reported.

7.1 Configuration upgrade

The vehicle configuration has been refined, in order to meet pilot visibility and stability requirements, while maintaining the hypersonic aerodynamic efficiency unaltered.

First of all the vehicle nose shape has been modified to improve the pilot field of view during landing phase, according to civil aircraft requirements. The central and rear parts of the body, which hold passengers and fuel tanks, have been left unchanged. This modification has resulted in the shortening of the vehicle fuselage of almost two meters.

In addition the vehicle original configuration has presented a longitudinal stability issue. In particular it has been found that at maximum takeoff weight and subsonic conditions, the vehicle center of gravity lies further from the nose than the total vehicle center of pressure. The problem is not experienced in supersonic flight conditions, where the center of pressure moves backward (lying at approximately $50\% \bar{c}$) and the center of gravity moves forward as the propellant is consumed (Figure 7.1).

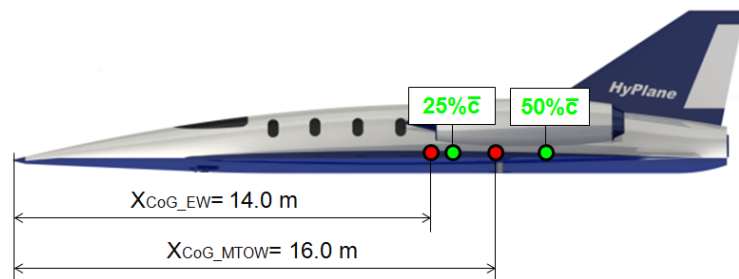


Figure 7.1: Longitudinal position of vehicle center of gravity at maximum takeoff weight and empty weight

Therefore the wing planform has been changed to ensure $(x_{CG} - x_{cp}) < 0$ for every computed position of the vehicle center of gravity and every flight regime. In particular

the upgraded wing planform presents a reduced root chord and an enlarged span, to move back the center of pressure in subsonic regime, while maintaining the same wing area.

Moreover vertical tail has been changed to guarantee, for the new wing-body configuration, directional stability ($C_{N\beta} > 0$) for all operative flight conditions.

The original and the upgraded configurations are illustrated in Figure 7.2. Main geometric parameters are reported in Table 7.1.

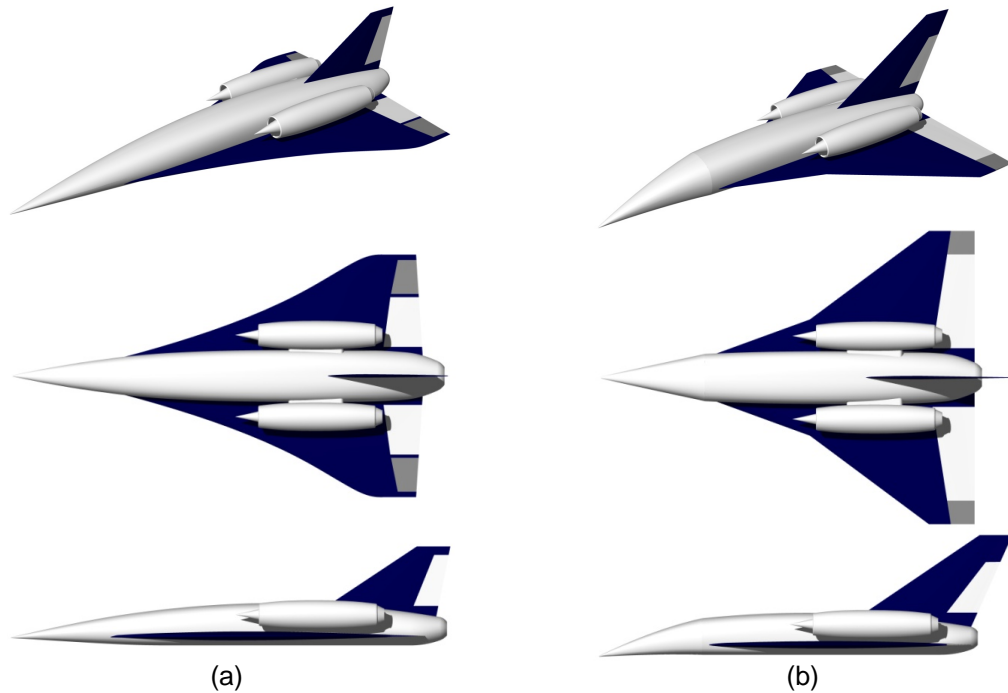


Figure 7.2: HyPlane original configuration (a) and upgraded configuration (b)

Geometric parameters	Original configuration	Upgraded Configuration
Fuselage length [m]	23.6	21.8
Nose Radius of Curvature [m]	0.03	0.03
Wing Area [m ²]	140	140.2
Wing Span [m]	13.5	16
Aspect Ratio	1.3	1.8
Wing Chord at Root [m]	16.7	14.4
Wing Chord at Tip [m]	2.5	2.5
Wing Mean Aerodynamic Chord [m]	12	11
Vertical Tail Span [m]	3.6	4.5
Vertical Tail Area [m ²]	14	18
Vertical Tail Chord at Root [m]	6.4	6.2
Vertical Tail Chord at Tip [m]	1.8	1.8
Vertical Tail Sweep [deg]	57	57

Table 7.1: HyPlane configurations main geometric features

Figures 7.3 and 7.4 show the upgraded vehicle CoG longitudinal position and inertia properties, as the propellant is consumed. These quantities have been evaluated taking advantage of a CATIA tool.

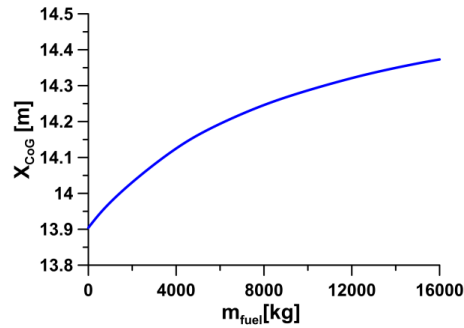


Figure 7.3: Vehicle CoG longitudinal position (from the nose apex) as the propellant is consumed

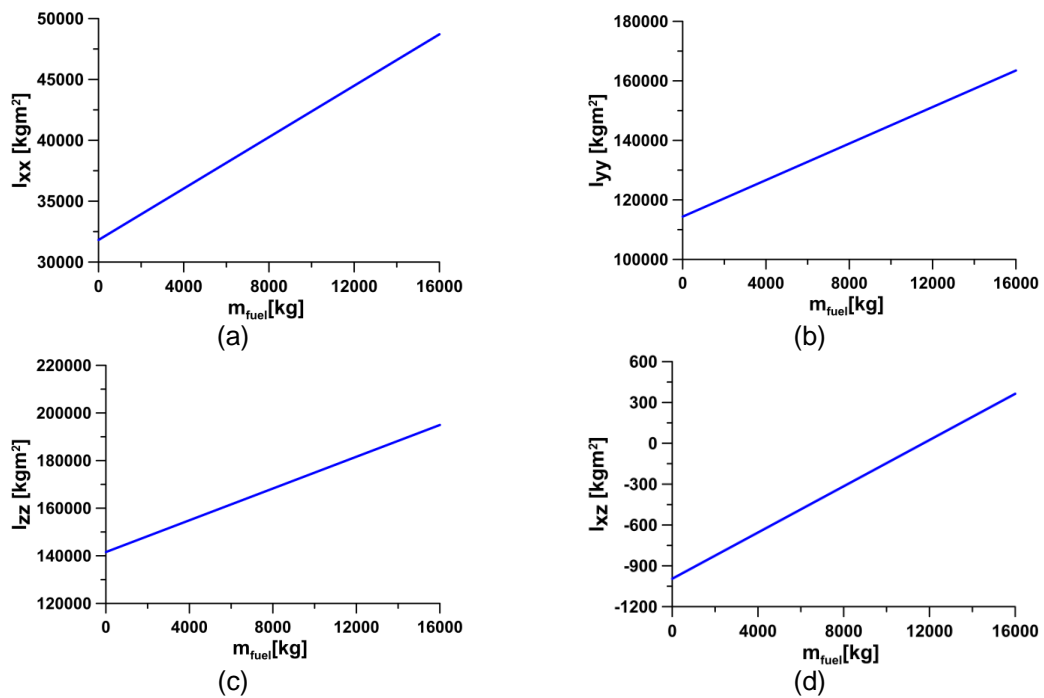


Figure 7.4: Vehicle inertia properties with respect to body axes centered in the CoG, as a function of fuel mass

7.2 Six-DoF nonlinear dynamic model

The six-dof nonlinear dynamic model of the vehicle, developed in MATLAB Simulink [2] environment, includes different blocks (Figure 7.5).

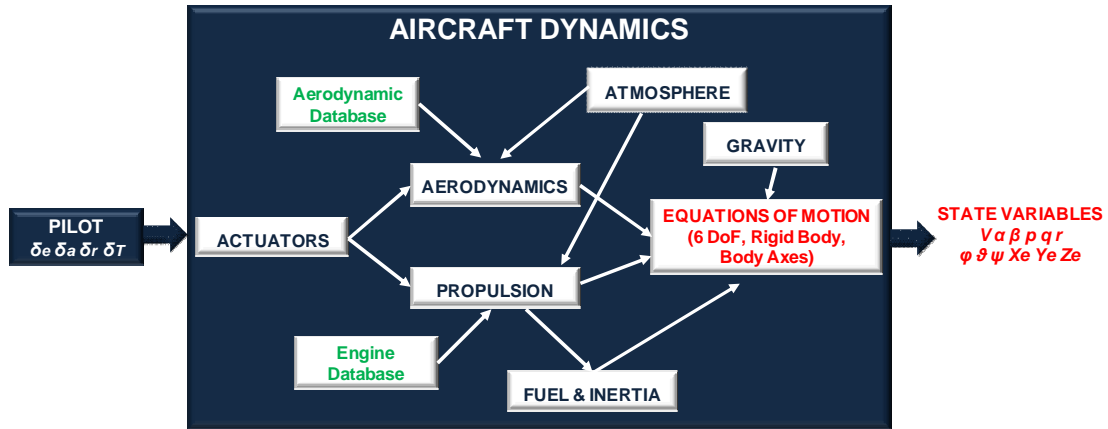


Figure 7.5: MASLab model block diagram

Pilot

The *Pilot* block provides the external command inputs including the deflections of control surfaces (δ_e , δ_a , δ_r) and the throttle δ_T . It can be linked to a joystick for manual control in real-time.

Actuators

The *Actuators* module calculates the effective deflections of control surfaces resulting from pilot inputs and takes into account the fact that surfaces must be moved by real devices which do not operate instantly. Actuators are modelled by means of first order transfer functions.

Equations of motion

The module *Equations of motion* includes the six-DoF equations which govern the motion of the aircraft (supposed to be a rigid body), the kinematic and the navigation equations. Gravitational, aerodynamic and propulsive forces and moments acting on the aircraft are expressed in body axes reference frame. Aircraft position and attitude are expressed in Earth reference frame.

These equations allow calculating the state variables:

- transitional velocities with respect to body reference frame: $u \ v \ w$
- angular velocity with respect to body reference frame: $p \ q \ r$
- Euler angles which express aircraft attitude: $\varphi \ \vartheta \ \psi$
- aircraft position with respect to Earth reference frame: $X_{EG} \ Y_{EG} \ Z_{EG}$

The six-DoF equations of motions are defined as:

$$\begin{pmatrix} \dot{u} \\ \dot{v} \\ \dot{w} \end{pmatrix} = \begin{bmatrix} 0 & -r & q \\ r & 0 & -p \\ -q & p & 0 \end{bmatrix} \begin{pmatrix} u \\ v \\ w \end{pmatrix} + m \begin{pmatrix} X_G + X_A + X_T \\ Y_G + Y_A + Y_T \\ Z_G + Z_A + Z_T \end{pmatrix}$$

$$\begin{pmatrix} \dot{p} \\ \dot{q} \\ \dot{r} \end{pmatrix} = [I]_B^{-1} \left(\begin{pmatrix} L_A + L_T \\ M_A + M_T \\ N_A + N_T \end{pmatrix} - \begin{bmatrix} 0 & -r & q \\ r & 0 & -p \\ -q & p & 0 \end{bmatrix} [I]_B \begin{pmatrix} p \\ q \\ r \end{pmatrix} \right)$$

where m is the vehicle mass and $[I]_B$ is the Inertia matrix:

$$[I]_B = \begin{bmatrix} I_{XX} & -I_{XY} & -I_{XZ} \\ -I_{XY} & I_{YY} & -I_{YZ} \\ -I_{XZ} & -I_{YX} & I_{ZZ} \end{bmatrix}$$

The kinetic and navigation equations are, respectively:

$$\begin{pmatrix} \dot{\varphi} \\ \dot{\vartheta} \\ \dot{\psi} \end{pmatrix} = \begin{bmatrix} 1 & \sin \varphi \tan \vartheta & \cos \varphi \tan \vartheta \\ 0 & \cos \varphi & -\sin \varphi \\ 0 & \frac{\sin \varphi}{\cos \vartheta} & \frac{\cos \varphi}{\cos \vartheta} \end{bmatrix} \begin{pmatrix} p \\ q \\ r \end{pmatrix}$$

$$\begin{pmatrix} \dot{X}_{EG} \\ \dot{Y}_{EG} \\ \dot{Z}_{EG} \end{pmatrix} = \begin{bmatrix} \cos \vartheta \cos \psi & \sin \varphi \sin \vartheta \cos \psi - \cos \varphi \sin \psi & \cos \varphi \sin \vartheta \cos \psi + \sin \varphi \sin \psi \\ \cos \vartheta \sin \psi & \sin \varphi \sin \vartheta \sin \psi + \cos \varphi \cos \psi & \cos \varphi \sin \vartheta \sin \psi - \sin \varphi \cos \psi \\ -\sin \vartheta & \sin \varphi \cos \vartheta & \cos \varphi \cos \vartheta \end{bmatrix} \begin{pmatrix} u \\ v \\ w \end{pmatrix}$$

The solution of these equations provides the value of the state vector derivative \dot{X} which is integrated to obtain the new value of $X = [u \ v \ w \ p \ q \ r \ \varphi \ \vartheta \ \psi \ X_{EG} Y_{EG} Z_{EG}]^T$ by means of a Discrete-Time Integrator block in which a sample time and a initial condition X_{zero} are defined.

The module also includes the conversion of translational velocities into the equivalent values of airspeed V , angle of attack α and sideslip angle β :

$$V = \sqrt{u^2 + v^2 + w^2} \quad \alpha = \tan^{-1} \frac{w}{u} \quad \beta = \sin^{-1} \frac{v}{V}$$

Atmosphere

The *Atmosphere* module provides the values of environmental variables, in particular the static temperature T_∞ and pressure p_∞ (using the classic 1976 COESA Atmosphere model) and the gravitational acceleration g , obtained directly from the altitude value $H = -Z_{EG}$. From these more variables are calculated: air density ρ_∞ and viscosity μ_∞ , Mach number M_∞ , dynamic pressure q_∞ and Reynolds number Re_∞ .

Gravity

The *Gravity* module calculates the values of gravitational forces acting on the aircraft using the equations below. Gravitational moments are identically zero, because evaluated with respect to body axes centered in the aircraft CoG.

$$\begin{Bmatrix} X_G \\ Y_G \\ Z_G \end{Bmatrix} = \begin{Bmatrix} -mg \sin \vartheta \\ mg \cos \vartheta \sin \psi \\ mg \cos \vartheta \cos \psi \end{Bmatrix}$$

Aerodynamics

The *Aerodynamics* module calculates the values of aerodynamic forces and moments acting on the aircraft, taking into account the aircraft altitude, Mach number and control surfaces deflections.

In particular the module operates in a sequence that involves:

1. The calculation of the aerodynamic coefficients and derivatives by using a set of 2D and 3D look-up-tables, that constitutes the vehicle *Aerodynamic Database* of the upgraded configuration.
2. The calculation of the aerodynamic force and moment coefficients using the equations:

$$\begin{aligned} c_L &= c_{L \text{ basic}} + \Delta c_{L \text{ elevons}} + \Delta c_{L \text{ ailerons}} + c_{L\dot{\alpha}} \frac{\dot{\alpha} \bar{c}}{2V} + c_{L\dot{q}} \frac{q \bar{c}}{2V} \\ c_D &= c_{D \text{ basic}} + \Delta c_{D \text{ elevons}} + \Delta c_{D \text{ ailerons}} + \Delta c_{D \text{ rudder}} + \Delta c_{D \text{ sideslip}} \\ c_M &= c_{M \text{ basic}} + \Delta c_{M \text{ elevons}} + \Delta c_{M \text{ ailerons}} + c_{M\dot{\alpha}} \frac{\dot{\alpha} \bar{c}}{2V} + c_{M\dot{q}} \frac{q \bar{c}}{2V} \\ c_Y &= c_{Y\beta} \beta + \Delta c_{Y \text{ rudder}} + c_{Y\hat{p}} \frac{pb}{2V} + c_{Y\hat{r}} \frac{rb}{2V} \\ c_L &= c_{L\beta} \beta + \Delta c_{L \text{ ailerons}} + \Delta c_{L \text{ rudder}} + c_{L\hat{p}} \frac{pb}{2V} + c_{L\hat{r}} \frac{rb}{2V} \\ c_N &= c_{N\beta} \beta + \Delta c_{N \text{ ailerons}} + \Delta c_{N \text{ rudder}} + c_{N\hat{p}} \frac{pb}{2V} + c_{N\hat{r}} \frac{rb}{2V} \end{aligned}$$

Force coefficients expressed in wind axes (c_L and c_D) are transformed to obtain their body-axes equivalents (c_X and c_Z) using the equations:

$$\begin{Bmatrix} c_X \\ c_Z \end{Bmatrix} = \begin{bmatrix} \sin \alpha & -\cos \alpha \cos \beta \\ -\cos \alpha & -\sin \alpha \cos \beta \end{bmatrix} \begin{Bmatrix} c_L \\ c_D \end{Bmatrix}$$

3. The calculation of the aerodynamic forces and moments using the equations:

$$\begin{Bmatrix} X_A \\ Y_A \\ Z_A \end{Bmatrix} = q_\infty S \begin{Bmatrix} c_X \\ c_Y \\ c_Z \end{Bmatrix} \qquad \begin{Bmatrix} L_A \\ M_A \\ N_A \end{Bmatrix} = q_\infty S \begin{Bmatrix} c_L \bar{b} \\ c_M \bar{c} \\ c_N \bar{b} \end{Bmatrix}$$

Propulsion

The *Propulsion* module calculates the values of propulsive forces and moments acting on the aircraft.

In particular the value of maximum available thrust T_{max} provided by each engine is calculated taking into account the aircraft altitude and Mach number (Figure 2.6a), using a 2D look-up table that constitutes the *Engine Database*. This value is multiplied by the throttle δ_T (that assumes values from 0 to 1) to achieve the effective thrust.

Supposing that the thrust vectors provided by the two engines are applied in their center of gravity and parallel to longitudinal body axis, the propulsive forces and moments are:

$$\begin{Bmatrix} X_T \\ Y_T \\ Z_T \end{Bmatrix} = \begin{Bmatrix} 2 \delta_T T_{max} \\ 0 \\ 0 \end{Bmatrix} \qquad \begin{Bmatrix} L_T \\ M_T \\ N_T \end{Bmatrix} = \begin{Bmatrix} 0 \\ X_T Z_{arm} \\ 0 \end{Bmatrix}$$

where Z_{arm} is the vertical distance between the vehicle and the engines center of gravity.

Fuel & Inertia

The *Fuel & Inertia* module calculates the current fuel consumption \dot{m}_p using the equation:

$$\dot{m}_p = - \frac{T}{I_{sp} \cdot g_{SL}}$$

where the value of the TBCC engine specific impulse I_{sp} is calculated taking into account the aircraft altitude and Mach number (Figure 2.6b), using a look-up table and g_{SL} is the gravitational acceleration at sea level.

The value of the current mass of the aircraft is obtained by subtracting the amount of fuel used from available onboard fuel and adding it to the aircraft empty weight. A set of 1D look-up tables is used to calculate aircraft center of gravity position and the inertia tensor for the current aircraft mass.

7.3 Trim algorithm

Trimmed flight conditions are a prerequisite for linearizing the nonlinear model as well as for initializing the model for dynamic simulations.

The aircraft nonlinear dynamic model can be synthetically expressed as:

$$f(\dot{X}, X, U) = 0 \quad , \quad \text{with}$$

$$X = [V \ \alpha \ \beta \ p \ q \ r \ \vartheta \ \psi \ X_{EG} \ Y_{EG} \ Z_{EG}]^T \quad \text{and} \quad U = [\delta_e \ \delta_a \ \delta_r \ \delta_T]^T$$

The trimmed condition is defined as a condition $X = X_{trim}$ which satisfies:

$$\dot{X} = 0, \quad U = const$$

According to the latest equations the trimmed flight condition is achieved when the sums of all forces and moments acting on the aircraft are equal zero. That means that the transitional and rotational accelerations $\dot{V}, \dot{\alpha}, \dot{\beta}, \dot{p}, \dot{q}, \dot{r}$ are identically zero.

Steady-state wings-level flight conditions have been analyzed, with the following additional constraints:

$$\varphi \ \dot{\varphi} \ \dot{\vartheta} \ \psi \ \dot{\psi} \equiv 0 \quad p \ q \ r \equiv 0$$

The calculation of the trimmed flight conditions can't be done analytically, because of the complex functional dependence of the aerodynamic data. A convenient way to find trimmed flight condition is by using a numerical algorithm suggested in [3] and presented in Figure 7.6. The algorithm is based on multivariable optimization method SIMPLEX [4], which minimizes a scalar cost function J built from the sum of the squares of the derivatives above mentioned:

$$J = \dot{u}^2 + \dot{v}^2 + \dot{w}^2 + 10(\dot{p}^2 + \dot{q}^2 + \dot{r}^2) + 100(\dot{\phi}^2 + \dot{\vartheta}^2 + \dot{\psi}^2)$$

The user specifies flight conditions, in particular altitude H , airspeed V and climb angle γ , as well as the aircraft mass m . The trim algorithm iteratively adjusts the control variables - $\delta_e, \delta_a, \delta_r, \delta_T$ - and appropriate state variables - α, β - in order to minimize the scalar cost function J .

In the minimization procedure the remaining variable ϑ is determined from the constraint equation:

$$\tan \vartheta = \frac{ab + \sin \gamma \sqrt{a^2 - \sin^2 \gamma + b^2}}{a^2 - \sin^2 \gamma}, \quad \vartheta \neq \pm \frac{\pi}{2}$$

$$a = \cos \alpha \cdot \cos \beta \quad b = \sin \phi \cdot \sin \beta + \cos \phi \cdot \sin \alpha \cdot \cos \beta$$

The numerical trim procedure is repeated iteratively until J is minimized. The last adjusted state and control variables represent the desired trimmed flight conditions.

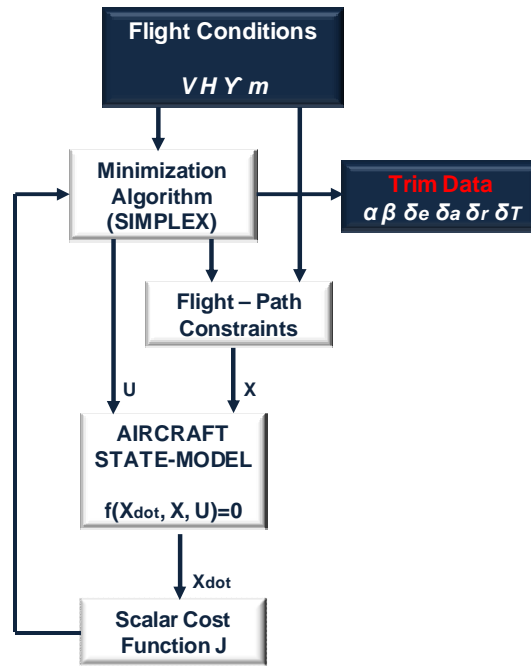


Figure 7.6: Trim algorithm

7.4 Trim performances

Figure 7.7a shows the two regions enclosing Mach number and altitude conditions, for which the vehicle is able to perform steady-state wings-level flight, at maximum takeoff weight and empty weight.

The two regions exhibit the same lower boundary and different upper boundaries. Lower boundary curve discontinuities are due to limitation for maximum available thrust. In transonic regime the upper boundary curves decrease because the available thrust is not able to balance drag force, due to the drag divergence effect around $M_\infty = 1$ combined with the decrease of the available thrust with altitude.

In the other graphs of Figure 7.7 corresponding ranges of angle of attack, elevons deflection angle and turboramjet throttle, as a function of Mach number, are presented. In subsonic regime, as Mach number increases lift coefficient increases and the angle of attack necessary to balance vehicle weight decreases, reaching minimum around $M_\infty = 1$. Obviously a lower angle of attack leads to a lower elevons upward deflection angle necessary to balance the nose down pitching moments produced by wings and turboramjet thrust.

The behaviour is opposite in supersonic regime: the reduction of c_L , as the Mach number increases, involves higher values for α and then higher values for δ_e to satisfy vertical forces and pitching moment equilibrium, respectively.

In the transition from subsonic to supersonic regime the backward translation of the vehicle center of pressure leads to a further increase of δ_e values required to trim the aircraft. This justifies the jump presented around $M_\infty = 1$.

The high negative values of δ_e in supersonic regime are also due to the need to equilibrate the pitching moment produced by the high turboramjet thrust necessary to equilibrate the high pressure drag developed in supersonic flow.

As the altitude increases, the reduction of air density leads to an increase of lift coefficient and consequently of angle of attack, necessary to guarantee vertical force equilibrium. Subsequently a higher elevons deflection angle is necessary for pitching moment balance.

As the weight decreases, a lower c_L and then a lower α is necessary for vertical force equilibrium. Subsequently a lower δ_e is required to trim the aircraft.

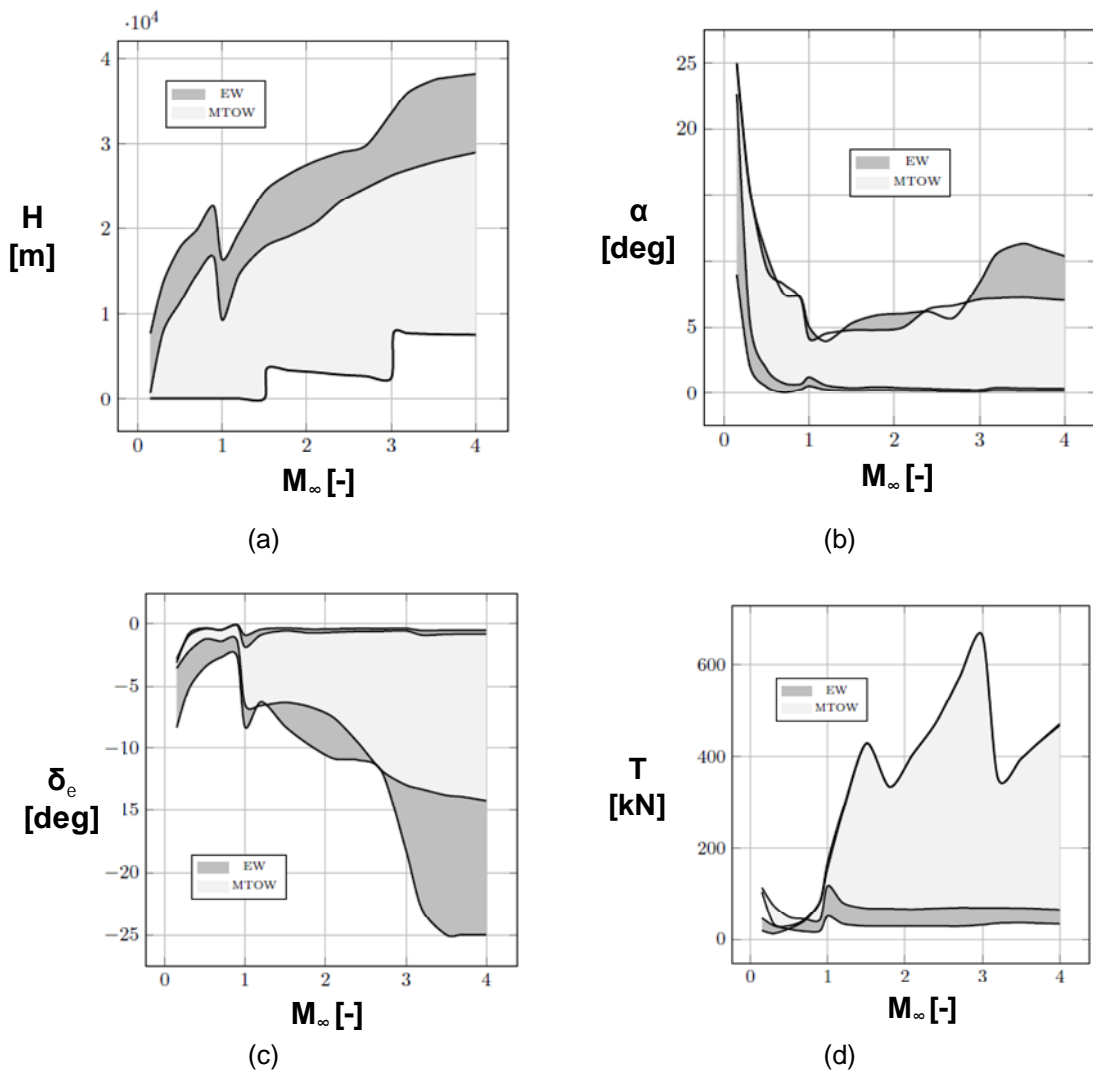


Figure 7.7: HyPlane trim envelop at MTOW and EW (a). Angle of attack (b), elevons deflection angle (c) and turboramjet throttle (c) in trimmed conditions

The effect of climb angle is visible in Figure 7.8. As γ increases, the maximum altitude decreases, due to the longitudinal component of the weight force added to the drag force to be equilibrated by the engines thrust.

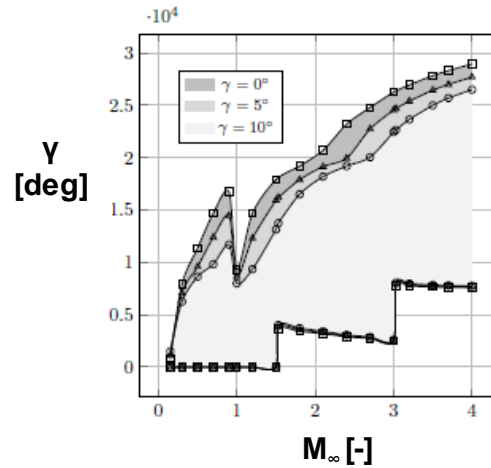


Figure 7.8: HyPlane trim envelope at MTOW varying the climb angle

In Figure 7.9 2D maps of aerodynamic efficiency corresponding to trimmed flight conditions for the vehicle, at maximum takeoff weight and empty weight, are presented. It is possible to observe that the vehicle is able to perform a cruise at Mach number of 4 and an altitude of 30 km, with a trimmed lift-to-drag ratio of about 4.

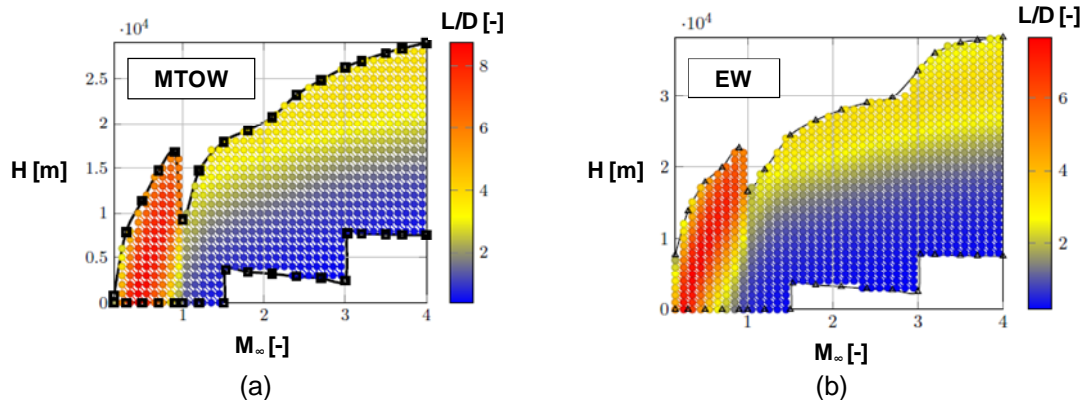


Figure 7.9: HyPlane aerodynamic efficiency in trimmed conditions at maximum takeoff weight (a) and at empty weight (b)

These results can be helpful to identify trajectories which minimize fuel consumption and maximize downrange.

References

- [1] P. Gunetti, M. Cassaro, M. Battipede, MASLab (Multipurpose Aircraft Simulation Laboratory) D3.2 User Manual: Aircraft Model Description Version 3 (2012)
- [2] MATLAB Simulink R2013a User's guide
- [3] B. L. Stevens, F. L. Lewis, Aircraft Control and Simulation, John Wiley & Sons (1992)
- [4] J. A. Nelder, R. Mead, Simplex method for function minimization, Computer Journal (1965)

8 Conclusions

In this work some contributions to the studies for a new concept for a small hypersonic airplane of six seats for Space tourism and point-to-point hypersonic transportation purposes, have been provided, through a synergistic integration between disciplines such as aerothermodynamics, propulsion and flight mechanics.

Research has been focused on aerodynamic analysis, which is essential for the evaluation of the effects of the aerodynamic heating in the hypersonic phase and for flight mechanics studies. In particular a validation methodology of an engineering tool has been carried out, aimed at the building of a comprehensive aerodynamic database and at the prevision of the effects of the aerodynamic heating in hypersonic regime.

On the basis of the predicted surface thermal loads occurring in the hypersonic cruise, proper materials able to sustain the most severe hypersonic conditions have been preliminarily identified.

Preliminary mission analysis carried out considering a three degree of freedom model have shown that vehicle is able to perform a medium range hypersonic cruise or a long-duration Space tourism mission (characterized by a sequence of sub-orbital parabolas offering short and repeated periods of low gravity in the high stratosphere), by optimizing the propulsion performances of two Turbine Cased Combined Cycle engines and a rocket engine in the different flight phases.

Finally longitudinal trim performances have been evaluated, taking advantage of a six degree of freedom model encompassing the vehicle aerodynamic, propulsive and inertia data. This analysis refers to an upgraded configuration of the vehicle, refined to meet visibility and stability requirements.

All presented methodologies and results can be considered a starting point for studies on more complex systems, based on the proposed concept of integrating aeronautical and Space technologies.

An appropriate Automatic Flight Control System for the vehicle could be studied in future works.